UR-1233
ER-13065-685

184 — UR-1233

Fermilab Library
0 1160 0006909 0

SEARCH FOR NEUTRAL HEAVY LEPTONS IN NEUTRINO-NUCLEON INTERACTIONS AT THE FNAL TEVATRON

Pawel de Barbaro
University of Rochester, Rochester, NY

RETURN TO FERMI LIBRARY
ROUTE TO
NAME
LOCATION

THE UNIVERSITY OF ROCHESTER

DEPARTMENT OF PHYSICS AND ASTRONOMY

ROCHESTER , NEW YORK

E744
E770

UR-1233
ER-13065-685

SEARCH FOR NEUTRAL HEAVY LEPTONS IN NEUTRINO-NUCLEON INTERACTIONS AT THE FNAL TEVATRON

Pawel de Barbaro
University of Rochester, Rochester, NY

Submitted in partial fulfillment of the requirement for the degree of Doctor of Philosophy in the Graduate School of Arts and Sciences, University of Rochester

Supervised by Arie Bodek
Department of Physics and Astronomy
College of Arts and Sciences

University of Rochester
Rochester, New York
1990

Curriculum Vitae

Pawel de Barbaro, born on December 17, 1959 in Krakow, Poland, graduated from the Nowodworski High School in 1979. He attended the Department of Physics and Mathematics at the Jagellonian University in Krakow, Poland and graduated in 1984 with the degree Master of Science. Since 1985, he has been a graduate student at the University of Rochester in Rochester, New York, where he has done research in High Energy Particle Physics towards the degree of Doctor of Philosophy.

Acknowledgements

I would like to express my thanks to all the members of the CCFR Collaboration for contributions to the experiment described in this thesis: Arie Bodek, Howard Budd and Willis Sakumoto from University of Rochester, Kurt Bachmann, Robert Blair, Costas Foudas, Bruce King, Walter Lefmann, Wing Leung, Sanjib Mishra, Paul Quintas, Steve Rabinowitz, Frank Sciulli, Bill Seligman and Mike Shaevitz from Columbia University, Frank Merritt, Mark Oreglia, Heidi Schellman, and Bruce Schumm from University of Chicago, Robert Bernstein, Fred Borcherding, Mike Lamm, Bill Marsh, and Drasko Yovanovitch from Fermilab, and Pam Sandler and Wesley Smith from University of Wisconsin.

Special thanks go to my advisor, Arie Bodek, who provided me with continous assistance and encouragement in every step of my work. I consider myself very fortunate to be one of Arie's graduate students.

I am grateful to my friend Howard Budd who has taught me many skills of experimental physics and has been always ready to discuss the problems of the Double Vertex analysis and to suggest possible solutions .

I would also like to thank Sanjib Mishra, for introducing me to the subject of the search for Neutral Heavy Leptons in ν-N interactions, and for many long and fruitfull discussions we have held over last two years.

Finally I want to thank my wife, Lucyna, my two daughters, Kaya and Izabella, and my entire family for their love and support during my graduate years.

SEARCH FOR NEUTRAL HEAVY LEPTONS IN NEUTRINO-NUCLEON INTERACTIONS AT THE FNAL TEVATRON*†

Pawel de Barbaro
University of Rochester, Rochester, NY

*Research supported by the U.S. Department of Energy.
†Submitted in partial fulfillment of the requirement for the degree of Doctor of Philosophy in the Graduate School of Arts and Sciences, University of Rochester.

Abstract

The search for Neutral Heavy Leptons (NHL) in the Neutrino-Nucleon (ν-N) interactions has been conducted using the CCFR Detector and the Fermilab Quad Triplet Beam (FNAL-E744 and FNAL-E770). No evidence for NHL was found in the charged current decay channel, NHL$\rightarrow \mu^- + X$. NHL with masses between 0.5 and 3.0 GeV/c^2 were excluded for coupling to muons below 1 to 10^{-4} of Fermi strength, depending on the NHL mass. An excess of 5.2 +/- 2.3 NHL candidates, in the neutral current decay channel, $NHL \rightarrow \nu + X$, was found for events with the separation between the production vertex and the decay vertex greater than 2.3 meters. No evidence for NHL was found in the neutral current decay channel, NHL$\rightarrow \nu + X$ for events with the separation between the production vertex and the decay vertex between 0.6 meters and 2.3 meters. NHL with masses between 0.5 and 2.0 GeV/c^2 were excluded for coupling to muon neutrinos below 1 to 5×10^{-4} of Fermi strength, depending on the NHL mass.

Contents

Curriculum Vitae ii

Acknowledgements iii

Abstract iv

Contents v

List of Tables x

List of Figures xi

1 Introduction 1

1.1 Overview 1

1.2 Neutrino Mass 2

1.2.1 Dirac and Majorana Mass Terms 3

1.3 Theoretical Motivations for Neutral Heavy Leptons 4

1.3.1 Fourth Generation Neutrinos 5

1.3.2 Left-Right Symmetric Models (LRSMs) 5

1.3.3 Fermion masses in Left-Right Symmetric Models 7

1.3.4 Neutral Heavy Leptons in Grand Unified Theories 11

1.4 NHL signatures 12

1.4.1 NHL signatures in ν_μ-N scattering experiments 16

1.5 Overview of the Thesis 18

2 The Experimental Setup 19

2.1 The Beam Line 19

2.1.1 Time Structure of the Beam 19

2.1.2 Neutrino Beam Extraction 20

2.2 The Detector 21

2.3 The Target Calorimeter 22

2.3.1 Scintillation counters 22

2.3.2 Drift Chambers 23

2.4 The Muon Spectrometer 24

2.4.1 Toroid Scintillation Counters 25

2.4.2 Trigger counters 25

2.4.3 Scintillation Counter Numbering 25

2.5 Detector Triggering 26

2.5.1 Neutral Current Trigger Efficiency 27

2.6 Comparison of the Target and Toroid Instrumentation 29

3 The Event Reconstruction 31

3.1 Vertex Position Measurement 32

3.2 Measurement of Shower Energy 33

3.2.1 Energy Calibration of the Toroid Counters 35

3.3 Energy Determination 35

3.4 Delay Correction in the Energy Calculation 37

3.5 Efficiency of finding showers 38

3.6 Timing Determination 41

3.7 Shower Length Determination 44

3.8 Distinction between NC and CC showers 45

3.8.1 Contaminations of NC and CC classes 46

4 The Event Analysis **49**

4.1 Overview 49

4.2 The Event Selection 50

4.2.1 First pass cuts 51

4.2.2 Second pass cuts 53

4.2.3 Angle between the upstream and the downstream showers . . 58

4.2.4 Selection of In-Time Events 58

4.3 Classification of In-Time Events 60

4.3.1 Event Scanning 60

4.3.2 Material separation between the upstream and downstream showers 62

4.3.3 Shower type of secondary vertex 64

5 The Background Estimation **67**

5.1 Overview 67

5.2 The Random Overlay Background 67

5.2.1 Selection of Out-of-Time Events 68

5.2.2 Timing range of Out-of-Time events 70

5.2.3 VETO Rejection of Out-of-Time events 71

5.2.4 Visual Scanning and Classification of Out-of-Time Events . . . 73

5.2.5 The Ratio $R_{NC/CC}$ for the Out-of-Time sample 77

5.2.6 The Superbucket Correction 79

5.2.7 Efficiency of Shower-finding algorithm for Out-of-Time events 81

5.2.8 Summary of the Overlay Background Calculations 82

5.3 The Neutral Hadron Punch-Through Background 83

5.3.1 Test-Beam Experimental Setup 83

5.3.2 Test-Beam Double Vertex Selection 85

5.3.3 Test-Beam Double Vertex Analysis 86

5.3.4 The Normalization of the Test-Beam and the neutrino-induced Double Vertex Samples 88

5.3.5 Systematic uncertainties in the estimation of the neutral hadron punch-through background in ν-N interactions 97

5.4 The Total Background Estimation 99

6 Results and Comparisons with Theoretical Predictions **100**

6.1 Overview 100

6.2 Calculation of the statistical significance of the limit 100

6.3 Limits on observed number of NHL events 103

6.4 Comparisons with Theoretical Predictions 107

6.5 Conclusions 108

A The CCFR Collaboration 110

B Parametrization of the hadronic shower length 111

C Calculation of the superbucket correction 114

D NHL Monte Carlo generation procedure 118

References 122

Tables 125

Figures 133

List of Tables

4.1 Summary of the visual scanning of the In-Time Double Vertex Events. 125

4.2 Number of In-Time Target Double Vertex Events 125

4.3 Number of In-Time Toroid Double Vertex Events 126

5.1 Summary of the visual scanning of the Out-of-Time Double Vertex Events. 127

5.2 Number of Out-of-Time Target Double Vertex Events 127

5.3 Number of Out-of-Time Toroid Double Vertex Events 128

5.4 Summary of Random Overlay Background for Target Double Vertex Events. 129

5.5 Summary of Random Overlay Background for Toroid Double Vertex Events. 129

5.6 Summary of Neutral Hadron Punch-through Background for Target Double Vertex Events in $NC \rightarrow CC$ channel. 130

5.7 Summary of Signal and Background events in Double Vertex search. . 131

C.1 Summary of the number of In-Time $CC \rightarrow CC$ random overlay events. 132

C.2 Summary of the number of Out-of-Time $CC \rightarrow CC$ random overlay events normalized to 1 RF bucket. 132

List of Figures

1.1 The Feynman diagram for the production of isosinglet Neutral Heavy Lepton in $\nu - N$ interactions. 133

1.2 The Feynman diagram for the decay of NHL via the coupling to Z^0 or to $W^{\pm}$. 134

1.3 The Feynman diagrams for the production of Neutral Heavy Leptons. 135

1.4 Existing limits on masses and coupling suppression factors of isosinglet NHL. 136

2.1 The FNAL Tevatron accelerator and the neutrino beam line. 137

2.2 The Quadrupole Triplet Neutrino Beam line. 138

2.3 The CCFR neutrino detector. 139

2.4 Structure of a typical calorimeter cart. 140

2.5 The Muon Spectrometer. 141

2.6 The diagram of a toroid cart. 142

2.7 The diagram of Trigger 1 logic. 143

2.8 The diagram of Trigger 2 logic. 144

2.9 The diagram of Trigger 6 logic. 145

2.10 The diagram of *PTOR* logic. 146

2.11 The distribution of the longitudinal position of the interactions recorded with Trigger 2. 147

2.12 Efficiency of Trigger 2 as a function of the hadronic energy of neutrino-induced interaction. 148

3.1 The diagram of the relative timing between the ADC gate and the phototube pulses. 149

3.2 The delay correction in the energy calculation R_{delay}, as a function of the difference between the shower timing and the ADC gate. 150

3.3 The efficiency of shower finding algorithm as as function of shower energy for shower occurring inside the fiducial volume of the Target. . 151

3.4 The efficiency of shower finding algorithm as as function of shower energy for shower occurring inside the fiducial volume of the Toroid. . 152

3.5 The pulse height dependent timing correction as a function of energy deposited in individual counter. 153

3.6 The resolution of individual counter timing as a function of energy deposited in the counter. 154

3.7 Timing resolution of showers occurring inside the fiducial volume of the Target. 155

3.8 Timing resolution of showers occurring inside the fiducial volume of the Toroid. 156

3.9 The ratio of the NC-type to the CC-type interactions for events occurring in the Target, as a function of the radial position of interaction. . 157

3.10 The ratio of the NC-type to the CC-type interactions for events occurring in the Toroid, as a function of the radial position of interaction. . 158

4.1 Double Vertex signature of Neutral Heavy Lepton production in ν-N interaction. 159

4.2 Neutral hadron punch-through background of the Double Vertex signature of NHL decaying to muonless channel $NHL \rightarrow \nu + X$. 160

4.3 Random overlay background of the Double Vertex signature of NHL production. 161

4.4 Distribution of the timing difference between the upstream and the downstream showers in the sample of neutrino-induced Double Vertex events. The downstream shower occurred inside the fiducial volume of the Target. 162

4.5 Distribution of the timing difference between the upstream and the downstream showers in the sample of neutrino-induced Double Vertex events. The downstream shower occurred inside the fiducial volume of the Toroid 163

5.1 Distribution of the difference between interaction time and timing of random VETO hits for sample of Trigger 2 events. 164

5.2 Out-of-Time Double Vertex Events with upstream interaction occurring at the edge of fiducial volume of the Target (with $PLACE_1$ =81 or 82): Distribution of the relative timing between upstream shower and the VETO hit 165

5.3 Test-Beam punchthrough events: Distribution of the relative timing between the primary and secondary shower. 166

5.4 Test-Beam punchthrough events: Distribution of the angle between the hadron beam direction and the direction of the neutral hadron punchthrough. 167

5.5 Test-Beam punchthrough events: Distribution of the energy of secondary shower. 168

5.6 Test-Beam punchthrough events: Distribution of the separation between the end of primary shower and the beginning of the punchthrough shower. 169

5.7 Longitudinal acceptance of the CCFR detector for Double Vertex events as a function of the separation between the end of upstream shower and the beginning of the downstream shower. 170

5.8 Longitudinal acceptance of the Test-Beam detector configuration relative to the acceptance of the neutrino induced Double Vertex events. 171

5.9a Energy spectrum of single vertex neutrino induced interactions. . . . 172

5.9b Energy spectrum of single vertex Test-Beam data. 173

5.10 Comparison of pion induced and neutrino induced fragmentation functions of K^0 production. 174

6.1 $NHL \rightarrow \nu + X$, Small Separation region: Monte Carlo generated number of NHL as a function of coupling suppression factor U^2, relative to the Fermi coupling G_F for different values of mass of NHL 175

6.2 $NHL \rightarrow \nu + X$, Intermediate Separation region: Monte Carlo generated number of NHL as a function of coupling suppression factor U^2, relative to the Fermi coupling G_F for different values of mass of NHL 176

6.3 $NHL \rightarrow \nu + X$, Large Separation region: Monte Carlo generated number of NHL as a function of coupling suppression factor U^2, relative to the Fermi coupling G_F for different values of mass of NHL 177

6.4 $NHL \rightarrow \mu + X$, Small, Intermediate and Large Separation regions combined: Monte Carlo generated number of NHL as a function of coupling suppression factor U^2, relative to the Fermi coupling G_F for different values of NHL mass 178

6.5 NHL limits for charged current and neutral current decay channels and different regions of the separation between the end of the upstream and the beginning of the downstream showers. 179

6.6 Comparison of results for NHL limits for charged current and neutral current decay channels from this thesis with NHL limits from other experiments. 180

B.1 Distributions of a length of hadronic showers for different settings of hadron energy beam. 181

B.2 Parametrization of the length of hadronic showers as a function of hadronic energy E_{had}. 182

C.1 Distribution of the relative timing between random overlays of two uncorrelated charged current interactions. 183

8.2 Number of random $CC \rightarrow CC$ overlays as a function of the timing difference between the two muons. The dashed line corresponds to the average of random Out-of-Time overlays per 1 RF bucket. 184

Chapter 1

Introduction

1.1 Overview

This thesis reports on a search for Neutral Heavy Leptons (NHL) conducted by the Chicago-Columbia-Fermilab-Rochester (CCFR) Collaboration. The experiment was performed at Fermilab for the purpose of studying the interactions of neutrinos from the Tevatron Quadrupole Triplet Beam (QTB) with an iron target. The data used in this analysis was recorded during two Tevatron fixed target running periods in 1985 (Fermilab Experiment E744) and in 1987 (Fermilab Experiment E770).

The possibility of neutral current couplings between ν_μ and NHL could give rise to secondary vertices associated with NHL production and its subsequent decay in ν_μ-N interactions. The production of NHL would proceed via the exchange of neutral gauge bosons (Figure 1.1):

$$\nu_\mu + N \longrightarrow NHL_\mu + X \tag{1.1}$$

The decay of the NHL would proceed through the coupling of the NHL to the neutral current Z^0 (Figure 1.2a):

$$NHL_\mu \longrightarrow \nu_\mu + X \tag{1.2}$$

or the coupling to the charged currents W^+ (W^-) (Figure 1.2b):

$$NHL_\mu \longrightarrow \mu^-(\mu^+) + X \tag{1.3}$$

1.2 Neutrino Mass

The existence of a neutral, light, spin 1/2 particle (with mass of the order of magnitude of the electron) was first suggested by Wolfgang Pauli in 1930 [1], in order to explain the continous energy spectrum of electrons from nuclear β decay. Since then the question of the possibility of a non-zero neutrino mass has been intriguing theorists and experimental physicists. Enrico Fermi in his theory of β decay published in 1934 [2] recognized that the mass of a neutrino could be deduced from the shape of the β spectrum and concluded that it was much smaller than the electron mass.

The ordinary Dirac fermion is described with a four-component state function, with two states of helicity for particles and two states of helicity for antiparticles. If a the neutrino has a finite mass it must occur in both helicities, since a positive helicity state can be transformed into a negative one by Lorentz transformation. However, if the neutrino is exactly massless, negative or positive helicity states are independent solutions to the Dirac equation. Thus only parity conservation would require both of the helicity states to occur. The discovery of the parity violation in weak interactions [3] led to the 'two-component neutrino' theory [4]. According to this theory right-handed neutrinos and left-handed antineutrinos are absent from all weak interactions

and therefore it is possible to reduce two degrees of freedom in the Dirac equation.

About 10 years ago, a polarized electron-deuteron scattering experiment at SLAC [5] demonstrated that parity violation was a characteristic of the weak interactions, and not exclusively the feature of the neutrino particles. Thus, the question of neutrino mass has become interesting again.

Today, the experimental data on the mass of neutrinos of the three known lepton families is consistent with zero:

- the limit of $m(\nu_e) < 18$ eV at 90% confidence level (90%CL) comes from the analysis of the energy spectrum from the tritium β decay [6];
- the limit of $m(\nu_\mu) < 250$ keV (90%CL) was obtained by measuring the energy spectrum of the muons emitted in π^+ decay at rest [7];
- the limit of $m(\nu_\tau) < 35$ MeV (95%CL) comes from the study of the τ decay to 5 pions and ν_τ [8].

1.2.1 Dirac and Majorana Mass Terms

There are two types of the Lorentz invariant mass terms that can be formed from fermion fields: a Dirac mass term:

$$-\mathcal{L}_D = \frac{1}{2} m_D \bar{\nu}_L \nu_R + h.c. \tag{1.4}$$

or a Majorana mass term:

$$-\mathcal{L}_M = \frac{1}{2}(m_L \bar{\nu}_L^c \nu_L + m_R \bar{\nu}_R^c \nu_R) + h.c., \tag{1.5}$$

where we have used the following convention for chirality-projection and charge conjunction (antiparticle) operators:

$$\begin{aligned}
\nu^c &= C\gamma^0 \nu^* = i\gamma^2 \nu^* \\
\overline{(\nu^c)} &= \nu^T C \\
\nu_L &= \tfrac{1}{2}(1-\gamma_5)\nu \\
\nu_R &= \tfrac{1}{2}(1+\gamma_5)\nu \\
\nu_L^c &= (\nu_L)^c = \tfrac{1}{2}(1-\gamma_5)\nu^c = (\nu^c)_R \\
\nu_R^c &= (\nu_R)^c = \tfrac{1}{2}(1-\gamma_5)\nu^c = (\nu^c)_L
\end{aligned} \tag{1.6}$$

A Dirac mass term, which couples left-handed field ν_L with right-handed field ν_R, is invariant under the global phase (θ) transformation:

$$\nu \longrightarrow \nu' = e^{i\theta}\nu \tag{1.7}$$

and therefore conserves the total lepton number. In contrast, Majorana mass terms connect states of the same chirality, which makes the Lagrangian no longer invariant under global transformations and leads to the violation of fermion number. Thus Majorana neutrino masses would lead for instance to neutrino-less double β decay:

$$(Z-1) \longrightarrow (Z+1) + 2e^-. \tag{1.8}$$

1.3 Theoretical Motivations for Neutral Heavy Leptons

The Standard Model[9] of electroweak interactions has only massless neutrinos. The simple Higgs structure (one set of Higgs doublets) leads to global symmetries corresponding to the separate conservation of e-, μ-, τ-lepton numbers, which forbids

the Majorana mass term $\bar{\nu}_L^c$. On other hand, there are no ν_R that could combine with ν_L to form a Dirac mass term. In other words, the masslessness of the neutrinos is related to the restricted particle content being considered in the Standard Model. However, there are several possible extensions of the Standard Model in which m_ν is nonzero. The introduction of a right-handed neutrino allows a Dirac mass terms. In addition, the introduction of more complex Higgs fields, leads to the breaking of global symmetry and allows Majorana mass terms.

1.3.1 Fourth Generation Neutrinos

Since the number of lepton generations is not predicted by the Standard Model, there is the possibility of a fourth, yet unknown, family of leptons. Thus, in general, one may expect that the lightest member of the fourth generation of leptons is a neutrino. Such a neutrino, often called a sequential Neutral Heavy Lepton, would be a member of the $SU(2)_L$ doublet, and could acquire its mass through the mixing with its right-handed partner.

1.3.2 Left-Right Symmetric Models (LRSMs)

The Standard Model of electro-weak interactions based on $SU(2)_L \times U(1)_Y$ gauge groups has been an unquestionable success. It predicted the existence of neutral current interactions, and the relationship between the masses of gauge bosons $W^\pm$ and Z^0 and the Weinberg angle θ_W. Nevertheless it does not answer all the questions regarding electro-weak interactions. It does not explain fermion masses; it does not

explain of the symmetry and symmetry breaking of weak interactions, and it does not explain the origin of parity violation. There exists a class of models that attempt to address these issues. One class are Left-Right Symmetric Models (LRSMs)[10]. The main feature of Left Right Symmetric Models involves the restoration of parity in the weak interactions to the level of a conserved quantum number. At low energies, LRSMs are consistent with predictions of the Standard Model, but at high energies they introduce new features. We now discuss LRSMs in analogy to the Standard Model.

The LRSM theories are based on the gauge group $SU(2)_L \times SU(2)_R \times U(1)_{B-L}$, where $SU(2)_L$ is the symmetry of left weak isospin, $SU(2)_R$ is the symmetry of the right isospin and $U(1)_{B-L}$ is generator corresponding to the $B-L$ quantum numbers. The particles are characterized by 3 quantum numbers: I_{3L}, I_{3R}, and $Y = (B-L)$. The electric formula :

$$Q = I_{3L} - I_{3R} - \frac{1}{2}(B-L) \tag{1.9}$$

is an analog of the Standard Model's $Q = I_3 + \frac{1}{2}Y$. We have the following doublets:

$$\Psi_L = \begin{pmatrix} \nu \\ e \end{pmatrix}_L \quad \Psi_R = \begin{pmatrix} \nu \\ e \end{pmatrix}_R$$
$$Q_L = \begin{pmatrix} u \\ d \end{pmatrix}_L \quad Q_R = \begin{pmatrix} u \\ d \end{pmatrix}_R \tag{1.10}$$

and they are characterized by the following quantum numbers:

$$\begin{aligned} \Psi_L &: (\tfrac{1}{2}, 0, -1) \\ \Psi_R &: (0, \tfrac{1}{2}, -1) \\ Q_L &: (\tfrac{1}{2}, 0, \tfrac{1}{3}) \\ Q_R &: (0, \tfrac{1}{2}, \tfrac{1}{3}), \end{aligned} \tag{1.11}$$

where the numbers in brackets correspond to I_{3L}, I_{3R}, and $Y = (B - L)$, respectively.

In this model, the following Higgs particles are introduced:

$$\begin{aligned} \Delta_L &: (1, 0, +2) \\ \Delta_R &: (0, 1, -2) \end{aligned} \tag{1.12}$$

in addition to the Higgs of the Standard Model, namely:

$$\Phi : (\frac{1}{2}, \frac{1}{2}, 0) \tag{1.13}$$

Since there is an additional $SU(2)_R$ symmetry, three additional gauge bosons $W_R^{\pm}$ and Z_R are introduced.

1.3.3 Fermion masses in Left-Right Symmetric Models

In this section we present an example of the calculation of fermion masses in Left-Right Symmetric Models. This calculation can be found in its original form in Ref. 10 .

The vacuum expectation values of Higgs fields are given by:

$$< \Phi >= \begin{pmatrix} k & 0 \\ 0 & 0 \end{pmatrix}, \tag{1.14}$$

$$< \Delta_R >= \begin{pmatrix} 0 & 0 \\ v_R & 0 \end{pmatrix} \tag{1.15}$$

$$< \Delta_L >= \begin{pmatrix} 0 & 0 \\ v_L & 0 \end{pmatrix} \tag{1.16}$$

where

$$v_R \ll k \tag{1.17}$$

and

$$v_L = \gamma \times \frac{k^2}{v_R} \tag{1.18}$$

The masses of fermions are determined from the lagrangian describing couplings of scalar Higgs fields to the fermions:

$$\begin{aligned} \mathcal{L}_{mass} = h_1 \overline{\psi_L} \phi \psi_R - h_2 \overline{\psi_L} \tilde{\phi} \psi_R - \\ h_3 \overline{Q_L} \phi Q_R - h_4 \overline{Q_L} \tilde{\phi} Q_R - \\ i h_5 \left(\psi_L^T C \tau_2 \Delta_L \psi_L - \psi_R^T C \tau_2 \Delta_R \psi_R \right) - h.c.. \end{aligned} \tag{1.19}$$

where :

$$\tilde{\phi} = \tau_2 \phi^* \tau_2, \tag{1.20}$$

$$< \tilde{\Phi} >= \begin{pmatrix} 0 & 0 \\ 0 & k \end{pmatrix}. \tag{1.21}$$

and C is charge conjunction matrix. Thus, from the above lagrangian electron, and

u and d quarks acquire following masses:

$$m_e = h_2 k$$
$$m_u = h_3 k \tag{1.22}$$
$$m_d = h_4 k.$$

The neutrino sector of the lagrangian is equal to:

$$\mathcal{L}^{\nu}_{mass} = h_5 \left[v_L \left(\nu_L^T C \nu_L - \nu_L^- C^+ \nu_L^- \right) + v_R \left(\nu_R^T C \nu_R + \nu_R^+ C^- \nu_R^+ \right) \right] + h_1 k (\overline{\nu_L} \nu_R - \overline{\nu_R} \nu_L) \tag{1.23}$$

One can rewrite the above equation in terms of two-component spinors $\nu \equiv \nu_L$ and $N \equiv C(\overline{\nu}_R)^T$. Using the following properties of charge conjunction matrix:

$$C^T = -C$$
$$C^2 = -1 \tag{1.24}$$
$$C \gamma_\mu C^T = -\gamma_\mu^T$$

one can obtain following relations:

$$\nu_R^+ C^- \nu_R^+ = -N^T C N$$
$$\overline{\nu}_R \nu_L = N^T C \nu = \nu^T C N. \tag{1.25}$$

Thus the equation 1.23 can be rewritten as:

$$\mathcal{L}^{\nu}_{mass} = h_5 \left(v_L \nu^T C \nu - v_R N^T C N \right) + h_1 k \nu^T C N + h.c. \tag{1.26}$$

or in the matrix form:

$$\mathcal{L} = \frac{1}{2} \begin{pmatrix} \nu^T, & N^T \end{pmatrix} \mathcal{M} C \begin{pmatrix} \nu \\ N \end{pmatrix} + h.c., \tag{1.27}$$

where $\mathcal{M}$ is given by:

$$\mathcal{M} = \begin{pmatrix} a & c \\ c & b \end{pmatrix} \tag{1.28}$$

and

$$a = h_5 v_L$$
$$b = -h_5 v_R \tag{1.29}$$
$$c = \tfrac{1}{2} h_1 k.$$

The eigenstates of this mass matrix are:

$$\nu_e = \nu \cos\xi + N \sin\xi$$
$$N_e = -\nu \sin\xi + N \cos\xi. \tag{1.30}$$

where:

$$\tan 2\xi = \frac{2c}{b-a} \approx 2c/b \tag{1.31}$$

Since $b \gg a, c$, one gets:

$$\nu_e = a - c^2/b$$
$$N_e = b \tag{1.32}$$

Using equations 1.18 and 1.29 one gets the following expressions for the light and heavy Majorana neutrino masses:

$$m_{\nu_e} = \left(h_5 \gamma + \tfrac{1}{4} \tfrac{k_1^2}{h_5} \right) \tfrac{k^2}{v_R}$$
$$m_{N_e} = -h_5 v_R. \tag{1.33}$$

The important feature of the above equation is that in the limit of mass of right-handed boson W_R approaching infinity, the mass of heavy neutrino also becomes very large, and the mass of light neutrino goes to zero:

$$M_{W_R} \to \infty \quad (that\ is\ v_R \to \infty) \tag{1.34}$$

we get:

$$m_{N_e} \to \infty$$
$$m_{\nu_e} \to 0. \tag{1.35}$$

In this case weak interactions become purely left-handed and LRSM becomes equivalent to the Standard Model. The relation between the mass of light neutrino m_{ν_e} and the mass of heavy neutrino m_{N_e} is known as the see-saw mechanism [11].

The relation between the mass of light neutrino and the mass of corresponding charged fermion can be studied by comparing equations 1.22 and 1.33. If parameter γ is small:

$$\gamma \ll \frac{h_1^2}{h_5^2} \tag{1.36}$$

then we get relation:

$$m_{\nu_e} \approx O(m_e^2/m_{W_R}), \tag{1.37}$$

which links mass of light neutrino with the mass of corresponding charged fermion.

1.3.4 Neutral Heavy Leptons in Grand Unified Theories

Neutral Heavy Leptons are also present in models attempting to unify the presently observed interactions into a single gauge theory. Examples are models with SO(10) symmetry [12] in which NHLs acquire mass through the mixing with other fermion singlets.

1.4 NHL signatures

We now describe possible experimental signatures of NHL and discuss existing limits on masses and couplings of a NHL. This discussion is based on the review article. by M. Gronau, C.N. Leung and J.L. Rosner [13], and by F. Gilman [14]. In the Standard Model of electro-weak interactions, the charged (CC) and neutral (NC) currents involving neutrinos are given by:

$$J^{\mu}_{CC} = \bar{\nu}_{eL}\gamma^{\mu}e_L + \bar{\nu}_{\mu L}\gamma^{\mu}\mu_L + \bar{\nu}_{\tau L}\gamma^{\mu}\tau_L \tag{1.38}$$

and:

$$J^{\mu}_{NC} = \bar{\nu}_{eL}\gamma^{\mu}\nu_{eL} + \bar{\nu}_{\mu L}\gamma^{\mu}\nu_{\mu L} + \bar{\nu}_{\tau L}\gamma^{\mu}\nu_{\tau L} \tag{1.39}$$

where ν_e, ν_μ, ν_τ, e, μ, and τ are the lepton spinor fields. The existence of the additional Neutral Heavy Leptons, which are isosinglets under standard $SU(2)_L$, modify these equations by introducing the admixture of the heavy states into the weak isodoublets:

$$\nu_{iL} \longrightarrow \mathcal{N}_{iL} \approx \nu_{iL}(1 - \frac{1}{2}\sum_a U_{ia}{}^2) + \sum_a U_{ia}N_a \tag{1.40}$$

Here i= e, μ, τ, and the sum is over all heavy lepton species a. The weak eigenstates are now $\mathcal{N}_{iL}$: the mass eigenstates are ν_i (light neutrino) and N_a (Neutral Heavy Lepton). The matrix U_{ia} is a unitary matrix that mixes weak eigenstates and mass eigenstates. There are several types of experiments which are sensitive to the existence of NHL:

- universality constraints:

  NHL admixture in NC and CC leads to violation of universality of the coupling

of the neutral and charged currents: the coupling of a light neutrino is decreased by the factor :

$$(1 - \frac{1}{2}\sum_{a}|U_{\nu a}|^2) \tag{1.41}$$

The unitarity requirement of the Kobayashi-Maskawa matrix, the lifetime of the τ and the measurement of $R = \frac{\Gamma(\pi \to e\nu)}{\Gamma(\pi \to \mu\nu)}$, yield the following constraints [13] :

$$\begin{aligned} U_{ee}^2 &\leq 4.3 \times 10^{-2} \\ U_{\mu\mu}^2 &\leq 0.8 \times 10^{-2} \\ U_{\tau\tau}^2 &\leq 10. \times 10^{-2} \end{aligned} \tag{1.42}$$

The constraint for the $U_{\tau\tau}{}^2$ follows from the comparison of theoretical predictions and the experimental results for the life-time of τ- meson:

$$R = \frac{\tau_\tau^{theor}}{\tau_\tau^{exp}} = 1 - \sum_{a}|U_{\tau N_a}|^2. \tag{1.43}$$

- direct searches for NHLs produced in π and K decays at rest:

  the decay of $\pi \to (e, \nu)$ is helicity suppressed by a factor of 10^{-4} for massless neutrinos, but the suppression is not effective for massive neutrinos. Thus the $\pi \to e$ decay is a favored reaction in which to search for evidence of low mass heavy neutrinos coupling to electrons. The analysis is done by searching for a monochromatic peak in the energy spectrum of e^- from π^+ decays at rest. A similar analysis is done for K decays;

- search for decays of NHLs from π, K in flight:

  a neutrino beam, in addition to its major component of light neutrinos, may con-

tain a small component of heavy neutrinos. Such neutrinos may have originated from the decay of pseudoscalar mesons, which are produced in the interaction of protons with the target, and then decay in the detector:

- heavy neutrinos originating from charmed mesons in beam-dump experiments:

  if the proton beam is dumped into a thin target, some fraction of the neutrinos have origin in the short-lived charmed particles such as D's and F's. This provides a means for searching for heavy neutrinos with masses up to 1.8 GeV. A similar analysis can be done for B meson thereby expanding the mass range up to 5.3 GeV;

- NHL produced from b quark decays in e^+e^- annihilation:

  e^+e^- colliders (for example, CESR at Cornell University , NY) , which run the center of mass (CM) energies corresponding to the production of the Υ resonances provide another possible source of NHLs: one can look for secondary (detached) vertices originating from the semi-leptonic decays of the B mesons into NHLs:

- NHL coupling to Z^0 and production in e^+e^- collisions

  in the past decade, there have been experimental searches for NHLs that couple to Z^0's produced in e^+e^- collisions. Experiments which run at CM energies below the mass of Z^0 have looked for NHLs coupling to virtual Z^0. The recent availability of LEP/SLC machines operating at the CM energies equal to the mass of the Z gauge boson has opened up the possibility to search for NHLs

arising from Z decays. Figures 1.3a - 1.3c illustrate Feynman diagrams of different processes leading to the production of NHLs in e^+e^- colliders at the Z^0 peak.

Figure 1.3a represents the feynman diagram for a production of a pair of 4th generation, sequential NHLs, $\nu_4\overline{\nu_4}$:

$$e^+e^- \rightarrow Z \rightarrow \nu_4\overline{\nu_4} \tag{1.44}$$

Since these NHLs are isodoublets under Standard $SU(2)_L$, $\nu_4\overline{\nu_4}$ pair would couple to Z^0 with same strength as a pair of light neutrinos from three known generations. However, U^2, the square of mixing matrix elements (eqn 1.40) affects the lifetime of such NHLs. The results of a search for NHLs produced in such processes have been presented by the ALEPH Collaboration [15]. The limits on the existence of such fourth generation neutrinos has been extended up to neutrino masses of 42 GeV/c^2.

Figures 1.3b and 1.3c represent the Feynman diagrams of processes leading to the production of isosinglet NHLs. The production of a pair of isosinglet NHLs, shown of Figure 1.3b:

$$e^+e^- \rightarrow Z \rightarrow \mathcal{N}\overline{\mathcal{N}} \tag{1.45}$$

is suppressed by factor U^4, relative to the production of a pair of light neutrinos, which makes present e^+e^- experiments at SLC and LEP insensitive to such processes. However, if an isosinglet NHL could be produced in association with

a light neutrino from the three known generations (Figure 1.3c):

$$e^+e^- \rightarrow Z \rightarrow \nu\overline{\mathcal{N}} \tag{1.46}$$

the coupling of such a pair of neutrinos to Z^0 would be suppressed only by a factor U^2 relative to the coupling of Z^0 to the pair of light neutrinos. Recently, the OPAL Collaboration has presented the results from a search for isosinglet NHLs produced in such processes [16]. However, high statistics neutrino scattering experiments are more sensitive to isosinglet NHLs, as will be discussed in the following sections.

1.4.1 NHL signatures in ν_μ-N scattering experiments

As mentioned in the Overview, an isosinglet NHL could also be produced in the ν-N interactions. The Feynman diagram for such a process is shown on Figures 1.1. Such a NHL would couple with suppression factor U^2, relative to the coupling of light neutrinos. The factor U^2 also affects the lifetime of an isosinglet NHL (Figure 1.2a and 1.2b). There are several characteristic signatures of NHLs that can be looked for in ν_μ-N interactions:

- Opposite sign dimuon events:

  if NHLs were produced in the neutrino-induced interactions,

$$\nu_\mu + N \longrightarrow NHL_\mu - X \tag{1.47}$$

about 10% of time the NHLs would decay through the coupling to a light neutrino and a virtual Z^0, with Z^0 materializing into a pair of muons:

$$\mathcal{NHL}_\mu \rightarrow \nu_\mu + Z' \rightarrow \nu_\mu + \mu^- \mu^- \tag{1.48}$$

Thus in the final state one would observe two muons oppositely charged. The kinematic distributions of the dimuons originating from NHL decays would be distinct from the distributions for dimuon events associated with such conventional sources as for example, charged current neutrino interactions, with the second muon coming from the decay of a D or a K meson in the hadronic showers. A search for NHL using the above signature was performed by the CCFR Collaboration using data from Fermilab Experiment E744 [17]. This search is sensitive to NHLs with masses up to 18 GeV/c^2.

- Double Vertex events:

  For a certain range of NHL lifetimes, the decay of the NHL can occur outside of the hadronic shower that is associated with the neutrino interaction. Such a decay would lead to events with two separated showers, or Double Vertex events. Here the primary shower originates from the ν interaction in which the NHL is produced and the secondary shower results from the NHL decay. The search in this channel has been conducted by two experiments: the CHARM Collaboration at CERN [18], and the CCFR Collaboration at Fermilab using a neutrino Narrow Band Beam (NBB) data [19].

Figure 1.4 illustrates the results of searches for different types of NHL.

1.5 Overview of the Thesis

This thesis describes a search for NHL using the Double Vertex signature. In Chapter 2 we give a brief description of the experimental setup, and in Chapter 3 we present the event reconstruction. The selection of NHL candidates is described in Chapter 4, and in Chapter 5 we discuss different background processes for the Double Vertex signature of NHL production and decay in our apparatus. In Chapter 6 we discuss our results and compare the experimental data with Monte Carlo calculations for NHL production and decay.

Chapter 2

The Experimental Setup

Prior to the 1985 running period, the Fermilab accelerator had undergone a major upgrade. New magnets, equipped with superconducting coils, had been installed in the Main Ring tunnel, enabling the maximum energy of accelerated protons to be raised to almost 1 TeV, giving the accelerator its name, the Tevatron. For experiments using neutrino beams, the upgrade had a twofold effect: first, it has allowed the exploration of the new, higher-energy regime (above 300 GeV), and secondly, the higher energy of primary protons has resulted in more a copious production of secondaries and thus an overall improvement in neutrino event statistics.

In this chapter we describe the Fermilab Quad Triplet Neutrino beam used in experiments E744 and E770 and summarize the main features of the CCFR Detector.

2.1 The Beam Line

2.1.1 Time Structure of the Beam

The time structure of the Neutrino Beam reflected the way primary protons were accelerated in different stages of Fermilab machine. The Linac accelerated protons using a series of radio-frequency cavities (RF cavities) in which particles received successive increments of energy. The particles were clustered in groups, so called 'RF

buckets'. A typical time spread of a RF bucket was 2 nsec, and the separation between RF buckets was about 18.6 nsec, corresponding to the period of the RF cavities. The Linac at Fermilab accepted 750 keV protons and accelerated them to an energy of 200 MeV. At that stage particle buckets were injected to the rapid cycling proton synchrotron, called the Booster. There were 84 RF buckets in a single Booster batch. After being accelerated to an energy of 8 GeV, the protons were injected into the Main Ring and finally into the Tevatron. There were 12 Booster batches in one turn of the Tevatron. Thus a fully injected Tevatron would contain about 1113 RF buckets spread uniformly around the ring. However, sometimes not all 12 batches were put into the Main Ring and the accelerator was running half full, with only about 500 buckets.

The detailed layout of the beamline is shown on Figure 2.1 .

2.1.2 Neutrino Beam Extraction

After being accelerated to an energy of 800 GeV, the protons were extracted from the Tevatron ring and directed into the Switchyard. Here beams were split between the Proton, Muon and Neutrino lines.

The protons for the Neutrino Beam Line were extracted in two to four spills, of 2 milliseconds duration (pings) for every cycle of the Tevatron (every 60 seconds) . The protons were then directed onto the primary target. The collisions of the protons with the 310 mm beryllim primary target resulted in the production of secondary particles, predominantly π and K mesons. These secondary particles were then di-

Chapter 2

The Experimental Setup

Prior to the 1985 running period, the Fermilab accelerator had undergone a major upgrade. New magnets, equipped with superconducting coils, had been installed in the Main Ring tunnel, enabling the maximum energy of accelerated protons to be raised to almost 1 TeV, giving the accelerator its name, the Tevatron. For experiments using neutrino beams, the upgrade had a twofold effect: first, it has allowed the exploration of the new, higher-energy regime (above 300 GeV), and secondly, the higher energy of primary protons has resulted in more a copious production of secondaries and thus an overall improvement in neutrino event statistics.

In this chapter we describe the Fermilab Quad Triplet Neutrino beam used in experiments E744 and E770 and summarize the main features of the CCFR Detector.

2.1 The Beam Line

2.1.1 Time Structure of the Beam

The time structure of the Neutrino Beam reflected the way primary protons were accelerated in different stages of Fermilab machine. The Linac accelerated protons using a series of radio-frequency cavities (RF cavities) in which particles received successive increments of energy. The particles were clustered in groups, so called 'RF

buckets'. A typical time spread of a RF bucket was 2 nsec, and the separation between RF buckets was about 18.6 nsec, corresponding to the period of the RF cavities. The Linac at Fermilab accepted 750 keV protons and accelerated them to an energy of 200 MeV. At that stage particle buckets were injected to the rapid cycling proton synchrotron, called the Booster. There were 84 RF buckets in a single Booster batch. After being accelerated to an energy of 8 GeV, the protons were injected into the Main Ring and finally into the Tevatron. There were 12 Booster batches in one turn of the Tevatron. Thus a fully injected Tevatron would contain about 1113 RF buckets spread uniformly around the ring. However, sometimes not all 12 batches were put into the Main Ring and the accelerator was running half full, with only about 500 buckets.

The detailed layout of the beamline is shown on Figure 2.1 .

2.1.2 Neutrino Beam Extraction

After being accelerated to an energy of 800 GeV, the protons were extracted from the Tevatron ring and directed into the Switchyard. Here beams were split between the Proton, Muon and Neutrino lines.

The protons for the Neutrino Beam Line were extracted in two to four spills, of 2 milliseconds duration (pings) for every cycle of the Tevatron (every 60 seconds) . The protons were then directed onto the primary target. The collisions of the protons with the 310 mm beryllim primary target resulted in the production of secondary particles, predominantly π and K mesons. These secondary particles were then di-

rected through the collimator onto a set of three pairs of quadrupole magnets (hence the name : Quad Triplet Beam), shown on Figure 2.2 . This set of magnets focused pions and kaons into the 340 meters long decay pipe. Particles with a wide range of momenta (both positively and negatively charged) passed through the magnet train resulting in a high flux of secondaries entering the decay pipe. A fraction of the secondary particles decayed in flight, predominantly into muons and neutrinos. The remaining flux of secondaries was stopped in a 6 meter long aluminium beam dump. The beam dump was followed by the 900 meters of steel-impregnated earth berm which was designed to filter out the muons. The resulting neutrino beam was composed of neutrinos and anti-neutrinos with a flux ratio $\nu : \bar{\nu}$ of about 2.5 : 1, reflecting the dominance of positively charged secondaries produced in proton-nucleon collision in the primary target.

The neutrino beam consisted predominantly of muon type neutrinos. The electron neutrino contamination was about 2.5% [20].

2.2 The Detector

The CCFR Detector was located in the Lab E Neutrino area, about 1474 meters downstream of the primary target. It consisted of a 690 ton Target Calorimeter and 420 ton Muon Spectrometer. The purpose of the Target Calorimeter was to form the target for neutrinos and to measure the position and the energy of the interactions. The momenta of the final state muons were measured in the Muon

Spectrometer. In the analysis presented here the acrylic counters located in the Muon Spectrometer were also used to detect secondary showers and to measure their energy. Two additional drift chamber stations were located downstream of the spectrometer. Figure 2.3 shows the layout of the experiment.

2.3 The Target Calorimeter

The detailed structure of the Target Calorimeter is shown on Figure 2.4 . The calorimeter was divided into 6 identical, movable carts. Each cart consisted of 28 3 m × 3 m × 5.2 cm steel plates, with liquid scintillation counters, [21], [22] every 2 plates (10.4 cm of steel) and drift chamber stations every 4 plates (20.8 cm of steel). There were a total of 84 target counters.

2.3.1 Scintillation counters

The scintillation counters used in the instrumentation of the calorimeter were made out of ribbed acrylic tanks filled with liquid scintillator. The counters were reinforced on the outside with polyethylene bags filled with water in order to maintain hydrostatic pressure against the steel plates. The energy of the hadronic and electromagnetic showers produced by neutrino interactions was proportional to the total light output of scintillation counters. The process of light collection can be summarized as follows: charged particles passing through the counter excited a primary scintillator fluor, which emitted ultra-violet light. The UV light was absorbed by second fluor,

which re-emitted blue light. This light travelled about 1 meter to the edges of the counters, where it was absorbed by wave-length shifter bars (plastic acrylic doped with BBQ fluor) absorbing blue light and emitting green light. This system was used to collect light from a large area (3m × 3m) counter with a minimal number of phototubes. The green light propagated by total internal reflection to the end of the bar, where it was collected by a photomultiplier tube. Four photomultipliers (RCA 6342A) located in each corner of the counters were used to read out the light output of the counters. Analog signals from the phototubes were digitized by a LeCroy 4300 FERA ADC system.

2.3.2 Drift Chambers

The positions of showers produced by neutrino interactions were determined using a system of drift chambers. The basic operating idea of these devices is as follows: as charged particles pass through the chambers, the gas in the drift chambers is ionized and the electrons drift toward the sense wires. The drift time of the electrons recorded for each hit in the chambers is translated into the position of the hit by multiplying it by the drift velocity of the electrons. The drift chamber system used in the CCFR detector has been previously described in detail [23, 24]. Here we only mention the most important features of the system. There were 42 drift chambers in the calorimeter, each with 24 drift cells. The chambers were filled a 50% argon-50% ethane gas mixture. The drift velocity of electrons was about 5 cm/μsec, which combined with the 4 nsec clock of a Nevis Transport electronic digitizing system gave

the position resolution of hits of about 250 μmeters. The dead-time induced by the Time to Digital Converters (TDC) was about 12.3 μsec, similar to the one introduced by the FERA ADC system.

2.4 The Muon Spectrometer

The Muon Spectrometer measured the momenta of the final state muons produced in neutrino interactions. The spectrometer (Figure 2.5) consisted of three 3 m long toroidal magnets, containing 1.6 m of iron each, with a 1.8 m outer radius and a 12.7 cm radius hole for the coils. The magnetic field of about 18 KGauss provided a transverse momentum kick of 2.4 GeV/c for muons passing through the entire length of the magnet. The spectrometer was instrumented with drift chambers and scintillation counters. In addition to the chambers in the middle of each toroid there were drift chamber stations, each containing 5 chambers in x and y view, after each toroid. Tracking information from the toroid chambers was used to reconstruct the trajectories of muons bending in the magnetic field and thus to measure their momenta. Additionally, there were two drift chamber stations located downstream of the last toroid in order to improve the momentum reconstruction of high energy muon tracks. The rms momentum resolution of the spectrometer was about 11% and was dominated by multiple Coulomb scattering.

2.4.1 Toroid Scintillation Counters

Each of the Toroid counters, shown on Figure 2.6, consisted of 4 quadrants of acrylic plastic scintillator and required 10 photomultipliers for the readout. There were total of 25 counters, (numbered 0 through -24) placed every 20.3 cm of steel, 8 counters per one toroid cart, and one (counter number 0) in front of whole toroid system, separated by 10.2 cm steel plate from the last target scintillation counter. These counters were used to calculate the energy of showers from interactions taking place inside the Muon Spectrometer.

2.4.2 Trigger counters

A hodoscope made of solid scintillator counters was located in the gaps between toroid carts. There were 3 planes of the counters after the first toroid (T2, H1 and H2) , and 2 planes of the counters after the second toroid (T3 and H3). These counters were in the trigger for charge current events.

2.4.3 Scintillation Counter Numbering

The target counters were numbered from 1 to 84, with counter 84 being the most *upstream* counter. The Toroid counters were numbered 0 to -24, with counter -24 being the most *downstream* counter.

2.5 Detector Triggering

The triggers selected events with several different topologies. Triggers used in this analysis are described below: the main trigger used in the search for Double Vertex events was Trigger 2 (the Neutral Current Trigger); Trigger 6 (the Straight Through Muon Trigger) was used mainly for the purpose of the energy calibration and for the calibration of the timing of hadron showers; in the analysis presented here, Trigger 1 (the Charged Current Muon Trigger) was used in the studies of non-uniformity in the neutrino beam intensity per RF bucket.

- Trigger 1 (Charged Current Muon Trigger):

  The Trigger 1 logic is shown on Figure 2.7. This trigger selected charged current neutrino interactions, with a momentum analyzed one or more muons in the final state; it required at least minimum ionizing pulse heights in the first four downstream-most calorimeter counters (counters 1 through 4) in coincidence with a signal from trigger planes in the first and the second toroid gaps, or minimum ionizing pulse heights from the first and third group of four calorimeter counters (counters 1 through 4 and 9 through 12) and a signal from trigger planes in the first toroid gap. The trigger also required that the veto counters at the front of the detector did not fire.

- Trigger 2 (Neutral Current trigger):

  The logic for this trigger is shown on Figure 2.8. This trigger selected neutral current neutrino interactions; it required 2 counters in a group of 4 adjacent

counters to be on, in coincidence with $\geq$ 10 GeV of energy deposition in 8 counters, which included both the group of 4 and the next 4 downstream counters. In the E744/E770 fiducial region, there were 36 such overlapping groups of 4 counters (in counters 80 through 3). The trigger required that the veto counters at the front of the detector did not fire.

- Trigger 6 (Straight-Through Muon Trigger):

  Figure 2.9 presents the logic for Trigger 6. It selected events with muons originating from charged current neutrino interaction upstream of the CCFR detector: this trigger required signals from at least one counter from six widely separated groups of four adjacent Target Calorimeter counters. To ensure that a muon entered the detector from upstream, counters 81 or 82 had to be on. Toroid penetration was ensured by requiring the PTOR logic to fire. The PTOR logic (Figure 2.10) selected a high energy muon by requiring the muon to traverse the same quadrant throughout the entire length of the Toroid.

2.5.1 Neutral Current Trigger Efficiency

The Neutral Current Trigger (Trigger 2) was implemented only in the Target Calorimeter. Figure 2.11 shows the distribution of the longitudinal position of ν_μ-N interactions recorded with Trigger 2. As can be seen from the figure, the sensitivity of Trigger 2 spanned between counters 82 through 8. Neutrino interactions in the detector region of counters 84 and 83 (upstream part of the Target Calorimeter), between counters 7

through 1 (downstream part of the Target Calorimeter) and counters 0 through -24 (the Toroid Spectrometer counters) could not set Trigger 2 on.

The smaller number of Trigger 2 events for the most upstream target counters implies the lower efficiency of the trigger in that region. Two effects caused the inefficiency of Trigger 2 for interactions taking place in the region between counters between 82 and 79:

1. the most upstream counters which were part of Trigger 2 logic were counters 80 and 79. Thus, short showers that started at counter 82 or 81 and did not reach counter 79 could not set the Trigger 2 logic on;

2. counters 83 and 84 were part of the veto logic rejecting interactions taking place upstream of the detector. For some fraction of the interactions in the upstream most region of the target, a backsplash of showering particles could set counters 83 and 84 on and therefore veto the event.

The efficiency of Trigger 2 as a function of shower energy was measured using the charged current trigger (Trigger 1). Figure 2.12 shows the efficiency of Trigger 2 as a function of hadron energy. Trigger 2 was fully efficient for NC interactions with E_{had} greater than 15 GeV. For NC interactions with hadronic energy of 10 GeV the efficiency of Trigger 2 was about 90%.

2.6 Comparison of the Target and Toroid Instrumentation

Below we present the comparison between the instrumentation of the Target and the Toroid:

1. The Target Calorimeter

   - scintillation counters:

     liquid scintillator counters covering the full transverse plane of the calorimeter;

   - hadron energy sampling:

     hadron energy sampling interval corresponded to about 11.6 cm of steel, (0.6 λ_{INT});

   - drift chambers:

     drift chambers were located every 20 cm of steel, every 2 counters;

2. The Toroid (Muon Spectrometer)

   - scintillation counters:

     four quadrants of solid scintillator counters with a central hole with radius $\approx$ 12.7 cm. for return of the magnet coils;

   - hadron energy sampling:

     hadron energy sampling interval corresponded to about 23.2 cm of steel, (1.2 λ_{INT});

   - drift chambers:

     drift chambers stations were located every 1.6 m of steel, every 8 counters;

These differences have resulted in differences in the resolutions for reconstruction of the hadron energy, timing and transverse vertex position of hadronic showers occurring in these two different parts of the detector.

Chapter 3

The Event Reconstruction

In this chapter we discuss the reconstruction of the event variables used in the search for Double Vertex Events.

Before going into the detail of the event reconstruction procedures we make a historical note. Traditionally, in the analysis of charged current and neutral current ν-N interactions the CCFR detector was used in the following mode: the upstream part, the Target Calorimeter, was instrumented with triggers designed to detect neutrino-induced interactions and to measure the positions and the energies of hadronic showers. On the other hand, the main function of the Muon Spectrometer was to measure the momenta of the outgoing muons in the CC ν-induced interactions. The Toroid was also instrumented with the scintillation counters, however they were only used as a part of the trigger logic.

The initial search for Double Vertex signature of NHL in the E744 data was done by S. Mishra [25] and was restricted only to the fiducial volume of the Target Calorimeter. The preliminary results of that search were very intriguing: 5 NHL event candidates were found, with less than 1 event expected from the background processes. This result provided the motivation to expand the search into the fiducial volume of the Toroid. By doing so we have substantially increased the phase space available for the decay of a assumed NHL. On other hand, the different hardware

instrumentation of the Toroid, not optimized for calorimetry, has resulted in the poorer resolution for reconstruction of the energy and the vertex positions of showers in the Toroid. Since the drift chambers were placed only every 1.6 m of iron, some of the showers were contained before reaching the drift chamber stations and could not have their transverse positions reconstructed. The fact that the Toroid counters were placed only every 20 cm of iron resulted in poorer energy resolution and poorer efficiency for the finding the showers, especially of the electromagnetic type.

The following quantities played a crucial role in search for Double Vertex signature of Neutral Heavy Leptons:

- the longitudinal and transverse positions of the two showers
- the energies associated with the upstream and the downstream shower
- the relative timing between the two showers
- the length (charged particle penetration) of each shower

We now define the above variables and describe the way they were reconstructed in the off-line analysis programs.

3.1 Vertex Position Measurement

Each vertex was characterized by its longitudinal and transverse position. The longitudinal position (z-coordinate, along the neutrino beam direction) was defined using the scintillation counters:

- PLACE (shower beginning) corresponded to the number of the most upstream counter of the group of at least 2 counters with energy deposition greater than the equivalent of 4 × minimum ionizing particle deposition (4 MIPs)
- SHEND (shower end) corresponded to the number of the most downstream counter with pulse height > 4 MIPs, followed by at least three counters each having the pulse height < 4 MIPs.

Transverse (x- and y-coordinates) positions of a shower (V_X and V_Y) were defined as the centroids of the drift chamber hits in the shower region. The TDC information from the drift chambers between counters corresponding to PLACE and SHEND was used. For the showers inside the Toroid Spectrometer, drift chambers immediately downstream of SHEND were used as well.

3.2 Measurement of Shower Energy

The basic principle of the shower energy measurement is that the energy of the interaction is directly proportional to the amount of the light produced by the particles passing through the counters. As they pass through the calorimeter, they interact with the target nucleons and new particles are created. This avalanche continues to develop until new particles loose most of their energy and are finally absorbed in the calorimeter material. Each charged particle typically deposits a minimum ionizing energy. The photons produced through the ionization process are later collected by the photomultiplier tubes (phototubes). The signals from the phototubes then prop-

agate to the ADC units where they are digitized. In order to reconstruct the total energy of the shower one needs to know following quantities:

- the gain of the counters $GAIN_i$, that is the energy deposition of a minimum ionizing particle measured in ADC counts;
- map correction functions $MAPCOR(V_X, V_Y)_i$, that is the functions which account for the fact that the light collection efficiency varied with the distance of the shower from the phototubes
- the calibration constant $CALIB$, that is the conversion factor between MIP units and GeV, for hadronic, electromagnetic and muonic interactions.

The gains of the Target Calorimeter counters and the map correction functions have been measured using muons from the CC neutrino-induced events (taken with Trigger 1) and straight-through muons (Trigger 6) . The measurement of the calibration constant was done using separate data runs, during which a hadron beam was directed onto the target carts. The energy calibration procedure of the Target Calorimeter has been described in the detail in the recent publication [26].

The energy of a shower was calculated by summing up the pulse heights from the counters in the shower region. The contribution to the shower energy from the i-th counter in the Target Calorimeter was following:

$$E_i^{Target} = \left[\frac{ADC_i[ADC\ counts]}{GAIN_i[ADC\ counts/MIP] \times MAPCOR(V_X, V_Y)_i}\right] \times CALIB^{Target} \tag{3.1}$$

3.2.1 Energy Calibration of the Toroid Counters

As mentioned earlier, some of the showers developing in the Toroid could not have their transverse vertex position defined. Thus the shower energy determination procedure in the Toroid had to be modified: the map correction functions could not be used; instead the gain constants were found by averaging the energy depositions of muons passing through the entire plane of Toroid counters (in case of the Target calibration, gains of the counters were measured using muons passing within a small central region of each counter). The calibration constant for Toroid counters was assumed to be:

$$CALIB^{Toroid} = 2 \times CALIB^{Target} \tag{3.2}$$

corresponding to the fact that the Toroid counters were separated by $\approx$ 20 cm of iron compared to the separation of $\approx$ 10 cm of iron between the Target counters. The contribution to the shower energy from the i-th counter in the Toroid was following:

$$E_i^{Toroid} = \left[\frac{ADC_i[ADC\ counts]}{GAIN_i[ADC\ counts/MIP]}\right] \times CALIB^{Toroid} \tag{3.3}$$

3.3 Energy Determination

We have used two variables to describe the energy of a shower:

- E_{PLSH} :

  this energy was found by summing the pulse heights in the counters from

PLACE to SHEND inclusive:

$$E_{PLSH} = \sum_{i=SHEND}^{PLACE} E_i, \tag{3.4}$$

where E_i is defined in equations 3.1 and 3.3 for Target and Toroid counters respectively;

- E_{PLSL} :

  E_{PLSL} was defined to contain also the energy deposited by showering particles downstream of SHEND and also the energy deposition upstream of $PLACE$, (so called 'albedo region'). The calculation of E_{PLSL} required the following steps:

  1. finding PLACE, SHEND and E_{PLSH}
  2. predicting the length of the shower L_{had}, expressed in counter units. L_{had} corresponded to the charged particle penetration of a shower; the parametrization of the length of hadronic shower as a function of its energy was extracted from the analysis of the data taken with hadron beams. (see Appendix B)
  3. summing up the energy depositions in counters between PLACE+1 and PLACE - L_{had}

$$E_{PLSL} = \sum_{i=PLACE-L_{had}}^{PLACE+1} E_i \tag{3.5}$$

3.4 Delay Correction in the Energy Calculation

The measurement of a shower energy deposited in the calorimeter depended on the difference between the trigger time and the time of the interaction. The timing of the electronics was designed so that the pulses from photomultipliers would arrive at the ADC unit about 20 nanoseconds after the start of the ADC gate. The width of the ADC gate was about 240 nsec : since the typical width of the phototube pulse was about 50 nsec, this allowed for the full integration of the signal from the counters. However in the case of two neutrino interactions uncorrelated in time, only pulses that triggered the apparatus would have proper timing with respect to the ADC gate: the other interaction could occur later (or earlier) relative to the triggering event. Therefore the pulses from the counters associated with the second interaction would arrive later (or earlier) with respect to the ADC gate. Effectively only a fraction of the pulse would be digitized resulting in a lower measured energy.

Figure 3.1 illustrates the relative timing between the ADC gate and the triggering and non-triggering pulses from phototubes. Using a special trigger setup, we have measured the fraction of the pulse that is integrated as a function of a time difference between the ADC gate and the pulse from a phototube. This measurement was verified by studying the average energy depositions of cosmic ray muons traversing the CCFR detector in the direction opposite to the neutrino beam line. Figure 3.2 shows the fraction of the phototube pulse digitized by the ADC system R_{delay}:

$$R_{delay} = \frac{ADC(\Delta T)}{ADC(\Delta T = 0)}, \tag{3.6}$$

as a function of the time difference

$$\Delta T = T_{shower} - T_{ADCgate}. \tag{3.7}$$

We should note the fact that the function R_{delay} is not symmetric in respect to $\Delta T = 0$: for negative ΔT (shower arriving before the ADC gate opened i.e. the rising edge of the pulse has been 'chopped off') the drop-off is much faster than for positive ΔT (shower arrived after ADC gate opened, and only some part of the tail of the pulse has been 'chopped off').

Thus in the calculation of the energy for 'out-of-time' (non-triggering) showers we have applied the following correction:

$$E_{sh}^{corr} = E_{sh} \times \left[\frac{1}{R_{delay}(\Delta T)}\right] \tag{3.8}$$

3.5 Efficiency of finding showers

The efficiency of finding Double Vertex events depended on two factors: the efficiency of Trigger 2 and the efficiency of finding the second, non-triggering shower. As discussed earlier, the software condition for finding a shower required two consecutive counters to register pulse heights greater than 4 MIPs. This pattern recognition was done using pulse heights not corrected for the timing delay relative to the ADC gate, since at that point of the analysis the timing of the shower has not been yet established. Therefore the fraction of showers that could be found using the above algorithm depended on the relative timing between the ADC gate and the timing of the shower.

We have studied the efficiency of the shower finding code using single vertex neutrino-induced interactions. In order to imitate non-triggering showers we have defined a parameter $ECUT$:

$$ECUT(\Delta T) = \frac{4MIP}{R_{delay}(\Delta T)}, \tag{3.9}$$

and then searched for showers with energy depositions in two consecutive counters greater than $ECUT$:

$$ADC_i > ECUT(\Delta T)$$

$$ADC_{i-1} > ECUT(\Delta T).$$

Then the shower finding efficiency was defined as:

$$Eff_{sh}^{Target}(E_{sh}, \Delta T) = \frac{\#\ of\ showers\ found\ with\ ECUT(\Delta T)}{\#\ of\ showers\ found\ with\ ECUT(\Delta T = 0)} \tag{3.10}$$

Figure 3.3 shows the shower finding efficiency in the Target as a function of shower energy E_{sh}, for different values of ΔT.

Since the Trigger 2 was only implemented in the Target Calorimeter the above function (eqn. 3.10) did not reflect the efficiency of finding showers from interactions in the Toroid. Since the energy sampling interval in the Toroid was twice as big as that of the Target Calorimeter, the efficiency of finding showers in the Toroid was lower.

To estimate the efficiency of finding showers in the Toroid we have used following scheme:

- we have selected a sample of neutrino interaction in Target Calorimeter
- we have imitated Toroid energy sampling interval by using only every second Target counter in the search for the showers

$$ADC_{2i} > ECUT(\Delta T)$$

$$ADC_{2(i-1)} > ECUT(\Delta T).$$

- we have defined the efficiency of finding showers in Toroid for non-triggering showers, Eff_{sh}^{Toroid} as:

$$Eff_{sh}^{Toroid}(E_{sh}, \Delta T) = \frac{\#\ of\ showers\ found\ with\ ECUT(\Delta T)}{\#\ of\ showers\ found\ with\ ECUT(\Delta T = 0)}; \tag{3.11}$$

where in the numerator and in the denominator we have included showers found using only even-numbered Target counters.

Figure 3.4 shows shower finding efficiency in the Toroid, as a function of shower energy E_{sh}, for different values of ΔT.

It is important to realize that the above function (eqn 3.11) reflects only the efficiency of finding non-triggering showers in Toroid, which have similar ratio of hadronic to electromagnetic components as ν_μ-induced interactions. The inefficiency caused by the less frequent energy sampling interval in Toroid would be more significant for showers with high electromagnetic component.

3.6 Timing Determination

As mentioned earlier, the pulses from the phototubes were split and signals sent to both the ADC and TDC systems. The TDC system has been described in the detail in ref. [23]. The TDC information from the counters was used to establish the timing of showers relative to the trigger time. In order to achieve good timing resolution the following corrections were considered:

- pulse height slewing correction:

  signals with bigger pulse heights would cross the TDC discriminator threshold earlier than signals with lower pulse heights, thus contributing a spread of the timing. The correction accounting for this effect has been measured by comparing the timing from single counters with the averaged time from all counters in the shower region and plotting the difference as a function of the pulse heights of individual counters (see Figure 3.5). The resolution of the timing from individual counters, shown in Figure 3.6 has been calculated as a function of a energy deposited in a given counter. The inverse of the square of the timing resolution function of single counters was used as a weighting factor in the calculation of the average timing for the entire shower.

- correction for time of flight of photons across the counter plane:

  depending on the transverse distance of the shower to the closest phototube, the time of flight of photons to the phototubes varied: to account for this effect we have applied a position dependent correction. This correction was especially

  important for the Target Calorimeter counters, since their transverse dimensions (3 m × 3 m) could lead to time of flight difference of up several nanoseconds. Since the acrylic counters in the Muon Spectrometer were smaller (1.5 m × 1.5 m) this effect was less significant. Some of the showers in the Toroid could not have their transverse position defined : in such an instance, it was assumed that the shower was located in the center of a counter.

Due to the presence of the electronic noise in the TDC system, an iterative method had to be followed in order to measure the timing of a shower. A crude estimate of the shower timing was found using an overlapping-bin method, i.e. the timing of a shower was defined to be a center of the time bin with the highest number of the TDC hits from the counters within the shower region. Here the shower region was defined as counters between $PLACE$ and $SHEND$. Additionally, up to three counters downstream of $SHEND$ were included, if their pulse heights were above 2 MIPs. In the following iterations the weighted average of the hits from the most populated bin was calculated and the pulse-height and position corrected TDC hits away from the average by more than 2 σ (twice the resolution of the timing of an individual counter) were removed from the sum. Thus the final expression for the timing of a shower was following:

$$T_{shower} = \frac{\sum_i [TDC_i - COR_{PH}(ADC_i) - COR_{XY}(V_X, V_Y)] \times w_i}{\sum_i w_i}, \qquad (3.12)$$

where w_i was a weight equal to the square of the inverse of the resolution of the timing of individual counters:

$$w_i = \frac{1}{\sigma^2(ADC_i)}. \tag{3.13}$$

After the above corrections were taken into account, the resolution of the timing of a single shower was measured using events with muons in the final state, since the timing information for such events was independently available from the muon track. A sample of charged current neutrino-induced interactions was selected and the timing of the hadronic shower compared with the reference time T_{REF}. T_{REF} was an independently established time based on muon timing information from the drift chambers and from the trigger hodoscopes. Figure 3.7 shows the resolution of the timing for the showers occurring in the Target,

Trigger 1 was not implemented for neutrino interactions in the Toroid, therefore the only possible way to measure the resolution for showers in the Toroid was to use muons which developed shower cascades, originating from such stochastic processes as bremsstrahlung, e^+e^- and photonuclear interactions, so called "deep-μ" showers. Figure 3.8 shows the resolution of the timing for the showers occurring in the Toroid. Note that the timing resolution of the Toroid, as measured from "deep-μ" showers, was primarily for electromagnetic showers, since muon interactions are predominantly from electromagnetic processes.

3.7 Shower Length Determination

The length of each shower, was defined as the number of counters (each Target counter was separated by material corresponding to about 11.6 cm of iron) traversed by the most penetrating charged particle. The length of a shower was used to provide the basis for differentiation between NC-type showers (without muons) and CC-type showers (with muon).

We have introduced the variable SBEND (SBit END), which corresponded to the number of the downstream most counter with SBIT (TDC hit from scintillation counter) associated with the shower followed by at least three consecutive counters with no SBITs on (or no SBITs associated with the shower) A counter was considered to have its SBIT on associated with the shower if:

$$|T_{SBIT} - T_{shower}| \leq 28\ nsec \tag{3.14}$$

The TDC discriminator threshold corresponded to about $\frac{1}{4}$ MIP energy deposition. Because of the hole in the Toroid, the Toroid counters did not cover the whole transverse plane of the detector. Sometimes this resulted in a discontinuity in the strings of SBITs associated with muons emerging from the shower. Thus for showers developing inside or continuing to the Muon Spectrometer we have searched for the end of the most penetrating charged particle starting at the most downstream Toroid counter (counter -24) and searched for two consecutive counters with SBITs associated the shower. The most downstream counter from that pair was defined to be SBEND.

Then the L_{sh}, the length of the shower, was defined as:

$$L_{sh} = (\sum_{i=PLACE}^{SBEND} L_i) \tag{3.15}$$

where:

$$\begin{aligned} L_i &= 1 \ for \ i \geq 0(\ Target \ counters) \\ L_i &= 2 \ for \ i < 0(\ Toroid \ counters) \end{aligned} \tag{3.16}$$

Here each Toroid counter contributed doubly to the length of the shower, since the Toroid counters were separated by about twice the amount of iron as compared to the Target counters.

Since the TDC hits were recorded in $\pm$ 1 μsec window around the trigger time, the above definition of the shower length was not biased for non-tiggering showers.

3.8 Distinction between NC and CC showers

In order to study different decay channels of an assumed NHL we have distinguished between NC-type and CC-type showers. This distinction was based on the length of the shower. For NC showers this variable corresponded to the length of hadronic shower, while for CC events it was normally much larger due to the penetration of the muon.

The length of hadronic showers depends on the energy of the interaction. Using the test beam data taken with hadron beams directed onto the Target Calorimeter, we have parametrized the length of a shower as a function of its energy. The shower was classified as NC-type if the actual length of the shower L_{sh}, defined in eqn. 3.15.

was less than or equal to the length of a hadronic shower L_{had} with energy E_{sh}[1]:

$$L_{sh} \leq L_{had}(E_{sh}). \tag{3.17}$$

Otherwise the shower was classified as CC-type shower.

3.8.1 Contaminations of NC and CC classes

The above algorithm classified showers into two classes: the NC-type class and the CC-type class. It is important to realize that although the NC-type class contained predominantly showers without muons, it also contained showers with very low energy muons that ranged out inside the hardonic shower or with muons that exited the detector through the sides and did not penetrate the counters downstream of the hadronic shower. Additionally, a small number of cosmic ray showers interacting at the edges of the fiducial volume of the detector, contributed to the NC-type class.

The contamination of CC events in the NC-type sample can be seen by studying the ratio of NC-type showers to CC-type showers $R_{NC/CC}$. Figure 3.9 shows this ratio as a function of the radial position of the interaction inside the Target Calorimeter for interactions with hadronic energy greater than 15 GeV taken with Trigger 2. The increase of $R_{NC/CC}$ for larger radii is caused by increasing number of CC interactions with muons escaping from the fiducial volume of the detector and due to cosmic ray interactions at the edges of the detector.

[1] The detailed description of hadronic shower length parametrization can be found in the Appendix B.

The average ratio $R_{NC/CC}$ for single vertex events within the fiducial volume of square $\pm$ 50 inches and a radius cut of 60 inches was:

$$< R_{NC/CC} >^{Target} = 0.40 \pm 0.01 \tag{3.18}$$

We should also add that in the case of ν_e-N interactions, both NC and CC interactions would fall into NC-type category, since the electron emerging from the charged current interaction would be contained inside the hadronic shower.

The poorer reconstruction of neutrino interactions in the Toroid has led to the larger contamination of CC interactions in the NC-type class for showers occurring in the Toroid. The fraction of CC events with final state muon escaping the detector increased. since the transverse position of the shower could not be reconstructed and interactions occurring at the edges of the detector were included in the sample. Additionally, with larger fiducial volume (no transverse position cut) the fraction of cosmic ray background was also larger.

Since the Toroid counters were not part of the Trigger 2 logic, the measurement of $R_{NC/CC}$ ratio for interactions occurring in the Toroid could not be done directly. Instead we used single vertex neutrino interactions inside the Target Calorimeter and applied the analysis which mimicked the hardware instrumentation of the Toroid. We doubled the energy sampling interval by using only even-numbered counters in the shower finding algorithm , in the calculation of the energy of interactions and the assignment of the type of the interactions. Additionally, in the above analysis we did not restrict the fiducial volume of the Target Calorimeter to $\pm$ 50 inches square. The

result of this measurement is presented on Figure 3.10. The ratio $R_{NC/CC}$ in Toroid, is plotted as a function of radial position of a neutrino interaction. It demonstrates increasing level of the contamination of NC-type class by CC neutrino interactions at the outer edges of the fiducial volume of the Toroid. The averaged ratio of NC-type to CC-type neutrino interactions calculated in the analysis imitating the Toroid instrumentation was equal to :

$$< R_{NC/CC} >^{Toroid} = 0.60 \pm 0.02. \tag{3.19}$$

systematically higher than the average value of the ratio of NC-type to CC-type interactions inside the Target, $< R_{NC/CC} >^{Target}$.

Chapter 4

The Event Analysis

4.1 Overview

In this chapter we discuss the event analysis performed as a part of the search for NHL in ν_μ-N interactions. As mentioned before, we concentrate in this analysis on the search for the Double Vertex signature, that is the search for the events with two showers: the upstream shower associated with the incoming neutrino interaction, and the downstream shower originating from the decay of the assumed Neutral Heavy Lepton. The topology of such an event is depicted in the Figure 4.1.

There are two major conventional physics background sources of such events:

- neutral hadron punch-through events:

  In ν-N interactions, neutrons and K_L^0 produced in the primary hadronic vertex or in the secondary interactions of the hadrons inside the primary shower may penetrate and interact downstream of the end of the primary shower (Figure 4.2); these 'neutral punch-through events' are the dominant background for the Double Vertex events with small separation between the showers

- random overlay events:

  A certain fraction of the time, two independent neutrino interactions will take place inside the fiducial volume of the detector and within the timing gate of

  the trigger (Figure 4.3); depending on the time difference between these two interactions and the timing resolution of our apparatus they may or may not look like the simultaneous events. These 'random overlay events' are the main source of the background for the Double Vertex events with long separation between the showers.

- other backgrounds:

  Additional background events that mimick 'Double Vertex Events' could arise from cosmic ray showers happening within the ADC gate of the system, or from particle showers interacting at the edges of the detector and being not fully absorbed within the fiducial volume of the target iron plates, in effect scraping the side of the detector.

We now describe the selection criteria for the Double Vertex events. The calculation of background sources of Double Vertex events originating from such conventional processes as neutral hadron punch-through and random coincidences of uncorrelated neutrino interactions is presented in the following chapter.

4.2 The Event Selection

There were three topological components of the Double Vertex Event selection:

1. the cuts selecting the upstream shower;

2. the cuts selecting the downstream shower:

3. the cuts designed to ensure that the region between the upstream and downstream showers was 'quiet', ie there were no particles penetrating that region during the time of the interaction.

The selection of the Double Vertex events was done in two passes. Below we list the cuts used in the selection of the preliminary sample.

4.2.1 First pass cuts

- Trigger cuts:

  1. event should be triggered by Trigger 2, with Trigger 6 not firing
  2. event should be taken during Fast Spill gate (IGATE=1,2,3 or 4), corresponding to fast spill pings 1 - 4.

- Upstream shower cuts:

  1. finding an upstream shower, and requiring that its longitudinal vertex position, PLACE was between counter 1 (downstream most counter in Target Calorimeter) and counter 82:

$$82 \geq PLACE_1 \geq 1$$
$$82 \geq SHEND_1 \geq -8 \tag{4.1}$$

  2. defining transverse position V_{X1} and V_{Y1}
  3. calculating E_1^{PLSH}

  4. determining the timing (relative to the ADC gate) of the upstream shower T_{sh1}
  5. applying timing correction to the energy and requiring:

$$E_1^{PLSH\ corr} \geq 7.5\ GeV \tag{4.2}$$

- Cuts selecting downstream shower.

  1. searching for downstream shower and requiring that:

$$82 \geq PLACE_2 \geq -14$$
$$82 \geq SHEND_2 \geq -24 \tag{4.3}$$

  2. defining transverse position V_{X2} and V_{Y2}
  3. calculating map-corrected energy E_2^{PLSH}
  4. determining the timing (relative to the ADC gate) of the downstream shower T_{sh2}
  5. applying timing correction to the energy and requiring:

$$E_2^{PLSH\ corr} \geq 2.1\ GeV \tag{4.4}$$

- Cuts selecting 'quiet gap region'

  1. defining 'quiet gap region' as the region between end of the upstream shower and beginning of the downstream shower. Thus the 'quiet gap region' corresponded to the counters:

$$SHEND_1 - 1 \longrightarrow PLACE_2 + 1 \tag{4.5}$$

and the number of counters in the 'quiet gap region' N_{sepa}, was equal to :

$$N_{sepa} = (\sum_{i=PLACE_2+1}^{SHEND_1-1} 1), \tag{4.6}$$

2. requiring one of the following 3 conditions:

   (a) at least half of the counters in the 'quiet gap region' had map-corrected pulse heights such that :

$$PH_i^{map\ corr} \leq 0.5\ MIP \tag{4.7}$$

   (b) the average pulse height in the 'quiet gap region' :

$$< PH >_{GAP} = \frac{1}{N_{sepa}} \left[\sum_{i=PLACE_2+1}^{SHEND_1-1} PH_i^{map\ corr} \right] \leq 0.5\ MIP \tag{4.8}$$

   (c) if there was more than 10 counters in the 'quiet gap region':

$$N_{sepa} \geq 10 \tag{4.9}$$

   than the region between the showers was quiet if any of 10 consecutive counters within 'quiet gap region' would satisfy one of the criteria 2.a) or 2.b) listed above.

4.2.2 Second pass cuts

All events that have passed the above set of preliminary cuts were subject to the second pass analysis. In the second pass we recalculated variables the $PLACE_1$, $SHEND_1$, $PLACE_2$, $SHEND_2$ so that these variables were based on the counter

pulse heights after map correction and timing delay correction have been applied:

$$PH^{corr} = \frac{PH^{raw}}{MAPCOR(V_X, V_Y) \times R_{delay}(\Delta T)} \tag{4.10}$$

For counters upstream of $PLACE_2 + 1$ the delay correction was calculated based on the timing of the upstream shower T_{sh1}, and for counters downstream of $PLACE_2 + 1$ the delay correction was based on the timing of the downstream shower T_{sh2}. In the second pass analysis we have also applied more stringent fiducial volume, energy and timing cuts:

- <u>Upstream shower cuts:</u>

  1. longitudinal position of the upstream shower:

$$\begin{aligned} 82 \geq PLACE_1 \geq 10 \\ 82 \geq SHEND_1 \geq -8 \end{aligned} \tag{4.11}$$

  2. transverse position of the upstream shower:

$$\begin{aligned} |V_{X1}| \leq 50" \\ |V_{Y1}| \leq 50" \\ r_{sh1} = \sqrt{(V_{X1})^2 + (V_{Y1})^2} \leq 60" \end{aligned} \tag{4.12}$$

  3. energy of upstream vertex:

$$E_{sh1} = E_1^{PLSL\ corr} \geq 15\ GeV \tag{4.13}$$

  4. upstream shower type assignment:

     to ensure that there was no minimum ionizing particle emerging from the

upstream shower, we required that the upstream vertex was NC-type, as defined in previous section.

- Downstream shower cuts:

1. longitudinal position of the downstream shower:

$$82 \geq PLACE_2 \geq -14$$
$$82 \geq SHEND_2 \geq -24 \tag{4.14}$$

At this point we have separated the events into 2 classes:

(a) Target Events

Events for which the downstream shower has started within the Target Calorimeter:

$$PLACE_2 \geq 3 \tag{4.15}$$

were called Target events: both upstream and downstream showers were contained inside the Target Calorimeter, which guaranteed that the transverse positions of both showers could be calculated.

(b) Toroid Events

Toroid events were events with the upstream interaction inside the Target Calorimeter and the downstream shower beginning at the downstream edge of the Target or within the Toroid Spectrometer:

$$2 \geq PLACE_2 \geq -14 \tag{4.16}$$

The above ensured that there was at least 2.3 m of iron in the Toroids downstream of the interaction. This was required for the identification of muons emerging from the shower, based on the depth of the penetration of minimum ionizing particle.

2. transverse position of the downstream shower:

(a) For Target events we have applied the transverse position cuts on the downstream shower:

$$|V_{X2}| \leq 50''$$
$$|V_{Y2}| \leq 50'' \tag{4.17}$$
$$r_{sh2} = \sqrt{(V_{X2})^2 + (V_{Y2})^2} \leq 60''$$

(b) For Toroid events, we did not impose any transverse position cuts on the downstream shower, since some of the showers could not have their transverse position defined.

3. the energy of downstream vertex:

here for both, Target Events and Toroid Events we applied same cut:

$$E_{sh2} = E_2^{PLSL\ corr} \geq 15\ GeV \tag{4.18}$$

- Cuts selecting 'quiet gap region'

1. material separation between two showers L_{steel}, expressed in units corresponding to the amount of material separating adjacent Target Calorimeter

counters, be greater than 5:

$$L_{steel} = \left[\sum_{i=PLACE_2+1}^{SHEND_1-1} L_i \right] > 5, \tag{4.19}$$

where:

$$\begin{aligned} L_i &= 1 \; for \; i \geq 0(\; Target \; counters) \\ L_i &= 2 \; for \; i < 0(\; Toroid \; counters) \end{aligned} \tag{4.20}$$

Target counters were separated by about 11.6 cm of equivalent steel, while the material separation between two Toroid counters was corresponding to about 23.3 cm of steel. Therefore, the above cut corresponded to requirement that the beginning of the downstream shower was separated from the end of the upstream shower by material equivalent to at least 70 cm of steel.

2. requiring 'quiet gap' based on a counter pulse heights, conditions 2.a), 2.b), or 2.c) as described in the previous section.

3. an additional 'quiet gap' cut required that in the 'quiet gap region' there were at least half of the counters with no SBIT hits associated with T_{sh1} nor with T_{sh2}. If the counter separation between the two showers, N_{scpo} was greater than 10, the region would be defined as quiet, if in any group of 10 consecutive counters within the 'quiet gap region' at least five of the counters had no SBIT hits associated with T_{sh1} nor with T_{sh2}.

4.2.3 Angle between the upstream and the downstream showers

We have defined the angle between the direction of the neutrino beam and the line joining the beginning of the upstream and the downstream showers as θ :

$$\theta = \arctan \sqrt{\frac{(\Delta V_X)^2 + (\Delta V_Y)^2}{(\Delta V_Z)^2}} \tag{4.21}$$

As will be discussed in the Chapter 6.4, the predicted angular distribution of assumed NHLs with the mass in the range of 0.5 GeV/c^2 to 3 GeV/c^2 (the sensitivity of our experiment to the Double Vertex signature of NHL is limited to that mass range) is very narrow and over 98% of the assumed NHLs would be produced at the angles θ_{NHL}, less than 125 mrads.

Therefore, for the events with both showers contained inside the Target, we have applied the following cut:

$$\theta \leq 125 \; mrad \tag{4.22}$$

For events with the downstream shower contained inside the Toroid, the above cut was not applied, because the downstream shower vertex position could not be defined for a fraction of the events.

4.2.4 Selection of In-Time Events

So far in the analysis, the timing information was used only to correct the energy of non-triggering showers and to ensure the absence of the minimum ionizing particle penetrating into the gap between the upstream and downstream showers. The sample

of events selected with the above described cuts contained both NHL candidates and the events coming from conventional background sources. The background sources include NC neutrino interactions with neutral punch-through showers, and events originating from random overlays of two independent neutrino-induced interactions.

For NHL candidates and single vertex neutrino NC interactions with neutral hadron punch-through showers, the timing difference between the upstream and downstream showers should be zero, within the timing resolution. On other hand, the random overlay events were uncorrelated in time. For some of these the timing difference would be within the timing resolution of the detector, while others would appear as the Out-of-Time events. In order to select NHL candidates and estimate the background originating from random overlays we have used cuts based on the timing of the upstream and downstream showers. Figure 4.4 shows the distribution of the relative timing between the upstream and the downstream showers for Target events and for Toroid events. The multi-peaked structure of this distribution reflects the time structure of the accelerator beam, where particles are bunched into RF buckets. Each bucket is separated by about 18.6 nanoseconds. The intrinsic time spread of RF buckets is about 2 nanoseconds, and the total r.m.s. resolution of the timing difference between two uncorrelated showers is about 3.5 nanoseconds.

In order to select events correlated in time (later referred to as the In-Time events), we have required that the absolute value of the timing difference between the upstream and downstream shower is less than $\frac{1}{2}$ of time separation between two consecutive RF

buckets:

$$|T_{sh1} - T_{sh2}| \leq \frac{1}{2}\ RF \approx 9.3\ nsec \tag{4.23}$$

NHL candidates, neutral hadron punch-through events and accidental overlays of two neutrino interactions coming from same RF bucket were included in this category. Based on the timing resolution studies presented earlier, we estimated that the above timing cut was over 99% efficient for the class of events with both the upstream and downstream shower contained inside the Target Calorimeter (Target events) and about 96% efficient for the class of events with upstream interaction inside the Target Calorimeter and a the downstream shower inside the Toroid (Toroid events).

4.3 Classification of In-Time Events

The sample of Double Vertex In-Time Events was visually scanned. The sample was then subdivided into several classes based on the amount of material separation between the two showers and on the presence or absence of high energy muon in the downstream shower.

4.3.1 Event Scanning

The purpose of the visual scanning of events was to verify the computer algorithm selection of Double Vertex events. The topology of Double Vertex events was based on the presence of a 'quiet gap region' between the end of the upstream and the beginning of the downstream showers. Intermittent hardware failure of the counters or

mulfunctioning of the readout electronics could result in the apparatus not registering energy depositions or SBIT hits in a group of counters. In such a case, a single charged current neutrino interaction could imitate the topology of a Double Vertex event. This possibility could be checked by looking at the hits in the drift chambers in the 'quiet gap region' of such events.

The visual scan of Target Events (i.e. events with the downstream shower starting inside the Target Calorimeter). resulted in rejection of two CC neutrino interactions that passed the selection criteria for In-Time Double Vertex events. In these events, the quiet gap was a result of hardware failure of the counters or a downward fluctuation of the energy deposition of a final state muon in conjunction with a downstream shower from electromagnetic interaction of the muon with the target nuclei.

As mentioned earlier, the Toroid counters consisted of four quadrants with a hole for the return of the magnet coils. Therefore Toroid counters did not cover the entire transverse cross-section of the Muon Spectrometer. That in effect caused inefficiency in identifying muons from charged current neutrino interactions in the downstream part of the Target Calorimeter. for which a final state muon penetrated the central hole region of the Toroid. mimicking a 'quiet gap region'. As the muon emerged from the hole. it intersected the active area of the downstream counters and deposited energy in them. However. the drift chamber stations in the Toroid would record the track, and such events could be rejected in the visual scanning process. As a result of the scanning process of In-Time Toroid events, 13 such CC neutrino interactions

with muon passing through the Toroid hole were found and rejected from the sample of Double Vertex events.

Another drawback in the analysis of Toroid Events was the inability to define the transverse vertex positions for some of the showers found inside the Toroid. This resulted in a selection of neutrino interactions at the edges of the fiducial volume of the Target Calorimeter with a muon passing through the outer most section of Toroid counters. again mimicking Double Vertex events. Seven such events were found in sample of computer selected In-Time Toroid events and were removed from the Double Vertex sample.

Using the computer selection algorithm described above. a total of 192 In-Time Double Vertex Events were found. The sample included 123 Target events (with both showers occurring inside the Target Calorimeter) and 69 Toroid events (with downstream shower occurring inside the fiducial volume of the Toroid Spectrometer). As the result of visual scanning, 121 events remained in the Target In-Time sample and 49 events remained in the Toroid In-Time sample. Table 4.1 summarizes the numbers of In-Time Double Vertex events selected by the computer analysis and number of events remaining after the visual scanning process.

4.3.2 Material separation between the upstream and downstream showers

As a hadronic cascade develops inside the calorimeter, a certain fraction of the time high energy neutral hadrons with long lifetimes (i.e. neutrons and neutral K mesons)

are produced. Since these hadrons are electrically neutral, they do not deposit ionizing energy in the scintillation counters unless they interact with target nuclei and produce a secondary hadronic shower. The separation between the primary and secondary cascades depends on the interaction cross-section of neutral hadrons. The nuclear interaction length, λ_{INT}, for neutral hadrons is equal to the mean free path between inelastic interactions[1]. Therefore, in the NC neutrino interactions, secondary showers produced by neutral hadrons, which interacted downstream of the end of the primary shower contributed to the In-Time Double Vertex sample. The rate of these neutral hadron punch-through events depended on the amount of material between the end of upstream shower and the beginning of the downstream shower, L_{steel} (as defined in Eqn 4.19). Therefore we have subdivided the sample of In-Time Double Vertex events into three classes:

1. Small separation:

$$6 \leq L_{steel} \leq 10 \tag{4.24}$$

2. Intermediate separation:

$$11 \leq L_{steel} \leq 20 \tag{4.25}$$

3. Large separation:

$$L_{steel} \geq 21 \tag{4.26}$$

[1] In the CCFR detector the separation between counters in the Target Calorimeter corresponded to about $0.6\lambda_{INT}$ (the separation between Toroid counters was about $1.2\lambda_{INT}$).

The neutral hadron punch-through background for each of the above classes is described in detail in the next chapter.

4.3.3 Shower type of secondary vertex

In the earlier stage of the analysis, we have required that the upstream shower was classified as NC-type, in order to ensure the absence of a minimum ionizing particle in the gap between two showers. Here we classify events depending on the assignment of the downstream shower:

1. NC $\rightarrow$ NC events

   this class contained events with the downstream shower classified as NC-type

2. NC $\rightarrow$ CC events

   this class contained events with the downstream shower classified as CC-type.

The above classification was introduced in order to categorize Double Vertex events on the basis of the presence (or absence) of a high energy muon among the decay products of the assumed NHL.

The presence of the hole in the Toroid counters has resulted in poorer efficiency in the identification of muons emerging from the downstream shower in the Toroid. If a muon travelled through the hole then the algorithm would fail to identify it and the event would be incorrectly assigned to the $NC \rightarrow NC$ group. On other hand, since the parametrization of the length of hadronic showers was extracted using the Target Calorimeter, the different material densities in Target and Toroid

introduced the systematic uncertainty of the shower length parametrization and lead to misidentification of NC showers. Therefore we have scanned the Toroid In-Time sample and assigned them to the $NC \rightarrow NC$ or the $NC \rightarrow CC$ group based on the presence (or absence) of muon as registered by the drift chamber stations in the Toroid. The comparison of the shower type assignment based on shower length algorithm done by computer with the assignment based on visual scan has yielded following results:

1. Clear NC events

   We found 23 events which had the downstream shower assigned to the NC-type group based on shower length algorithm and no muon track emerging from the downstream shower.

2. Marginal NC events

   There were 4 events which had the downstream shower identified as CC-type, based on the length of the shower, but there was no muon penetrating the Toroid downstream of it.

3. Clear CC events

   There were 20 events with CC-type classification of the downstream shower and momentum analyzable muon emerging from the shower .

4. Clear CC events, but NC according to length algorithm

   We found 1 event with clear muon emerging from the downstream shower.

   (based on drift chamber information), for which the length algorithm classified it as NC-type.

5. Ambigious CC events

   We found 1 event, with downstream shower classified as CC-type on basis of shower length algorithm, with muon track present, but not momentum analyzable.

As the result of the visual scanning of Toroid events, events from 'Clear NC' group and 'Marginal NC' group were included in the $NC \rightarrow NC$ channel, while events from remaining three groups fell into the $NC \rightarrow CC$ channel.

Table 4.2 and 4.3 summarize the number of Double vertex events in each of the above described categories.

Chapter 5

The Background Estimation

5.1 Overview

Different types of backgrounds play the dominant role for each of the classes of events described in the previous chapter. The background for NHL in the $NC \rightarrow CC$ channel came predominantly from random overlay events. In case of the $NC \rightarrow NC$ channel, the background for Small Separation events was dominated by the neutral hadron punch-through events. In the Intermediate Separation region both neutral hadron punch-through events and random overlay events contribute to the background, and for the Large Separation $NC \rightarrow NC$ events, the background originated almost exclusively from random overlay events. We now discuss the ways in which the background sources of Double Vertex events were estimated. At the end of this chapter we compare the background estimates with the number of observed NHL candidates.

5.2 The Random Overlay Background

As mentioned earlier, In-Time events with timing difference between the upstream and downstream showers:

$$|T_{sh1} - T_{sh2}| \leq \frac{1}{2}\ RF \tag{5.1}$$

could arise from random coincidence of two uncorrelated neutrino-induced interactions. Since the resolution of the relative timing between two showers was about 3.5 nsec as compared to the 18.6 nsec separation between two adjacent RF buckets, virtually all of these coincidences originated from interactions of neutrinos from same RF bucket.

5.2.1 Selection of Out-of-Time Events

In order to estimate the random overlay contribution to the background of Double Vertex events, we have searched for overlays of neutrino interactions uncorrelated in time, i.e. from different RF buckets. The selection of Out-of-Time events was performed using the cuts described in Sections 4.2.2 and 4.2.3. These cuts were designed not to introduce any biases between In-Time and Out-of-Time events.

The timing range for Out-of-Time events was determined to ensure full Trigger 2 efficiency and high efficiency of finding hadron shower associated with the non-triggering interactions:

- Triggering efficiency:

  Only counters 80 through 8 inclusive were part of the Trigger 2 logic. Interactions with showers starting in the upstream counters 81 or 82 triggered this logic only if showers penetrated into or downstream of counter 79.

- Finding non-triggering showers:

  The shower-finding algorithm was based on energy depositions in the counters.

as digitized by the ADC system. For non-triggering showers the timing of the ADC gate was not correlated with timing of pulses from PMTs. This resulted in a lower efficiency of finding the non-triggering showers which were 'out-of-time' relative to the interaction that set the trigger on.

For the events with both interactions taking place inside the region of full Trigger 2 efficiency (counters 80 through 8), the interaction occurring first would always trigger the apparatus. Therefore the non-triggering interaction would always appear as late relative to the ADC gate:

$$\Delta T = T_{sh,\ non-trig} - T_{ADC\ gate} \geq 0 \tag{5.2}$$

However, for Double Vertex events in which one of the interactions took place in the region where Trigger 2 was not fully efficient (counters 81 or 82) or not implemented (counter 7 through -14), the non-triggering interaction could appear as late or as early relative to the ADC gate. The delay correction function $R_{delay}(\Delta T)$ for 'late' (with $\Delta T > 0$) interactions was a slowly changing function of ΔT. For 'early' interactions (with $\Delta T < 0$), the delay correction function was strongly dependent on ΔT (see Figure 3.1). Therefore we have used only events, for which the non-triggering interaction occurred after the triggering one:

$$T_{sh,\ non-trig} - T_{sh,\ trig} \geq 0 \tag{5.3}$$

In order to preserve high efficiency for finding non-triggering showers (Figures 3.2 and Figure 3.3) we required that the time separation between two uncorrelated inter-

actions in Out-of-Time events be no more than 160 nsec (160 nsec = $8\frac{1}{2}$ RF units):

$$T_{sh,\ non-trig} - T_{sh,\ trig} \leq 8\frac{1}{2}RF \tag{5.4}$$

5.2.2 Timing range of Out-of-Time events

The above considerations led to the following set of cuts on the timing of Out-of-Time events. These cuts depended on the longitudinal location of the upstream and downstream showers, $PLACE_1$ and $PLACE_2$:

- Target Events:

  1. $81 \leq PLACE_1 \leq 82$, $PLACE_2 \geq 8$:

     here we required that the downstream shower triggered the apparatus, and the upstream interaction occurred after the trigger;

     $$\frac{1}{2}RF \leq T_{sh1} - T_{sh2} \leq 8\frac{1}{2}RF. \tag{5.5}$$

     In this fiducial volume region random coincidences of neutrino interactions, separated in time by up to 8 RF buckets would fall into the above timing range. Therefore the normalization factor, ${N_{RF}}^{Tar1}$ =8 had to be used in order to find number of Out-of-Time events per 1 RF bucket for that region.

  2. $10 \leq PLACE_1 \leq 80$, $PLACE_2 \geq 8$:

     in this region, both the upstream and the downstream interactions could

trigger the apparatus with full efficiency, with the earlier interaction always setting Trigger 2 on. Consequently the non-triggering interaction was always 'late' relative to the ADC gate. Therefore we required:

$$\frac{1}{2}RF \leq |T_{sh1} - T_{sh2}| \leq 8\frac{1}{2}RF, \tag{5.6}$$

For this fiducial volume region the normalization factor, ${N_{RF}}^{Tar2}$ was equal to 16, reflecting the fact that both the upstream and downstream showers could trigger the apparatus.

3. $10 \leq PLACE_1 \leq 80$, $3 \leq PLACE_2 \leq 8$:

   in this region, only the upstream interaction could set Trigger 2 on, so we required:

$$-8\frac{1}{2}RF \leq |T_{sh1} - T_{sh2}| \leq -\frac{1}{2}RF. \tag{5.7}$$

   The normalization factor for this region, ${N_{RF}}^{Tar3}$ was equal to 8.

- Toroid Events

  in this region only the upstream shower could trigger the apparatus, thus we required:

$$-8\frac{1}{2}RF \leq |T_{sh1} - T_{sh2}| \leq -\frac{1}{2}RF., \tag{5.8}$$

  The normalization factor for this region, ${N_{RF}}^{Tor}$ was equal to 8.

5.2.3 VETO Rejection of Out-of-Time events

As mentioned earlier, in order to eliminate the background events originating from interactions occurring upstream of the CCFR detector, Trigger 2 events were rejected

in hardware if a VETO bit was on at the time of the trigger coincidence. The VETO logic required a coincidence of hits from two arrays of 27 solid scintillation counters. These were mounted in two 25 feet × 15 feet arrays upstream of the detector. Additionally the two most upstream calorimeter counters were included in the VETO logic. Thus Trigger 2 was also vetoed by SBITS firing in both counters 83 and 84. The veto logic has resulted in greater than 99% efficiency in rejection of interactions upstream of the detector.

For interactions beginning at counter 81 or 82, albedo (backscattered hadrons) from the hadron shower could reach counters 83 and 84 and set the VETO bit on, causing the rejection of the Trigger 2 event. This resulted in an inefficiency of Trigger 2 for interactions in the upstream most region of the detector. In the case of two independent interactions occurring inside the detector within the duration of the ADC gate, the interaction in the upstream most part of the detector could also set a VETO bit on. However if the VETO signal arrived at the trigger logic unit after the Trigger 2 coincidence was formed by the downstream interaction, the trigger could not be rejected. Effectively, the trigger efficiency for Double Vertex events with:

$$81 \leq PLACE_1 \leq 82,$$

$$PLACE_2 \geq 8$$

depended on the relative timing between the two interactions and was biased against events with upstream interaction occurring before or at the time of the downstream interaction.

The effect of trigger rejection by VETO bits not correlated with the triggering interaction can be seen by looking at the relative timing distribution between VETO hits and Trigger 2 time, shown on Figure 5.1 . The sharp cut-off in the distribution implies that events with $T_{VETO} - T_{trig}$ smaller than 10 TDC clock counts (1 TDC clock count = 4 nsec) were vetoed. Random VETO hits occurring very early before the interaction time could not veto the trigger, since the duration of the VETO pulse was about 150 nanoseconds.

In order to remove the VETO bias in the selection of random overlay events the following cut was implemented. For Target Events in the region:

$$81 \leq PLACE_1 \leq 82,$$

$$PLACE_2 \geq 8$$

we required that there were no VETO hits such that:

$$T_{VETO} - T_{sh1} < 10\ TDC\ clock\ counts \tag{5.9}$$

Figure 5.2 shows the distribution of the relative timing between the VETO bit and the timing of the non-triggering shower in this class of Out-of-Time Double Vertex Events.

5.2.4 Visual Scanning and Classification of Out-of-Time Events

In order to verify the topology of the Out-of-Time events, the sample was visually scanned. Most of the events in the Out-of-Time sample corresponded to two uncor-

related neutrino interactions. However, a cosmic ray shower which deposited ionizing energy in the upper parts of the detector could also trigger the apparatus and mimick the Double Vertex topology (two showers isolated by a quiet gap). A section of the shower could hit the upstream end of the detector while another section the downstream end. However, the time difference between the upstream and the downstream parts of cosmic ray shower (as registered by the TDC system) was proportional to the spatial separation of the showers. Therefore cosmic ray showers contributed predominantly to the Out-of-time sample of Double Vertex events. As a result of the visual scanning, four cosmic ray shower events were rejected from the sample of Out-of-Time Double Vertex events. Additionally three events, for which the drift chamber information indicated that the downstream interaction did not originate from a neutrino interaction inside the fiducial volume of the Toroid Calorimeter were rejected from the Toroid Out-of-Time sample.

Table 5.1 summarizes the number of Out-of-Time Double Vertex events selected by the computer analysis and the number of events remaining after the visual scanning process. As the result of the selection by the computer algorithm and the visual scanning scan, 402 events remained in the Out-of-Time Double Vertex sample.

The sample of Out-of-Time events was then categorized, in a similar way as the In-Time Double Vertex Events, into the following groups:

- Target and Toroid Events, based on the longitudinal position of the downstream shower;

- the $NC \rightarrow NC$ channel and the $NC \rightarrow CC$ channel, based on the presence or absence of an outgoing muon in the downstream shower;
- Small, Intermediate and Large Separation, based on the amount of material separating the end of the upstream shower and the beginning of the downstream shower.

Similarly as in the case of the In-Time Toroid Double Vertex sample, to verify the downstream shower type assignment based on the computer algorithm, we have scanned the Toroid Out-of-Time events and assigned them to the $NC \rightarrow NC$ or the $NC \rightarrow CC$ group. The assignment was based on the presence (or absence) of a muon in the downstream shower, as registered by the drift chamber stations. The comparison of the shower type assignment based on shower length algorithm done by computer with the assignment based on visual scan has yielded following results:

1. Clear NC events

   We found 84 events which had the downstream shower assigned to the NC-type group based on shower length algorithm and no muon track emerging from the downstream shower.

2. Marginal NC events

   There were 8 events which had downstream shower identified as CC-type, based on the length of the shower, but there was no muon penetrating the Toroid downstream of it.

3. Clear CC events

   There were 127 events with CC-type classification of the downstream shower and momentum analyzable muon emerging from the downstream shower.

4. Clear CC events, but NC according to length algorithm

   We found 5 events with clear muon emerging from the downstream shower. (based on drift chamber information), for which the length algorithm classified it as NC-type.

5. Ambigious CC events

   We found 16 events, with the downstream shower classified as CC-type on basis of shower length algorithm, with muon track present, but not momentum analyzable.

As a results of the visual scanning of Toroid Out-of-Time sample, events from 'Clear NC' group and 'Marginal NC' group were included in the $NC \rightarrow NC$ channel, while events from remaining three groups fell into the $NC \rightarrow CC$ channel.

Table 5.2 and 5.3 summarize the number of events in each of the above groups.

The estimation of the random overlay background in the In-Time Double Vertex sample was done in the following way. First, Out-of-Time events, in each of the above categories separately, were normalized by the factor N_{RF}, (equal to $\frac{1}{8}$ or $\frac{1}{16}$, as discussed in the previous section) to determine the number of the Out-of-Time random coincidences per one RF bucket. Then the numbers in the $NC \rightarrow NC$ channel and $NC \rightarrow CC$ channel were added, and multiplied by three factors:

- a factor representing the expected fraction of NC-type and CC-type events in the Target, f_{NC}^{Target} and f_{CC}^{Target} and in the Toroid, f_{NC}^{Toroid} and f_{CC}^{Toroid};
- a correction corresponding to the per bucket non-uniformities in the flux of particles, R_{ob};
- a correction accounting for the inefficiency of the shower-finding algorithm for Out-of-Time events in the Target, $1/f_{sh\ eff}^{Target}$ and in the Toroid, $1/f_{sh\ eff}^{Toroid}$.

These correction factors are discussed in detail in the following three sections.

5.2.5 The Ratio $R_{NC/CC}$ for the Out-of-Time sample

Since the Out-of-Time Double Vertex events originated from random overlays of neutrino induced interactions, the ratio of the number of $NC \rightarrow NC$ events to the number of $NC \rightarrow CC$ events in the Out-of-Time Double Vertex sample should be equal within statistical errors to $R_{NC/CC}$, the ratio of NC-type to CC-type single neutrino interactions. As discussed earlier, for interactions occurring inside the Target Calorimeter, this ratio was equal to:

$$< R_{NC/CC} >^{Target} = 0.40 \pm 0.01, \tag{5.10}$$

and for interactions inside the Toroid :

$$< R_{NC/CC} >^{Toroid} = 0.60 \pm 0.02. \tag{5.11}$$

The measurement of the ratio of NC-type to CC-type interactions in the CCFR

detector, using the sample of Out-of-Time Double Vertex events gave the following results:

$$R_{NC/CC}{}_{DV}^{Target} = 0.30 \pm 0.06, \tag{5.12}$$

and for interactions inside Toroid :

$$R_{NC/CC}{}_{DV}^{Toroid} = 0.62 \pm 0.08. \tag{5.13}$$

The agreement, within statistical errors, with the average $< R_{NC/CC} >$ as measured for single neutrino interactions confirmed that the shower type assignment was not biased for events with Double Vertex topology.

In order to increase the statistical power of the random overlay background estimation, the background for each channel was calculated by summing up the contributions from overlay events with the downstream showers coming from both NC and CC interactions and then multiplying it by the factor equal to:

$$f_{NC} = \frac{< R_{NC/CC} >}{1 + < R_{NC/CC} >}, \tag{5.14}$$

for the $NC \rightarrow NC$ channel background and by the factor:

$$f_{CC} = \frac{1}{1 - < R_{NC/CC} >}, \tag{5.15}$$

for the $NC \rightarrow CC$ channel. In the calculation of the above factors, values of $< R_{NC/CC} >^{Target}$ (eqn. 5.10) and $< R_{NC/CC} >^{Toroid}$ (eqn. 5.11) were used for Target Events and Toroid Events respectively.

5.2.6 The Superbucket Correction

The number of Out-of-Time overlays (two uncorrelated neutrino interactions originating from different RF buckets) would be exactly equal to number of In-Time overlays (two uncorrelated neutrino interactions coming from same RF bucket) only in the case of an equal flux of neutrino particles in individual RF buckets. However, a bucket-to-bucket variation in the flux of particles would lead to higher number of In-Time accidentals relative to the number of Out-of-Time accidentals. This effect follows from the fact that In-Time overlays are proportional to the average of the square of the beam intensity $< I^2 >$, while Out-of-Time overlays are proportional to the square of the average beam intensity $< I >^2$.

Let us denote the fractional standard deviation of the beam intensity, equal to standard deviation of the intensity distribution per RF bucket divided by the mean of the intensity distribution as F_I:

$$F_I = \frac{\sigma_I}{< I >}. \tag{5.16}$$

From the set of equations listed below:

$$\sigma_I^2 =< I^2 > - < I >^2 \tag{5.17}$$

$$In - Time\ accidentals \sim < I^2 > \tag{5.18}$$

$$Out - of - Time\ accidentals \sim < I >^2 \tag{5.19}$$

it follows that the ratio of In-Time overlays to the Out-of-Time overlays, later

referred to as the superbucket ratio R_{sb} [1], is equal to:

$$R_{sb} = \frac{In - Time\ overlays}{Out - of - Time\ overlays} = 1 + F_I^2. \tag{5.20}$$

The source of the per bucket flux non-uniformity can be summarized as follows: the number of protons in RF buckets originating from a single booster batch is fairly uniform. However, as protons are accelerated in the Main Ring and later in the Tevatron the longitudinal and transverse size of the buckets and their momentum dispersion may vary for individual buckets. The extraction of primary protons from the Tevatron ring to the Neutrino Beam Line is done by forcing the particles into a resonance trajectory and then separating them from the Tevatron orbit using an electrostatic septum. The amplitude of this resonance depends strongly on the momentum of the protons. Through the resonance, the orbit of a particle becomes unstable, and the amplitude of the oscillation depends on the momentum of the particle. The particles with higher momentum cross the electrostatic septum earlier, and thus leave the ring first.

The estimation of the superbucket correction has been discussed in detail in Appendix C. Here we quote only the result of this measurement:

$$R_{sb} = 1.5 \pm 0.25 \tag{5.21}$$

This value of R_{sb} corresponds to an r.m.s. spread of intensities per RF buckets of

[1] The origin of this name comes from the fact that at Fermilab, per-bucket flux non-uniformity was often referred to as a 'superbucket effect', underscoring the existence of RF buckets with extremely high number of particles relative to the number of particles in typical RF bucket.

- pions constituted the dominant component of the beam, with the proton fraction of about 20% at 100 GeV. Electron contamination was about 10% at 50 GeV and increased with decreasing energy, and a kaon fraction was about 5% or less. However, most of the beam electron interactions took place in the material upstream of the Target Calorimeter and did not trigger the apparatus.

During the Test-Beam running period, the detector was triggered by the coincidence of a beam signal and a signal of energy deposition in the CCFR Target Calorimeter, equivalent to the Trigger 2 for neutrino running.

5.3.2 Test-Beam Double Vertex Selection

The search for the upstream shower started at the most upstream counter exposed to the beam $N_{max}(Cart)$: counter 28 for the 2-Cart configuration, counter 42 for the 3-Cart configuration and counter 56 for the 4-Cart configuration. We have also required that the hadronic interaction took place within the 5 upstream most counters (3 λ_{INT}) from the upstream end of the target carts. Since the horizontal positions of the calorimeter carts were offset relative to the Toroid Spectrometer, the search for the downstream shower was restricted only to the volume of the Target carts. Therefore the longitudinal fiducial volume cuts in the Test-Beam data analysis were as follows:

$$PLACE_1 \leq N_{max}(Cart) \tag{5.27}$$

$$PLACE_1 \geq N_{max}(Cart) - 5 \tag{5.28}$$

$$PLACE_2 \geq 3 \tag{5.29}$$

With the exception of the longitudinal fiducial volume cuts, the selection criteria of the Test-Beam Double Vertex sample were identical to the selection performed on the neutrino-induced data sample, described in Sections 4.2.2 and 4.2.3.

5.3.3 Test-Beam Double Vertex Analysis

Figure 5.3 illustrates the distribution of the relative timing between the upstream and the downstream shower for the Test-Beam Double Vertex sample. Since the random overlay background was negligible, for virtually all the events the absolute value of the time difference between the upstream shower (originating from a primary hadron interaction) and the downstream shower, (originating from the interaction of the neutral hadrons produced in the upstream shower) was less than $\frac{1}{2}$ RF. For neutral hadron punch-through events, both the intrinsic spread within the RF buckets and the timing correction for the dependence on the transverse position of the shower were the same. This resulted in very good timing resolution for Test-Beam Double vertex events, with an r.m.s σ of the difference in time between the two showers of 2.4 nsecs.

Figure 5.4 shows the angular distribution of Test-Beam punch-through events. Here the angle was defined as:

$$\theta_{T.B.} = \arctan\left(\sqrt{\left(\frac{\Delta V_X}{\Delta V_Z} - <\theta_X>\right)^2 + \left(\frac{\Delta V_Y}{\Delta V_Z}\right)^2}\right), \tag{5.30}$$

where $< \theta_X >$ was equal to the average angle between the beam direction and the direction of the detector axis:

$$< \theta_X >= 65\ mrad. \tag{5.31}$$

Figure 5.5 presents the energy spectrum of the downstream shower. Events with E_{sh2} greater than 9.0 GeV are shown. One should notice the exponential fall-off the energy of the secondary showers.

Figure 5.6 shows the distribution of separation between the end of the primary hadronic shower and the beginning of the secondary, downstream shower.

The events were categorized on the basis of the L_{steel} :

- the Small separation events, with $6 \leq L_{steel} \leq 10$.

  The Test-Beam Double Vertex sample included 65 such events.

- the Intermediate separation events, with $11 \leq L_{steel} \leq 20$.

  The Test-Beam Double Vertex sample included 6 such events.

No events with material separation between two showers, L_{steel} greater than 20 counters were found. It is important to realize that only the 3-Cart and 4-Cart configurations were sensitive to the neutral hadron punch-through events with Large separation.

All Test-Beam Double Vertex events were classified as the $NC \rightarrow NC$ events. The probability of a muon production in hadron interactions with the incident energy less than 100 GeV is less than 10^{-3}. Thus in a sample of less than 100 Double Vertex events

one would expect not to find a secondary hadronic shower with a muon emerging from it. However since the shower type assignment was based on the parametrization of the length of hadronic shower such that it would include 98% of all NC showers for given range of shower energy, one could expect to find few events in the Test-Beam Double Vertex sample that would be classified as $NC \rightarrow CC$, although a high energy muon would not be present.

5.3.4 The Normalization of the Test-Beam and the neutrino-induced Double Vertex Samples

We have estimated the neutral hadron punch-through background in the In-Time sample of Double Vertex neutrino induced interactions by multiplying the raw number of Double Vertex events found in the Test-Beam data by several normalization factors. The following normalization factors were considered:

- the ratio of the total number of single NC neutrino interactions to the total number of hadronic interactions in the Test-Beam data;
- a correction accounting for different geometrical acceptance of the detector during neutrino running relative to Test-Beam running;
- a correction accounting for the different transverse distribution the neutrino and hadron Test-Beam;
- a correction accounting for the different angular distribution of the neutrino induced and hadron induced neutral punch-through events

- a correction accounting for the different hadron energy distribution of the Test-Beam and neutrino data.

Below we describe in the detail the calculation of these factors. The total number of single vertex neutrino interactions N_ν, was calculated using following cuts:

$$PLACE \leq 82 \tag{5.32}$$

$$PLACE \geq 10 \tag{5.33}$$

$$SHEND \geq 19 \tag{5.34}$$

$$E_{sh} \geq 30.GeV \tag{5.35}$$

$$|V_X|, |V_Y| \leq 50" \tag{5.36}$$

$$R_{sh} = \sqrt{V_X^2 + V_Y^2} \leq 60". \tag{5.37}$$

The requirement SHEND $\geq$ 19 ensured full geometrical acceptance for the Target Double Vertex events with separation L_{steel}:

$$10 < L_{steel} \leq 15 \tag{5.38}$$

In the combined data sample of E744 and E770, we have found the total number of neutrino induced interactions N_ν:

$$N_\nu = 1.61 \times 10^6 \ events. \tag{5.39}$$

The number of single neutrino NC interactions was defined as:

$$N_{NC} = N_\nu \times \frac{< R_{NC/CC} >}{1 + < R_{NC/CC} >}, \tag{5.40}$$

where $< R_{NC/CC} >$ was equal to the measured ratio of the NC to the CC neutrino- and induced interactions in the CCFR detector (eqn. 5.10). Thus, the total number of single vertex neutrino interactions classified as NC-type, that could produce neutral hadron punch-through events with separation:

$$11 \leq L_{steel} \leq 15 \tag{5.41}$$

was equal to:

$$N_{NC}^{Int} = .460 \times 10^6 \ events. \tag{5.42}$$

The absolute normalization correction of 1.12 was applied for Double Vertex events with separation $6 \leq L_{steel} \leq 10$:

$$N_{NC}^{Small} = .515 \times 10^6 \ events. \tag{5.43}$$

This correction corresponded to 12% larger number of neutrino NC interactions that could produce neutral hadron punch-through events with separation:

$$6 \leq L_{steel} \leq 10 \tag{5.44}$$

The number of single hadronic interactions for each of the three different Test-Beam cart configurations $N_{T.B.}$ was calculated using following cuts:

$$PLACE \leq N_{max}(Cart) \tag{5.45}$$

$$PLACE \geq N_{max}(Cart) - 5 \tag{5.46}$$

$$E_{sh} \geq 30.GeV \tag{5.47}$$

$$|V_X|, |V_Y| \leq 50" \tag{5.48}$$

$$r_{sh} = \sqrt{V_X^2 + V_Y^2} \leq 60". \tag{5.49}$$

The number of hadronic interactions passing the above cuts in combined data sample of 2-Cart, 3-Cart and 4-Cart configuration was equal to:

$$N_{T.B.} = .352 \times 10^6 \; events. \tag{5.50}$$

Therefore, the absolute normalization factor between the neutrino-induced and Test-Beam induced data was equal to:

$$\frac{N_{NC}}{N_{T.B.}}^{Int} = 1.31 \tag{5.51}$$

for the Intermediate separation region and

$$\frac{N_{NC}}{N_{T.B.}}^{Small} = 1.47 \tag{5.52}$$

for the Small separation region.

We now compare the geometrical acceptances of the neutrino and the Test-Beam detector setup. Figure 5.7 illustrates the geometrical acceptance for the Double Vertex events of the neutrino running detector setup , as a function of L_{steel}. This acceptance function was determined using the sample of the Target Out-of-Time Double Vertex Events. (the combined sample of the $NC \rightarrow NC$ and $NC \rightarrow CC$ channel, without angle cut) and normalized to the acceptance for the events with the separation between the upstream and the downstream shower, $10 < L_{steel} \leq 15$. The lower relative acceptance for events with L_{steel} shorter than 10 counters, has resulted from the inefficiency of the quiet gap cut for small separation events. As can be seen from the figure, high acceptance of the neutrino setup extended beyond L_{steel} equal to 20 counters.

The detector setup during the Test-Beam data taking employed a smaller number of Calorimeter carts than the typical setup of the CCFR Detector during neutrino running period. This resulted in a smaller relative acceptance for the Test-Beam Double Vertex events with long separation between the primary and secondary showers. The acceptance was only lower for the 2-Cart configuration, since only 28 counters were exposed to the hadronic beam. Thus, a geometrical acceptance correction for Test-Beam Double Vertex events had to be taken into account. This correction was calculated using a Monte Carlo simulation in the following way:

- first, the longitudinal position (PLACE) of the hadronic interaction was generated according to the fraction of the Test-Beam data taken with different cart configurations;
- then, the end of the primary hadronic interaction shower (SHEND) was generated based on the distribution of the hadronic showers in the Test-Beam data;
- finally, the separation between SHEND and counter #3 (the downstream most counter within the fiducial volume of the Test-Beam setup) was calculated:

$$L_{test} = SHEND - 3 - 1. \tag{5.53}$$

L_{test} was then compared with the separation L_{steel}, generated according to the neutrino setup relative acceptance function, (Figure 5.7). In the above Monte Carlo calculations we have assumed the full acceptance for the small separation events, since the inefficiency of the quiet gap cut was also present in the selection

of the Test-Beam Double Vertex sample.

- The event was accepted if:

$$L_{test} \leq L_{steel} \tag{5.54}$$

Figure 5.8 illustrates the Test-Beam relative geometrical acceptance, $Rel\ Acc^{T.B./\nu}$, as a function of L_{steel}, normalized to the neutrino setup acceptance for separation:

$$10 < L_{steel} \leq 15. \tag{5.55}$$

The step-like fall-off of this acceptance function reflects different cart configurations during the Test-Beam data taking period.

Each of the Test-Beam Double Vertex events was then multiplied by the weight equal to inverse of the relative acceptance function for given separation between the showers L_{steel}. The average relative longitudinal correction factor for the Test-Beam Double Vertex events in Intermediate Separation was equal to 1.09 . The relative longitudinal acceptance correction for the Small Separation Test-Beam Double Vertex events was equal to 1.0 .

The transverse dimensions of the neutrino beam were comparable with the transverse size of the detector resulting in a wide radial distribution of the neutrino interactions. However, the transverse size of the hadron beam was only few inches and most of the Test-Beam data was taken with the hadron beam steered into the geometrical center of the upstream most target cart. This resulted in the higher transverse acceptance for neutral hadron punch-through events in the Test-Beam relative to the

neutrino induced neutral hadron punch-through events.

Another factor affecting the relative normalization between neutral punch-through events induced by neutrino interactions and by hadron interactions was the angular distribution of the punch-through events. In case of hadron interactions, the angle θ of the neutral hadron punch-through was calculated relative to the hadronic interaction shower direction, which was identical with the direction of the hadron beam. However in the case of the NC neutrino interactions, the hadronic shower was coming at the angle, such as to balance the transverse momentum, p_T of the scattered neutrino. Since the above angle could not be reconstructed on the event by event basis, the angle θ of the neutral punch-through events from neutrino induced showers was calculated relative to the detector beam axis.

The average angle of the hadronic shower in the neutrino NC interactions is:

$$< \theta >_{had} = 60\ mrad \tag{5.56}$$

The angle of the hadronic shower is inversely proportional to its energy:

$$\theta_{had} \propto \frac{\theta_\nu \times E_\nu}{E_{had}}. \tag{5.57}$$

On other hand, due to the energy threshold of the neutral hadron punch-through showers:

$$E_{sh2} > 15\ GeV \tag{5.58}$$

the rate of neutral hadron punch-through events depended on the total energy of the primary hadronic shower. Low energy hadronic showers were less likely to produce a

neutral hadron shower with E_{sh2} above 15 GeV. In effect, in ν-N interactions, there was an inverse correlation between the angle of hadronic shower θ_{had} and the rate of neutral hadron punch-through events.

We have used a Monte Carlo simulation to calculate the correction accounting for the lower transverse acceptance and for the wider angular distribution of the neutrino induced neutral hadron punch-through events. The simulation consisted of the following steps:

- generate the transverse position of the primary hadronic interaction, V_{x1}, V_{y1} according to the neutrino interactions transverse position distributions;
- generate the longitudinal separation between the primary and secondary showers Δ_z:

$$\Delta_z = z(PLACE_1) - z(PLACE_2), \tag{5.59}$$

  according to the Δ_z distributions of the Test Beam Double Vertex events in Small and Intermediate regions separately;
- generate the angle of the neutral punch-through particles, $\theta_{T.B.}$ according to the angular distribution of the Test Beam Double Vertex events in Small and Intermediate regions separately;
- use angular distribution of hadronic showers in neutrino interactions, θ_{had} to smear $\theta_{T.B.}$;

- using V_{x1}, V_{y1}, Δ_z and the smeared neutral hadron punch-through angle, $\theta_{T.B.}^{smear}$, calculate transverse positions of secondary showers ,V_{x2}, V_{y2} and require that they are within fiducial volume of the detector. The fraction of Double Vertex events passing the above cut was:

$$Acc_{tr}^{\nu/T.B.} = 0.94. \tag{5.60}$$

- finally we required that $\theta_{T.B.}^{smear}$ is less than 125 milliradians. The fraction of Double Vertex events passing the above cut was equal to:

$$Acc_{\theta}^{\nu/T.B.Small} = 0.81 \tag{5.61}$$

  for events in the Small separation and:

$$Acc_{\theta}^{\nu/T.B.Int} = 0.94 \tag{5.62}$$

  for events in the Intermediate separation.

In summary, the punch-through background in the Target Double Vertex sample was estimated using following expression:

$$Bkgd_{p.-through}^{NC,Target} = \frac{< R_{NC/CC} >}{1 + < R_{NC/CC} >} \times \frac{N_\nu}{N_{T.B.}} \times Acc_{tr}^{\nu/T.B.} \times Acc_{\theta}^{\nu/T.B.} \times \{ \sum_{i=L_{steel}} N_i^{T.B.,raw} \times \frac{}{Rei} \tag{5.63}$$

In the above equation $N_i^{T.B.,raw}$ corresponds to the raw number of neutral hadron punch-through events found in the Test-Beam data with the separation equal to:

$$L_{steel} = i \text{ counters}. \tag{5.64}$$

and $Rel\ Acc_i^{T.B./\nu}$ is equal to the Test-Beam longitudinal acceptance relative to the neutrino setup for a given separation L_{steel}.

Table 5.6 summarizes the neutral hadron punch-through background estimation for the Small Separation and the Intermediate Separation Target Double Vertex events.

5.3.5 Systematic uncertainties in the estimation of the neutral hadron punch-through background in ν-N interactions

The above estimation of the of neutral hadron punch-through background in ν-N interactions was based on the analysis of neutral hadron punch-through from hadron induced showers . There are two possible sources of systematic uncertainties in the estimation of this background:

- different energy spectra of neutrino-induced and hadron induced interactions
- different fragmentation functions for neutral hadron production in neutrino and hadron induced interactions

Below we discuss the possible systematic errors associated with these differences.

The hadron energy distribution of neutrino interactions is shown on Figure 5.9a. The average value of the total energy was equal to :

$$< E_{tot}^{\nu} >= 98\ GeV \tag{5.65}$$

The total energy spectrum of the Test-Beam data is shown on Figure 5.9b. Distinctive peaks correspond to the different energy settings of the hadron beam. The average

value of the total energy was equal to :

$$< E_{tot}^{T.B.} >= 83\ GeV \tag{5.66}$$

The approximate agreement between the average energy of neutrino data and the average energy in the Test-Beam interactions was purely accidental. A Monte Carlo calculation was done in order to check if the different hadron energy spectra of the neutrino data vs the Test-Beam data introduce a systematic difference in the number of secondary showers. We found that systematic effects associated with different energy spectra of primary interactions were smaller than 5%.

It is important to realize that the estimation of the punch-through background in the neutrino induced Double Vertex events was based on the implicit assumption that the fractional energy carried by the neutral hadrons produced in neutrino induced showers is same as the fractional energy of the neutral hadrons produced in the pion induced showers. This assumption is valid if most of the neutral punch-through events originate from the neutral hadrons produced in the secondary hadronic interactions of the primary fragments (so called 'shower component').

However neutral hadrons may be also produced at the primary vertex interaction (so called 'vertex component'). We have studied the possible systematic difference in the punch-through rates in neutrino and pion induced interactions arising from different fragmentation functions, $f(z)$

$$f(z) = \frac{1}{N}\frac{dN}{dz}, \tag{5.67}$$

where fragmentation variable z is defined as:

$$z = \frac{Fragment\ Energy}{Total\ Hadronic\ Energy} \tag{5.68}$$

We have used fragmentation functions for neutral kaon production in neutrino and pion induced interactions [27, 28] and applied the nuclear reweighting correction accounting for nuclear effects in hadronic fragmentation [24]. The comparison of the resulting fragmentation functions for neutral kaon production in ν-Fe and π-Fe interactions is shown on Figure 5.10. A Monte Carlo simulation of the secondary shower energy spectrum of neutral kaons based on the above fragmentation functions indicated that the production rate of neutral kaons from the primary collisions in pion induced interactions with punch-through shower energies above 15 GeV would be about 30% higher than in neutrino induced interactions. However since more than 2/3 of neutral hadron punch-through events originate from secondary interactions we estimate the difference between pion induced and neutrino induced showers to be less than 10%.

5.4 The Total Background Estimation

The total background estimation was calculated by adding the Random Overlay background and the Punch-Through background for each category of the Double Vertex events separately.

The summary of the background for neutrino induced Double Vertex sample is presented in the Table 5.7.

Chapter 6

Results and Comparisons with Theoretical Predictions

6.1 Overview

In this section, we use the data described in the previous chapter to set limits on the possibility of production and subsequent decay of Neutral Heavy Leptons in ν-N interactions . We explain the method used to determine the statistical significance of the results. Finally, we compare the experimental results with Monte Carlo simulation of the production and decay of NHL.

6.2 Calculation of the statistical significance of the limit

We define an excess of observed Double Vertex events. N_{excess} as:

$$N_{excess} = N_{obs} - N_{bkgd} \tag{6.1}$$

In order to estimate the statistical significance of an excess of observed events above the background, we have to take into account two uncertainties:

1. the uncertainty in the mean number of background events, described by σ_{bkgd}; depending on the statistics and the systematic uncertainties of the background

estimation. the distribution of mean number of background events may follow Poisson or Gaussian statistics or some combination thereof.

2. the fluctuations, according to Poisson statistics, of the actual number of background events.

The total error is calculated by combining, in quadrature, the uncertainty of the mean with the statistical error of the actual number of background events, given by the square root of the number of background events:

$$\sigma_{excess} = \sqrt{N_{bkgd} + \sigma^2_{bkgd}} \tag{6.2}$$

We express the significance of the excess in terms of the ratio:

$$\frac{N_{excess}}{\sigma_{excess}}. \tag{6.3}$$

If the number of the observed events is consistent with the background estimation, we set limits on the possibility of the existence of the signal. The limits are expressed in terms of the confidence level as a function of the assumed signal μ_S. Assuming that the relative uncertainty in the background estimation is negligible, the confidence level $CL(\mu_S)$ is defined as:

$$CL(\mu_S) = \sum_{n=N_{obs}+1}^{\infty} P(\mu_B + \mu_S; n), \tag{6.4}$$

where:

$$P(\mu_B + \mu_S; n) \tag{6.5}$$

is the Poisson probability of observing n events, given the number of background events μ_B, and the number of signal events μ_S. For a mean number of background events, μ_B and the observed number of events N_{obs}, $CL(\mu_S)$ is the probability of seeing more than N_{obs} events, if the mean number of events from the signal is μ_S.

We set limits on the signal μ_S at the 90% confidence level by defining $\mu_S{}^{min}$ and $\mu_S{}^{max}$:

$$CL(\mu_S{}^{max}) = .90 \tag{6.6}$$

$$CL(\mu_S{}^{min}) = .10 \tag{6.7}$$

Therefore the signal, μ_S, is bounded, at the 90% confidence level:

$$\mu_S{}^{min} < \mu_S < \mu_S{}^{max} \tag{6.8}$$

$CL(\mu_S = 0)$ corresponds to the probability, that given no signal, fluctuations in the background would give more than N_{obs} observed events. For values of $\mu_S < \mu_S^{min}$ there is a greater than 90% probability that the number of observed events would be N_{obs} or less; for $\mu_S > \mu_S^{max}$ there is a greater than 90% probability that we would observe more than N_{obs} events.

The definition of the confidence level (Eqn 6.4) is modified in case when the number of the background events is not known exactly. Assuming the probability distribution function of the background rate, $\mu_B{}'$:

$$f(\mu_B, \sigma_B; \mu_B{}'), \tag{6.9}$$

given the average background rate of μ_B, with systematic error σ_B, the confidence level $CL(\mu_S)$ is expressed as:

$$CL(\mu_S) = \sum_{n=N_{obs}+1}^{\infty} \int_0^{\infty} d\mu_B' f(\mu_B, \sigma_B; \mu_B') P(\mu_B' + \mu_S; n), \qquad (6.10)$$

6.3 Limits on observed number of NHL events

In setting the limits on the production and the decay of NHL we consider the following four channels:

1. $NC \rightarrow NC$, Large Separation Target Double Vertex events:

   the number of observed events (number of the In-Time events), N_{obs} is 10. and the estimated background, N_{bkgd} is 4.8 $\pm$ 0.8. The dominant source of the background for this channel are random overlay events and the uncertainty in the background estimation is dominated by the 17% fractional error in the estimation of the superbucket correction R_{sb}. The total error on the excess of the observed events above the estimated background. σ_{excess} is equal to 2.33 events. Thus in the above channel, the excess of 5.2 events represents a '2.2 σ effect'. In other words, if one would perform large number of measurements of a process with μ_B = 4.8 $\pm$ 0.8, on average in about 1.5% of the experiments one would observe more than 10 events. Using values of N_{obs} =10, μ_B= 4.8 and σ_B= 0.8 we obtain:

$$CL(\mu_S = 0) = 1.5\% \qquad (6.11)$$

$$\mu_S^{min} = 2.2 \ events \qquad (6.12)$$

$$\mu_S^{max} = 10.8 \ events \qquad (6.13)$$

Since the significance of the number of the excess events (NHL candidates) is only 1.5 %, we use μ_S^{max} = 10.8 events to set the upper limit on the number of NHL observed in this channel.

2. $NC \rightarrow NC$, intermediate separation Target Double Vertex events

   In this channel. the number of observed events, N_{obs} is 12, and the total estimated background. N_{Bkgd} is equal to 8.2 $\pm$ 3.1 events. The background is dominated by neutral hadron punch-through events. The uncertainty in the background estimation is coming from the Poisson statistics of the 6 neutral punch-through events observed in the hadron Test-Beam sample, and the uncertainty in the relative normalization between hadron Test-Beam Double Vertex sample and the neutrino induced Double Vertex sample.

   Using values of N_{obs} =12, μ_B= 8.2 and σ_B= 3.1 we obtain:

$$CL(\mu_S = 0) = 23.\% \qquad (6.14)$$

$$\mu_S^{min} = 0 \ events \qquad (6.15)$$

$$\mu_S^{max} = 9.8 \ events \qquad (6.16)$$

Since the number of observed events is consistent with the estimated background we use this result to set limits on the number of NHL observed in this channel.

3. $NC \rightarrow NC$, small separation Target Double Vertex events

In this channel, the number of observed events, N_{obs} is 90, and the estimated total background. N_{bkgd} is 83. $\pm$ 9.6. In this channel, the background comes almost exclusively from the neutral hadron punch-through events. Using values of N_{obs} =90, μ_B= 83. and σ_B= 9.6 we obtain:

$$\mu_S{}^{min} = 0 \ events \tag{6.17}$$

$$\mu_S{}^{max} = 30 \ events \tag{6.18}$$

Since the number of observed events is consistent with the estimated background we use this result to set limits on the number of NHL observed in this channel.

4. $NC \rightarrow CC$, combined Target and Toroid Double Vertex events

We use this channel to set the limit on number of observed Neutral Heavy Leptons with at least one muon emerging from the decay vertex. In the $NC \rightarrow CC$ channel, the background events originate predominantly from random overlays of neutrino interactions. The contribution from the neutral hadron punch-through background is negligible. Therefore in setting the limits on number of observed NHL events in this channel, we have combined the Target $NC \rightarrow CC$ sample from Small, Intermediate and Large separation classes.

The toroid hole introduces the systematic uncertainty in the amount of the material separating the upstream and the downstream showers. This leads to uncertainty in the background estimation for the Toroid Double Vertex events

in the Small and Intermediate separation regions. Therefore in addition to the Target Double Vertex $NC \rightarrow CC$ events only the Toroid Double Vertex events with Large separation between two showers were included in the $NC \rightarrow CC$ data sample.

Thus, for this combined data set the the number of observed events, N_{obs} is 27, and the total estimated background, N_{bkgd} is equal to 40.9 $\pm$ 7.0 events. Using values of N_{obs} =27, μ_B= 40.9 and σ_B= 7.0 we obtain:

$$\mu_S{}^{min} = 0. \ events \tag{6.19}$$

$$\mu_S{}^{max} = 9.6 \ events \tag{6.20}$$

Since the number of observed is consistent with the estimated background we use this result to set limits on the number of NHL observed in this channel.

In summary, the above results show a 2.2 σ excess of the number of the observed events above the expected background in the $NC \rightarrow NC$ channel, where the separation between the end of the upstream and the beginning of the downstream showers in larger than 2.3 meters of steel. However the number of observed events is consisten with the expected background in the $NC \rightarrow NC$ channel with the separation between the end of the upstream and the beginning of the downstream showers between 0.6 meters and 2.3 meters of steel. There is also no excess of observed events in the $NC \rightarrow CC$ channel for events with the separation between end of the upstream and the beginning of the downstream showers in larger than 0.6 meters of steel.

6.4 Comparisons with Theoretical Predictions

We use the results summarized in the previous section to set limits on Neutral Heavy Lepton production and decay in our apparatus. To that end we compare the upper limit of the number of observed NHL events with the predictions of NHL Monte Carlo generation program.

The parameters of the Monte Carlo generation program are the mass of Neutral Heavy Lepton m_{NHL} and the coupling suppression constant U^2 relative to the Fermi coupling G_F. The Monte Carlo generation of the production of NHL and its subsequent decay in the CCFR apparatus is described in the detail in the Appendix D.

The absolute normalization of the number of Monte Carlo generated NHL is based on the number of observed NC interactions in the entire neutrino data sample. Figures 6.1 through 6.3 show the number of Monte Carlo generated NHL events that would be observed in the CCFR apparatus, in the $NC \rightarrow NC$ channel in the Small, Intermediate and Large Separation classes. The number of predicted NHL events is plotted as a function of a suppression coupling constant U^2, relative to the Fermi coupling G_F for different values of parameter m_{NHL}. The horizontal lines correspond to the upper limits, at 90% confidence level, of the number of NHLs observed in this experiment in a given channel.

Figure 6.4 shows the number of Monte Carlo generated NHL events that would be observed in the CCFR apparatus, in the $NC \rightarrow CC$ channel. In setting limits

on m_{NHL} and U^2 using the $NC \rightarrow CC$ channel, to maximize the sensitivity to NHL production and decay in our apparatus, both data and Monte Carlo events were required to have a separation between the primary and the secondary showers less than L_{max}. L_{max} was chosen for each m_{NHL} and U^2 to contain 95% of all NHL decays within the fiducial volume of the CCFR detector. Figure 6.5 shows the limits, at 90% confidence level, for NHL production in the m_{NHL}, U^2 plane.

6.5 Conclusions

We have searched for the Double Vertex signature of Neutral Heavy Leptons produced in the neutrino-nucleon interactions. No evidence of a NHL was found in the charged current decay channel, $NHL \rightarrow \mu^- + X$. NHL, with masses between 0.5 GeV/c^2 and 3.0 GeV/c^2 were excluded for coupling to muons below 1 to 10^{-4} of the Fermi strength, depending on the value of NHL mass. In the neutral current decay channel, for separation between the end of the primary shower and the beginning of the secondary shower greater than 2.3 meters, we have found an excess of 5.2 ± 2.33 events above the estimated background from conventional physics processes. This excess represents an upper limit of 10 events at a 90% confidence level , a 2.2 standard deviation effect. However, no evidence of NHL was found in the neutral current decay channel, for separation between the end of the primary shower and the beginning of the secondary shower between 0.6 meters to 2.3 meters. Using the above data we set limits on production of Neutral Heavy Leptons decaying through neutral current

channel. $NHL \rightarrow \nu + X$. NHL with masses between 0.5 GeV/c^2 and 2.0 GeV/c^2 were excluded, at 90% confidence level, for coupling to muonic neutrinos below 1 to 5×10^{-4} of Fermi strength, depending on the NHL mass.

Appendix A

The CCFR Collaboration

P. de Barbaro. A. Bodek, H.S. Budd. W.K. Sakumoto

University of Rochester, Rochester, NY 14627

K.T. Bachmann,[1] R.E. Blair.[2] C. Foudas.[3] B.J. King, W.C. Lefmann, W.C. Leung, S.R. Mishra. P.Z. Quintas. S.A. Rabinowitz. F.J. Sciulli. W. Seligman, M.H. Shaevitz

Columbia University, New York, NY 10027

F.S. Merritt. M.J. Oreglia. H. Schellman.[4] B.A. Schumm[5]

University of Chicago, Chicago, IL 60637

R.H. Bernstein. F. Borcherding. M.J. Lamm. W. Marsh. D.D.Yovanovitch

Fermilab, Batavia, IL 60510

P. Sandler. W.H. Smith

University of Wisconsin, Madison, WI, 53706

[1]Present address: Widener Univ.. Chester. PA 19013.

[2]Present address: Argonne National Laboratory, Argonne. IL. 60439.

[3]Present address: Univ. of Wisconsin. Madison. WI. 53706.

[4]Present address: Fermilab. Batavia. IL 60510

[5]Present address: LBL. Berkeley. CA 94720.

Appendix B

Parametrization of the hadronic shower length

In this section we describe the procedure used to determine the parametrization of the length of hadronic showers as a function of hadronic shower energy. The parametrization was used in a determination of hadronic interaction type of the upstream and downstream showers in the Double Vertex event sample: if the actual shower length was longer than the length predicted by the parametrization, the shower was deemed to be CC-type, and if shorter, it was retained in the NC-type sample.

In order to determine the shape of the hadronic shower length distribution we have analyzed the hadron test beam data recorded during the experiment E744 [1]. During that running period the hadron beams with energies at 25 GeV, 50 GeV, 100 GeV, 200 GeV and 300 GeV were directed into the CCFR Target Calorimeter carts. Pions constituted the dominant component of the hadron beam. The electron beam contamination was removed by requiring that the ratio R_3 [21], between the energy deposited in the first three most upstream counters and total energy contained within the shower boundries:

$$R_3 = \frac{E(1) + E(2) + E(3)}{E_{TOT}} \tag{B.1}$$

[1] This analysis was performed by R. Bernstein, member of the CCFR Collaboration

be less than 0.96. Electrons have a ratio close to 1.0 and hadron interactions populate the region between 0. and 1.0 .

The length of a shower was defined as:

$$L_{sh} = PLACE - SBEND + 1, \tag{B.2}$$

where PLACE corresponded to the number of the upstream most counter of the group of at least two counters with energy deposition greater than the equivalent of 4 × minimum ionizing particle depositions, and SBEND was determined by searching for three consecutive counters with no TDC hits. The discriminator threshold for the TDC signals corresponded to about 0.25 × minimum ionizing particle deposition.

Figure B.1 shows L_{sh} distribution for different energy settings of hadron Test-Beam. These distributions were used to determine 98% length containment L_{had}, that is the length past which only 2% of hadron showers penetrate.

$$\frac{\int_0^{L_{had}} \frac{dN}{dL}}{\int_0^{\infty} \frac{dN}{dL}} = 98\%. \tag{B.3}$$

Figure B.2 shows the 98% length containment, L_{had}, as a function of a hadron energy. The solid line corresponds to the L_{had} parametrization used in the vertex type assignment (NC-type or CC-type) in the Double Vertex analysis.

The length of the hadronic shower, in units of Target counters (material between each Target counter was equivalent to ≈ 11.6 cm of Fe) was parametrized as a function

of hadronic energy of the shower:

$$L_{had}(E) = P_1 + P_2 \times log_{10}(E)\ for E \geq 50\ GeV$$
$$L_{had}(E) = R_1 + R_2 \times E\ for E < 50\ GeV, \tag{B.4}$$

where values of above parameters were:

$$P_1 = -5.84$$

$$P_2 = 5.61$$

$$R_1 = 12.0$$

$$R_2 = 0.08$$

For the purpose of a comparison we show alternative parametrization of the hadronic shower length based on 99% energy containment criterion, that is the event length past which only 1% of the energy leaks out. However this length definition can not be directly applied for shower type assignment due to fluctuations in energy depositions of outgoing muon in charged current neutrino interactions. The dashed line on Figure B.2 corresponds to the shower length parametrization based on 99% energy containment.

Appendix C

Calculation of the superbucket correction

As discussed earlier, a bucket-to-bucket variation in the flux of neutrino particles in individual RF buckets would lead to a higher number of In-Time accidentals relative to the number of Out-of-Time accidentals:

$$R_{sb} = \frac{In - Time\ overlays}{Out - of - Time\ overlays} = 1 + F_I^2, \tag{C.1}$$

where F_I denotes the fractional standard deviation of the beam intensity.

We have analyzed events with accidental overlays of charged current neutrino interactions to measure the ratio R_{sb}. In this analysis the CC events were required to have momentum analyzable track traversing the Muon Spectrometer. The timing of each neutrino interaction was determined using drift chamber track fitting algorithm.

The following cuts were used in the selection of the $CC \rightarrow CC$ overlays:

- Only Trigger 1 (Charged Current Muon Trigger) events were included in the analysis.
- We have selected events with two charged current neutrino interactions by requiring two muon tracks in the Muon Spectrometer.

- The longitudinal position of both interactions, had to be contained between counter 76 and counter 10.
- The transverse vertex positions of both the upstream and the downstream charged current neutrino interactions were required to be within 60 inches of the center of the Target Calorimeter and inside ± 50 inches central square.
- Both muon tracks had to link with at least two toroid segments in both x and y views, and be momentum analyzable.
- The timing of each interaction was determined using the information from the drift chamber stations located in the toroid gaps.
- We required that for each track the timing extracted independently from x and y view chambers agreed:

$$T^x_{\mu i} - T^y_{\mu i} \leq \frac{1}{2} RF, i = 1, 2. \tag{C.2}$$

- We required that two uncorrelated CC neutrino interactions recorded during same event were separated by no more than 20 RF buckets.
- The distance of closest approach between the two tracks in the Target Calorimeter was required to be greater than 8 inches. The object of this cut was to reject dimuon events originating from single neutrino interactions.

It is important to realize that the above method of calculation of the superbucket correction implicitly assumes that all $CC \rightarrow CC$ events originate from random overlays

of two uncorrelated charged current neutrino interactions.

Figure C.1 shows the relative timing distribution between the two charged current neutrino interactions. The events in the central bucket correspond to random overlays of two uncorrelated neutrino interactions occurring in same RF bucket, while the events in non-zero buckets correspond to accidental overlays of charged current neutrino interactions from different RF buckets. Figure C.2 shows the number of accidental overlays per one RF bucket. The events from the positive and the negative buckets were averaged together. We found 26 In-Time $CC \rightarrow CC$ overlay events, with the relative timing difference between two muons:

$$|T_{\mu 1} - T_{\mu 2}| \leq \frac{1}{2} RF \tag{C.3}$$

and an average of 15.5 events per 1 RF bucket of $CC \rightarrow CC$ overlays originating from different RF buckets.

Similar analysis was performed for a case of overlay events, where event was triggered by a muon originating from the interaction upstream of the CCFR detector (Trigger 6) and a non-triggering interaction corresponded to the charged current neutrino event. In this channel we have found total of 13 In-Time overlay events, with the relative timing difference between two muons:

$$|T_{\mu 1} - T_{\mu 2}| \leq \frac{1}{2} RF \tag{C.4}$$

and and average of 11.6 events per 1 RF bucket of overlays originating from different RF buckets.

Table C.1 summarizes number of overlays found in each of above channels in E744 and E770 experiments. Since the beam non-uniformity may have been different for each of the running periods, we have calculated the weighted average of superbucket correction R_{sb} for both experiments using following formula:

$$R_{sb} = \{\frac{N_{In-Time}}{N_{Out-of-Time}}\}_{E744} \times f_{rel}(E744) + \{\frac{N_{In-Time}}{N_{Out-of-Time}}\}_{E770} \times f_{rel}(E770), \quad (C.5)$$

where $f_{rel}(E744)$ and $f_{rel}(E770)$ corresponded to the relative flux of neutrino interactions recorded in each of the experiments:

$$f_{rel}(E744) = 0.43 \quad (C.6)$$

$$f_{rel}(E770) = 0.57 \quad (C.7)$$

Therefore, the weighted average of superbucket correction in both experiments was equal to:

$$R_{sb} = 1.5 \pm .25 \quad (C.8)$$

This value of R_{sb} corresponds to an average r.m.s spread of intensities per RF bucket of $\sqrt{0.5}$ or about 70%.

Appendix D

NHL Monte Carlo generation procedure

The Monte Carlo generation of the production of NHL and its subsequent decay in the CCFR apparatus consisted of the following steps:

- neutrino events spectrum

  We generate the neutrino and antineutrino events according to the energy and position spectrum of the Tevatron neutrino beam, as measured by single vertex charged current neutrino interactions in the CCFR detector. We apply hadronic energy and fiducial volume cuts same as in the Double Vertex data analysis.

- production cross-section of NHL in ν-N interactions

  The production cross-section of NHL in ν-N interactions, σ_{NHL} was assumed to be proportional to the cross-section of the neutrino charged current interactions. σ_{CC}:

$$\sigma_{NHL} = \sigma_{CC} * U^2 * (1 - m^2_{NHL}/s)^2, \quad (D.1)$$

  where U^2 is the coupling suppression factor, relative to G_F, due to the mixing between the incoming muonic neutrino and the NHL, and the expression in the bracket represents a mass dependent threshold factor.

- Kinematic variables of NHL

the kinematic variables of NHL in the lab frame were calculated by substituting the mass of a muon from the CC interaction by a mass of assumed NHL:

$$E_{NHL} = E_\mu \tag{D.2}$$

$$\nu = E_\nu - E_{NHL} \tag{D.3}$$

$$p_{NHL} = \sqrt{(E_\mu^2 - m_{NHL}^2)} \tag{D.4}$$

$$\cos(\theta_{NHL}) = \frac{(2 * E_\nu * (E_{NHL} - m_p * x * y) - m_{NHL}^2}{2 * E_\nu * p_{NHL}}, \tag{D.5}$$

where x is equal to the Bjorken scaling variable:

$$x = \frac{Q^2}{2 * m_p * \nu} \tag{D.6}$$

and y is equal to the fraction of the energy lost by neutrino in the lab frame:

$$y = \frac{\nu}{E_\nu} \tag{D.7}$$

- Life-time of NHL

We assume that the life-time of NHL τ_{NHL}, is inversely proportional to the coupling suppression factor. U^2 and has following mass dependence [13]:

$$\tau_{NHL} \simeq (4.49 \times 10^{-12} s)(m_{NHL}/1\ GeV)^{5.19} U^{-2} \tag{D.8}$$

The decay rate to any given process scales with m_{NHL}^5, and the additional exponential term reflects the rate at which new decay channels open up as m_{NHL} increases.

- Decay modes of NHL

The decay of NHL can proceed via the NC mode (emission of Z^0 and light neutrino) or the CC mode (emission of $W^\pm$ and charged lepton), depending on the relative coupling of NHL to Z^0 and $W^\pm$. The relative branching ratios also depend on the mass of assumed NHL. In the case of the neutral current decay mode, the virtual Z^0 can materialize by coupling to pair of leptons ($\nu\bar{\nu}$, e^-e^-, $\mu^+\mu^-$, or $\tau^+\tau^-$) or quark-antiquark pair ($q\bar{q}$). In the charged current decay mode, the virtual $W^\pm$ can materialize by coupling to lepton pairs (charged lepton and accompanying neutrino) or pairs of quarks. NHL which decay to at least one muon in the final state were assigned to the $NC \rightarrow CC$ channel, and NHL with muonless decays were assigned to the $NC \rightarrow NC$ channel. The separation between the hadronic shower from the neutrino interaction and the downstream shower originating from the decay of the NHL was generated according to the decay length of the NHL in the lab frame. Monte Carlo generated events were categorized into three separation classes: small, intermediate and large, using same separation definition as in the Double Vertex analysis. NHLs decaying within fiducial volume of the Target Calorimeter were classified as the Target Double Vertex events, and NHLs decaying within the fiducial volume of the Toroid Spectrometer were classified as the Toroid Double Vertex events.

- normalization of the Monte Carlo to the data

The absolute number of NHL predicted by Monte Carlo simulation for combined

data set of the experiments E744 and E770 was derived by comparing the total number of observed single vertex neutrino induced interactions in the CCFR detector, $N_{\nu-N}{}^{data}$, with the number the of Monte Carlo generated neutrino induced interactions, $N_{\nu-N}{}^{MC}$:

$$f_{data/MC} = N_{\nu-N}{}^{data}/N_{\nu-N}{}^{MC}. \tag{D.9}$$

The total number of the Monte Carlo generated neutrino interactions was equal to the number of the MC generated charged current interactions, passing hadronic energy and fiducial volume cuts, N_{CC}^{MC} multiplied by the factor $(1+r_\nu)$ for neutrino induced interactions or $(1+r_{\bar{\nu}})$ for antineutrino induced interactions, where r_ν, $(r_{\bar{\nu}})$ represents the ratio of the neutral current (NC) to the charged current (CC) cross-sections for neutrino (antineutrino) induced interactions.

$$r_\nu = \frac{\sigma_{\nu-N}^{NC}}{\sigma_{\nu-N}^{CC}} \tag{D.10}$$

$$r_{\bar{\nu}} = \frac{\sigma_{\bar{\nu}-N}^{NC}}{\sigma_{\bar{\nu}-N}^{CC}} \tag{D.11}$$

We have used following values for r_ν and $(r_{\bar{\nu}})$, as measured by the CDHS Collaboration [29] :

$$r_\nu = .3072 \pm 0.0032 \tag{D.12}$$

$$r_{\bar{\nu}} = .363 \pm 0.015 \tag{D.13}$$

References

[1] L. M. Brown, Physics Today, September 1978, p. 23.

[2] E. Fermi, Z. Physik 88: 1661 (1934).

[3] T. D. Lee and C. N. Yang, Phys Rev 98: 1501 (1955).

[4] T. D. Lee and C. N. Yang, Phys Rev 104: 254 (1956).

[5] C. Y. Prescott et al., Phys. Lett. 77*B*: 347 (1978).

[6] M. Fritshi et al., Phys. Lett. 173*B*: 485 (1986).

[7] R. Abela et al., Phys. Lett. 146*B*: 431 (1984).

[8] H. Albrecht et al., Phys. Lett. 202*B*: 149 (1988).

[9] S. Weinberg, Phys. Rev. Lett. 19: 1264 (1967).

[10] R. Mohapatra, G. Senjanovic. Phys. Rev. *D*23: 165 (1981). Review aritic-le in: Quarks. Leptons and Beyond. NATO ASI Series, Series B: PHysics, *vol*122: 219 (1988).

[11] M. Gell-Mann. P. Ramond and R. Slansky, in: Supergravity. North Holland 1979.

[12] C. N. Leung, J. L. Rosner. Phys. Rev. *D*28: 2205 (1983).

[13] M. Gronau, C. N. Leung, J. L. Rosner, Phys. Rev. *D29*: 2539 (1984).

[14] F. J. Gilman, Comments Nucl. Part. Phys. 16: 231 (1986).

[15] D. Decamp et al., CERN priprint: CERN-EP/89-139.

[16] M. Z. Akrawy et al., CERN priprint: CERN-EP/90-72.

[17] S. R. Mishra et al., *in* : Neutrino 88, Proc. 13th Int. Conf. Neutrino Physics and Astrophysics. Boston, 1988, p. 259.

[18] J. Dorenbosch et al., Phys. Lett. *166B*: 473 (1986).

[19] S. R. Mishra et al., Phys. Rev. Lett. 59: 1397 (1987).

[20] R. Bernstein, Fermilab. Private Communication.

[21] F. S. Merritt et al., Nuclear Inst. and Methods *A215*: 27 (1986).

[22] B. Barish et al., IEEE Trans. Nucl. Sci., *NS – 25*: 532 (1978).

[23] C. Foudas, Ph. D. Thesis, Columbia University, 1989, unpublished.

[24] B. A. Schumm, Ph. D. Thesis, The University of Chicago, 1988, unpublished.

[25] S. R. Mishra, Columbia University, Private Communication.

[26] W. Sakumoto et al., Nuclear Inst. and Methods *A294*: 179 (1990).

[27] P. Bosetti et al., Nucl. Phys. *B209*: 29 (1982).

[28] A. E. Brenner et al., Phys. Rev. *D26*: 1497 (1982).

[29] U. Amaldi et al., Phys Rev *D36*: 1385 (1987).

[30] R. Abela et al., Phys. Lett. *105B*: 263 (1981).

[31] T. Yamazaki et al., in : Neutrinò 84. Proc. 11th Int. Conf. Neutrino Physics and Astrophysics. 1984. p. 183.

[32] A. M. Cooper-Sarkar et al., Phys. Lett. *160B*: 207 (1985).

[33] M. E. Duffy et al., Phys Rev *D38*: 2032 (1988).

[34] We have used limits from Ref. 13].

Scanning of the In-Time Double Vertex Events			
	Fiducial Volume Region		
	Target	Toroid	Combined
Comp. selected events	123	69	192
DC hits in quiet gap	2	13	15
Scraping the edge		7	7
Remained after vis. scan	121	49	170

Table 4.1: Summary of the visual scanning of the In-Time Double Vertex Events.

In-Time Target Double Vertex Events			
	separation between Showers		
	Small	Interm.	Large
$NC \rightarrow NC$	90	12	10
$NC \rightarrow CC$	2	0	7
Combined	92	12	17

Table 4.2: Number of In-Time Target Double Vertex Events.

In-Time Toroid Double Vertex Events			
	separation between Showers		
	Small	Interm.	Large
$NC \rightarrow NC$	11	3	13
$NC \rightarrow CC$	1	2	19
Combined	12	5	32

Table 4.3: Number of In-Time Toroid Double Vertex Events.

Scanning of the Out-of-Time Double Vertex Events			
	Fiducial Volume Region		
	Target	Toroid	Combined
Comp. selected events	194	248	442
cosmic ray events	3	1	4
Scraping the edge	0	3	3
Remained after vis. scan	191	244	435

Table 5.1: Summary of the visual scanning of the Out-of-Time Double Vertex Events.

Out-of-Time Target Double Vertex Events			
	separation between Showers		
	Small	Interm.	Large
$NC \rightarrow NC$	2	6	36
$NC \rightarrow CC$	7	18	122
Combined	9	24	158

Table 5.2: Number of Out-of-Time Target Double Vertex Events.

Out-of-Time Toroid Double Vertex Events			
	separation between Showers		
	Small	Interm.	Large
$NC \rightarrow NC$	3	6	84
$NC \rightarrow CC$	3	4	144
Combined	6	10	228

Table 5.3: Number of Out-of-Time Toroid Double Vertex Events.

Summary of Signal and Background of Double Vertex Events			
	separation between Showers		
Target, $NC \rightarrow NC$	Small	Interm.	Large
In-Time events	90	12	10
Random Overlay Bkgd.	0.24 ± 0.09	0.62 ± 0.17	4.8 ± 0.8
Punch-Through Bkgd.	82.8 ± 9.6	7.6 ± 3.1	0
Total Background	$83. \pm 9.6$	8.2 ± 3.1	4.8 ± 0.8

	separation between Showers		
Target, $NC \rightarrow CC$	Small	Interm.	Large
In-Time events	2	0	7
Random Overlay Bkgd.	0.61 ± 0.23	1.61 ± 0.41	12.0 ± 2.3
Punch-Through Bkgd.	1	0	0
Total Background	1.61 ± 0.23	1.61 ± 0.41	12.0 ± 2.3

	separation between Showers
Toroid, $NC \rightarrow NC$	Large
In-Time events	13
Random Overlay Bkgd.	16.0 ± 2.9
Punch-Through Bkgd..	.0
Total Background	16.0 ± 2.9

	separation between Showers
Toroid, $NC \rightarrow CC$	Large
In-Time events	19
Random Overlay Bkgd.	26.7 ± 4.9
Punch-Through Bkgd..	.0
Total Background	26.7 ± 4.9

Table 5.7: Summary of Signal and Background events in Double Vertex search.

Number of In-Time $CC \rightarrow CC$ random overlays			
	Running period		
	E744	E770	Combined
$TR1 \rightarrow TR1$	15	11	26
$TR6 \rightarrow TR1$	3	10	13
Combined	18	21	39

Table C.1a: Summary of the number of In-Time $CC \rightarrow CC$ random overlay events.

Number of Out-of-Time $CC \rightarrow CC$ random overlays			
	Running period		
	E744	E770	Combined
$TR1 \rightarrow TR1$	7.2	8.3	15.5
$TR6 \rightarrow TR1$	2.0	9.6	11.6
Combined	9.2	17.9	27.1

Table C.1b: Summary of the number of Out-of-Time $CC \rightarrow CC$ random overlay events. normalized to 1 RF bucket.

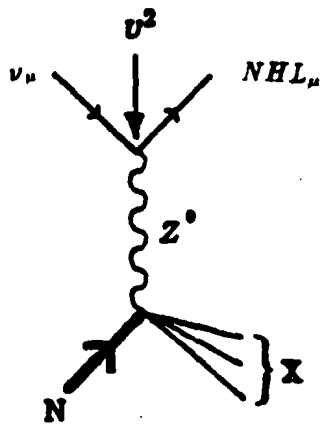

Figure 1.1: The Feynman diagram for the production of isosinglet Neutral Heavy Lepton in $\nu - N$ interactions.

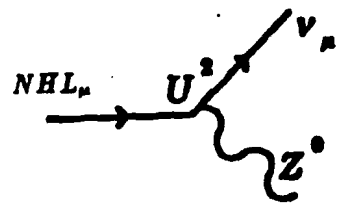

Figure 1.2a: The Feynman diagram for the decay of NHL via the coupling to Z^0.

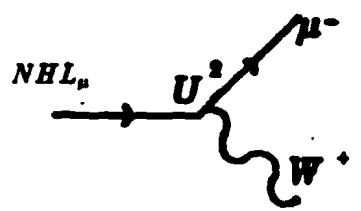

Figure 1.2b: The Feynman diagram for the decay of NHL via the coupling to $W^\pm$.

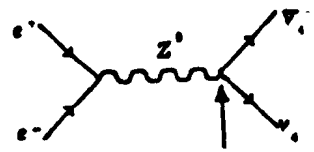

no suppression

Figure 1.3a: The Feynman diagram for the production of a pair of fourth generation NHLs.

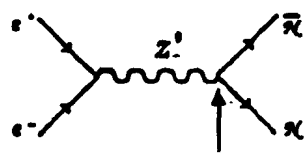

suppression U^4

Figure 1.3b: The Feynman diagram for the production of a pair of isosinglet NHLs. suppression U^2

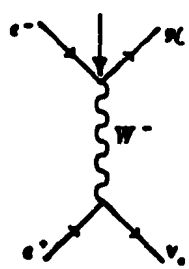

Figure 1.3c: The Feynman diagram for the production of isosinglet NHL in association with a light neutrino from known three generations.

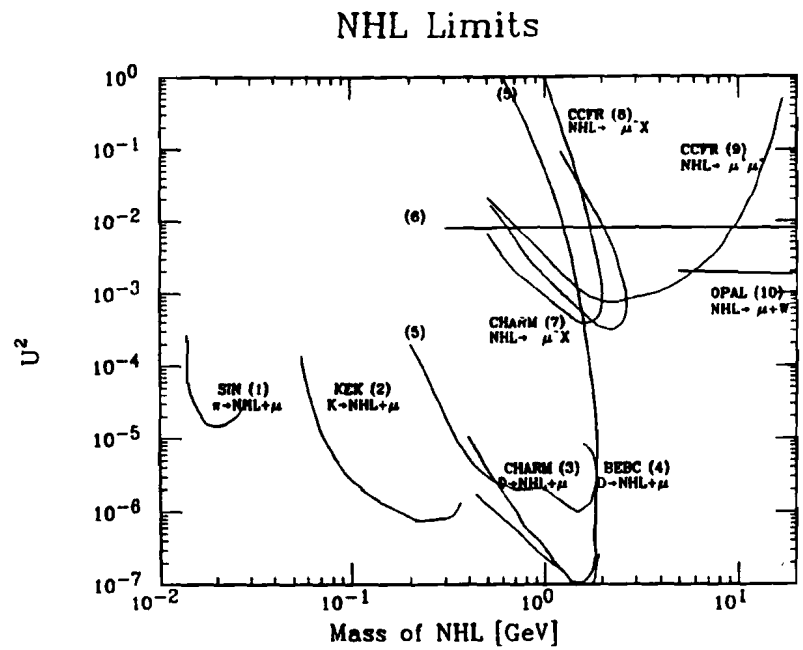

Figure 1.4: Existing limits on the coupling suppression factor U_μ^2 as a function of mass of isosinglet Neutral Heavy Lepton NHL_μ, as obtained from various experiments: (1) SIN $\pi \to \mu\nu$ [30]; (2) KEK $K \to \mu\nu$ [31]; (3) CHARM beam dump experiment [18]; (4) BEBC beam dump experiment [32]; (5) FNAL beam dump experiment [33]; (6) universality constraints [34]; (7) CHARM double vertex Search [18]; (8) CCFR double vertex Search [19]; (9) CCFR dimuon search [17]; (10) OPAL limit on NHL production from Z^0 decay [16].

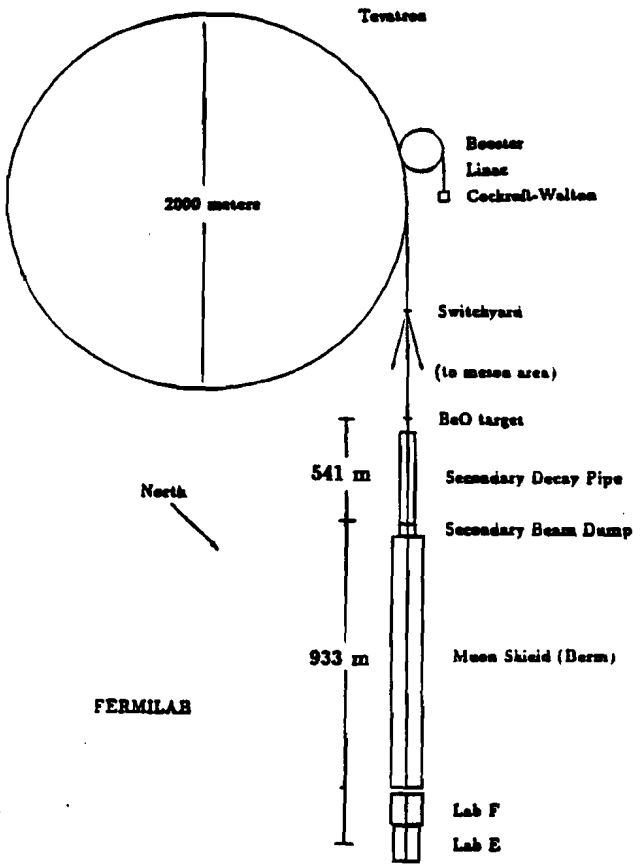

Figure 2.1: The FNAL Tevatron accelerator and the neutrino beam line.

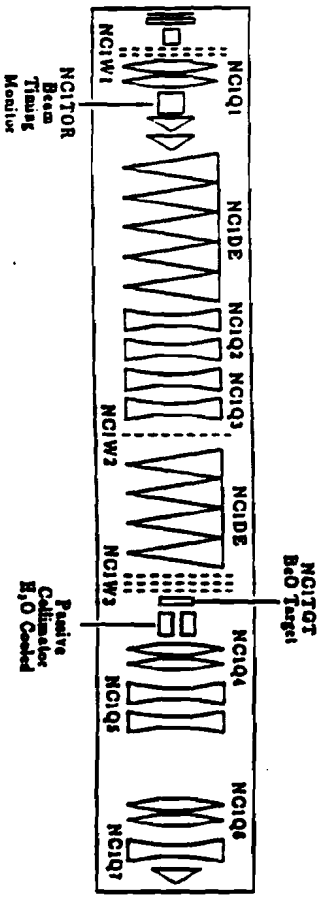

Figure 2.2: The Quadrupole Triplet Neutrino Beam line.

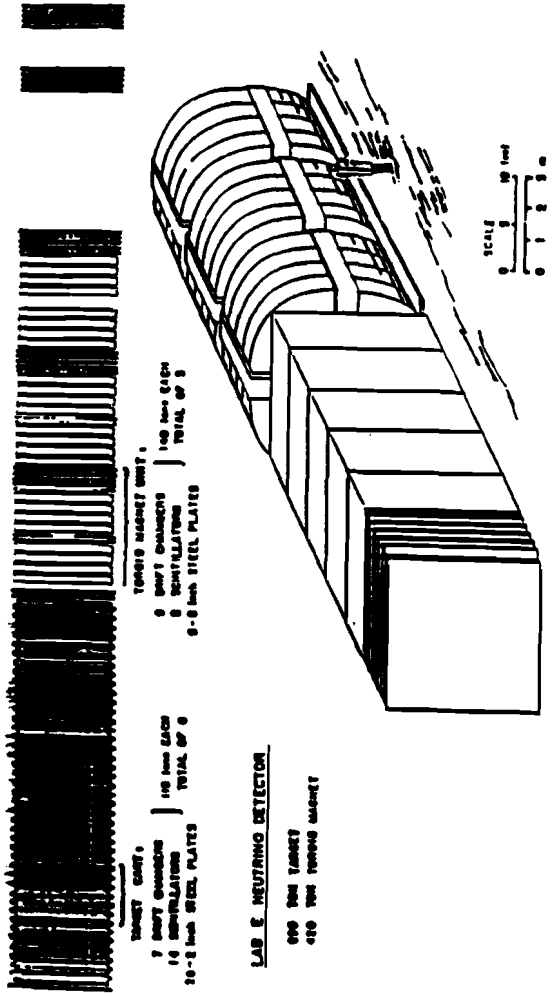

Figure 2.3: The CCFR neutrino detector.

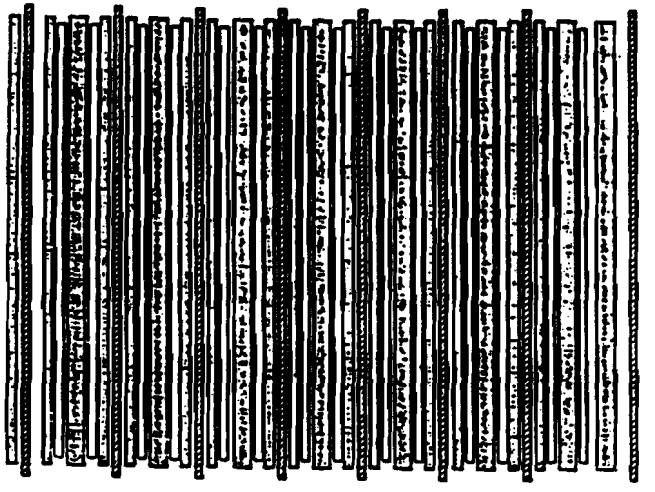

Figure 2.4: Structure of a typical calorimeter cart. The shaded rectangles represent steel plates; the white rectangles represent scintillation counters, and the rectangles with diagonal lines represent drift chambers.

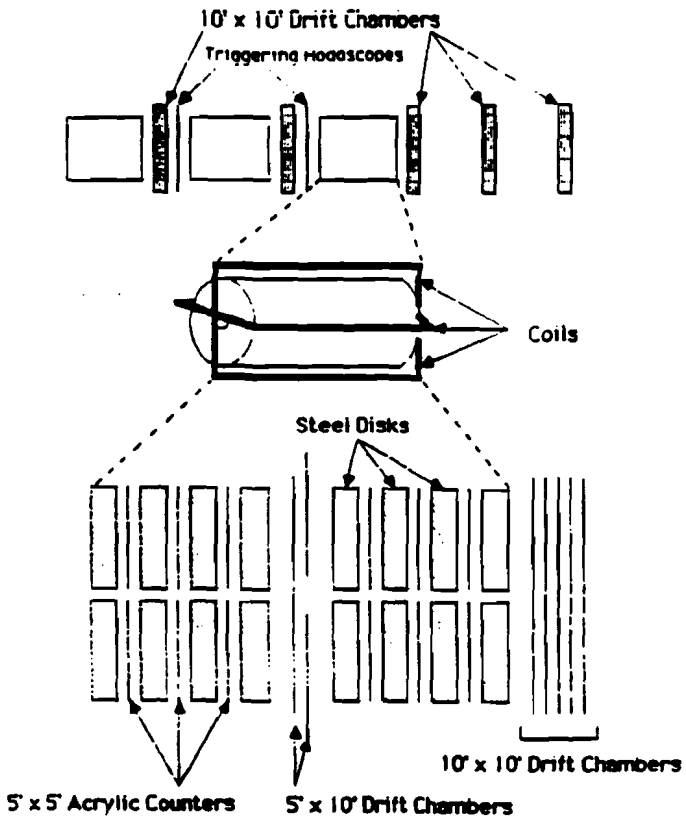

Figure 2.5: The Muon Spectrometer (the Toroid).

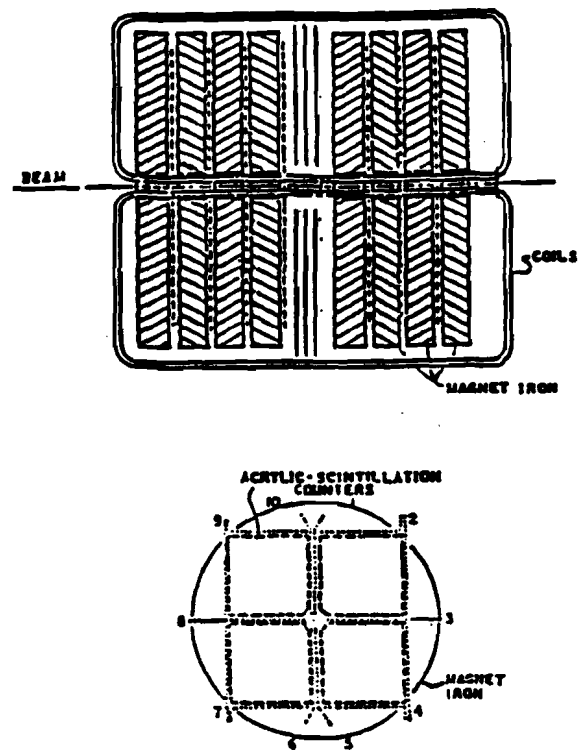

Figure 2.6: Diagram of a toroid cart. Each cart is made of eight iron washers with the magnet coil going through the hole. Acrylic scintillation counters are placed between the washers and five 1-wire drift chambers are mounted in each toroid gap.

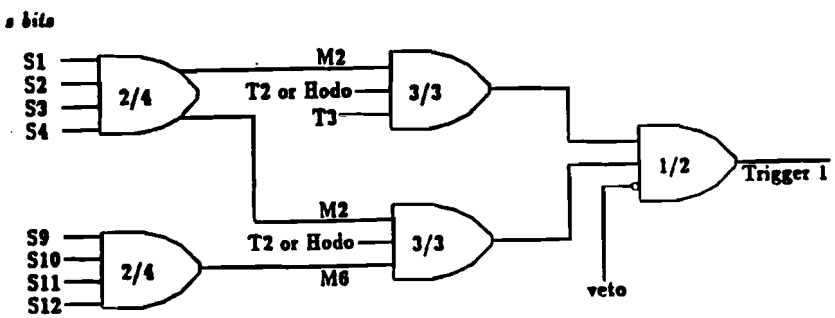

Figure 2.7: The diagram of Trigger 1 logic.

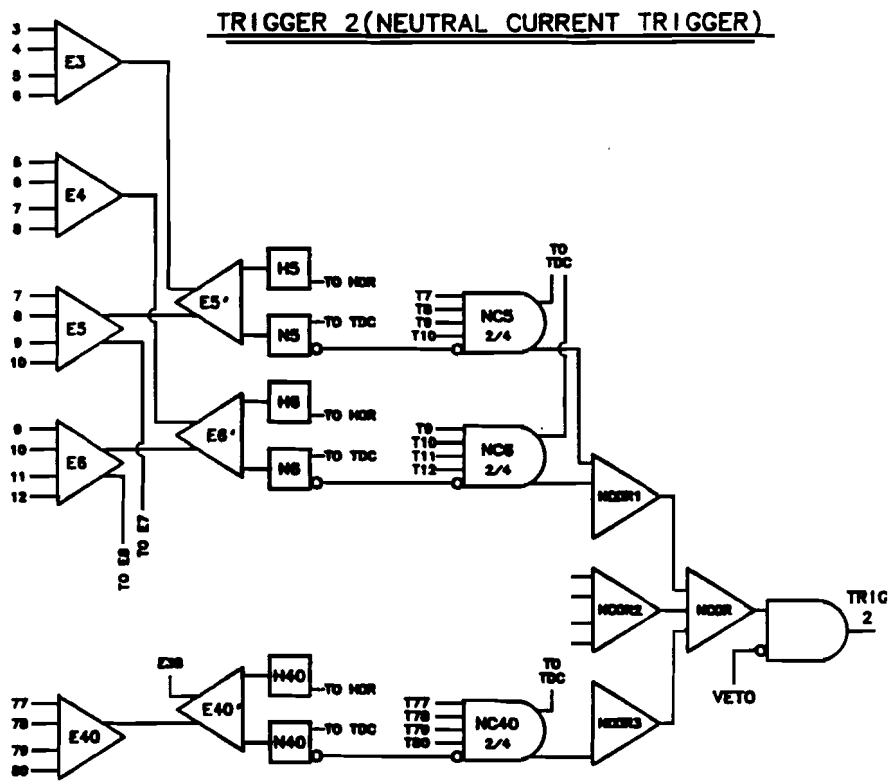

Figure 2.8: The diagram of Trigger 2 logic.

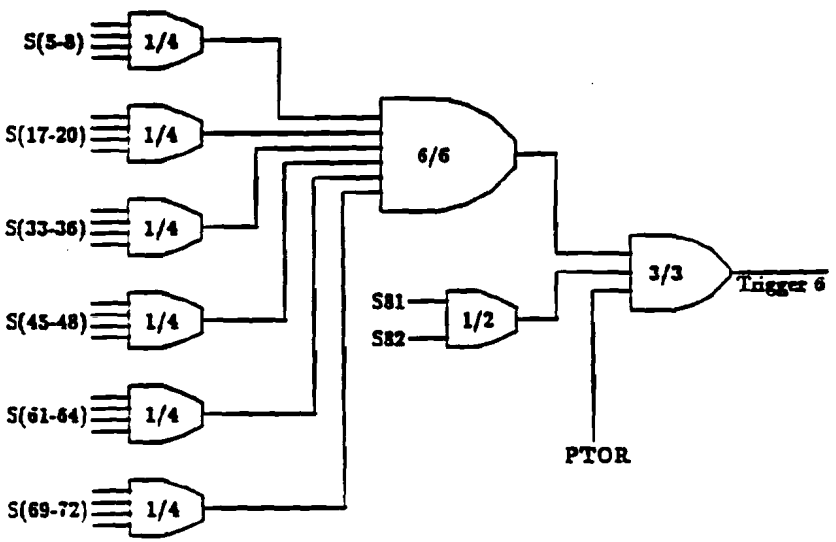

Figure 2.9: The diagram of Trigger 6 logic.

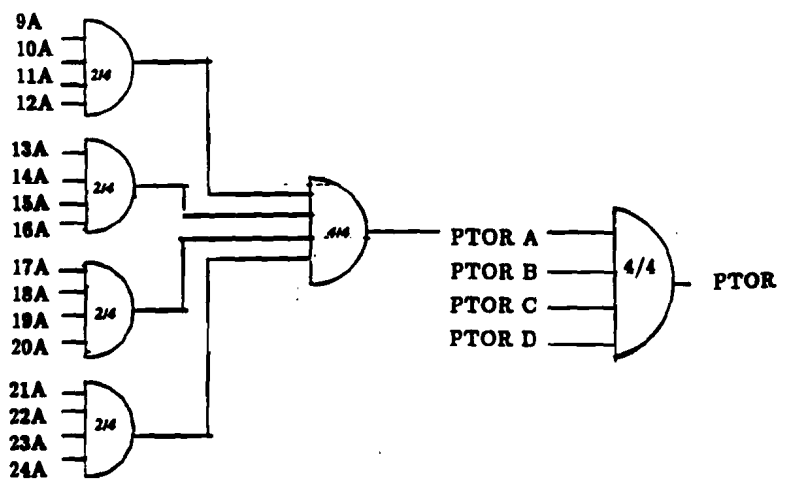

Figure 2.10: The diagram of *PTOR* logic.

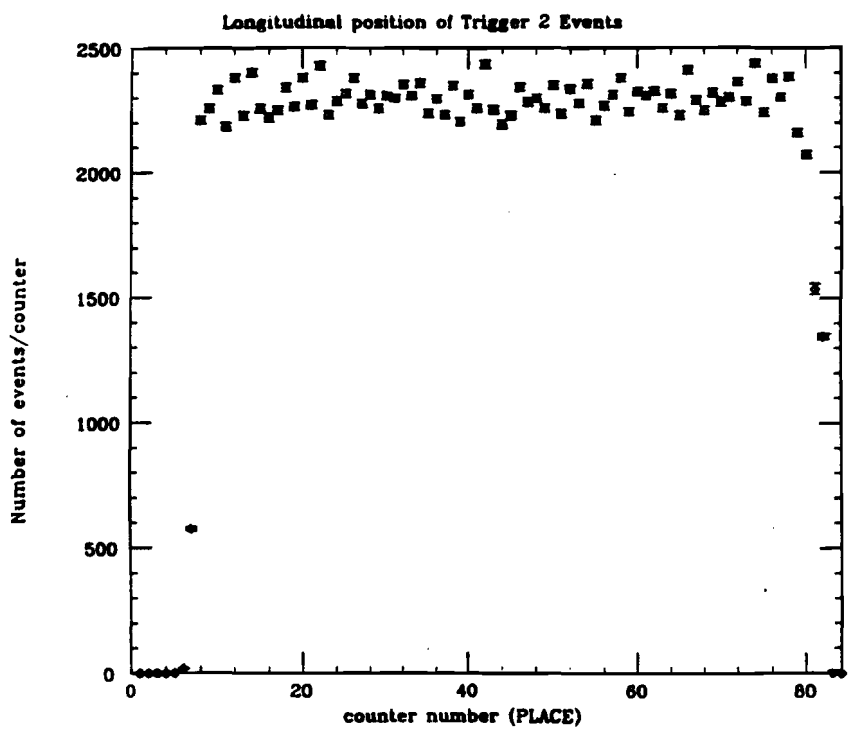

Figure 2.11: The distribution of the longitudinal position of the interactions recorded with Trigger 2. Trigger 2 was fully efficient for neutrino induced interactions occurring between counters 8 and 80.

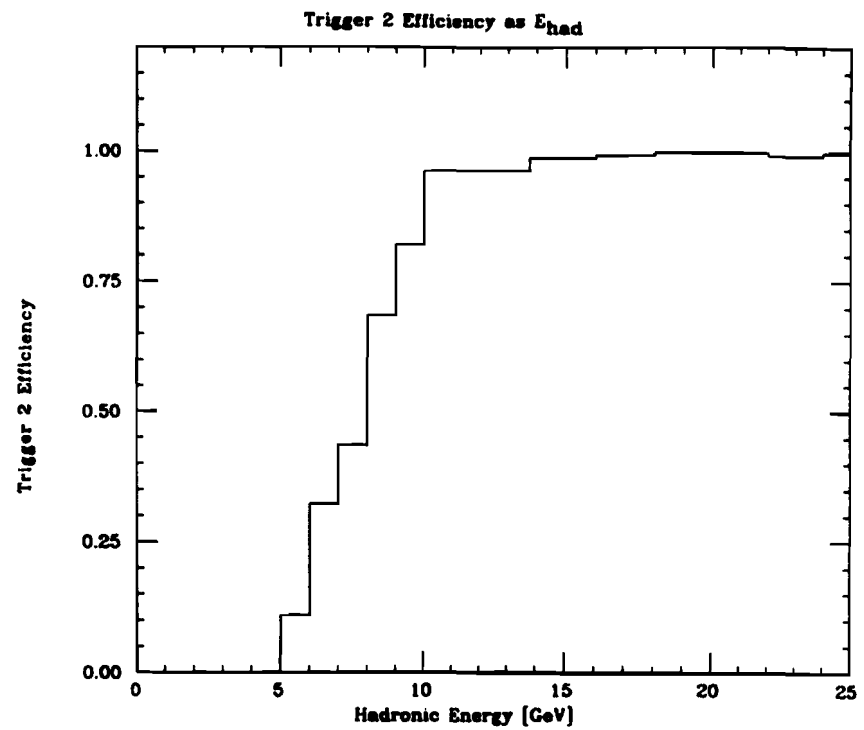

Figure 2.12: Efficiency of Trigger 2 as a function of the hadronic energy of neutrino-induced interaction. The trigger was fully efficient for interactions with E_{had} greater than 15 GeV.

Figure 3.1a: The diagram of the relative timing between the ADC gate and the phototube pulses associated with the triggering interaction.

Figure 3.1b: The diagram of the relative timing between the ADC gate and the phototube pulses associated with the interaction occurring *after* the interaction that triggered the apparatus. The tail of the signal is not integrated.

Figure 3.1c: The diagram of the relative timing between the ADC gate and the phototube pulses associated with the interaction occurring *before* the interaction that triggered the apparatus. The raising edge of the pulse is not integrated.

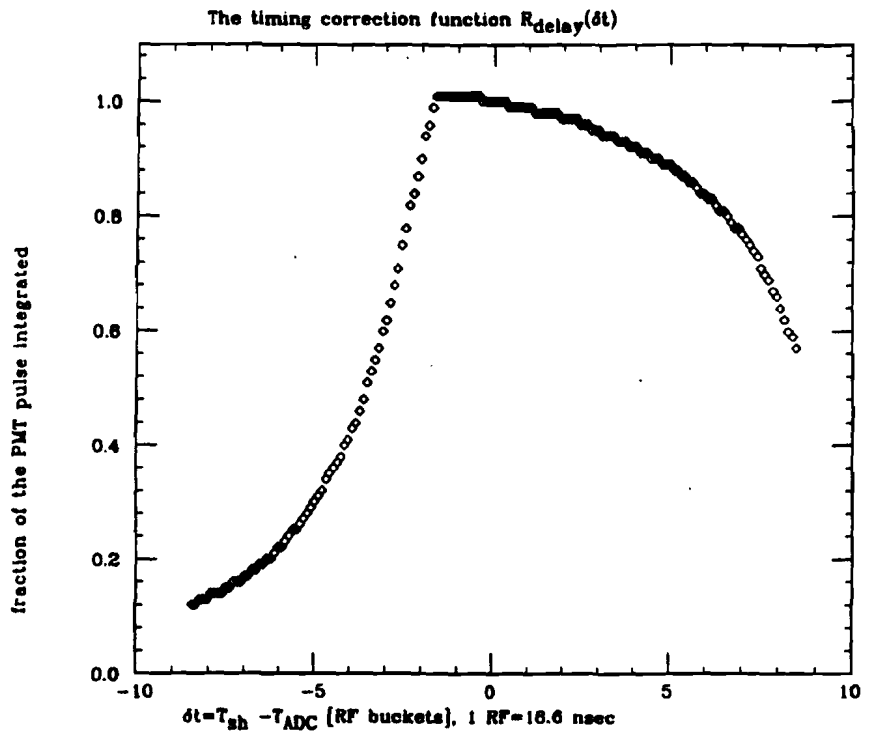

Figure 3.2: The delay correction in the energy calculation R_{delay}, as a function of the difference between the shower timing and the ADC gate. Negative values of ΔT correspond to showers occurring before the trigger. Positive values of ΔT correspond to showers occurring after the trigger.

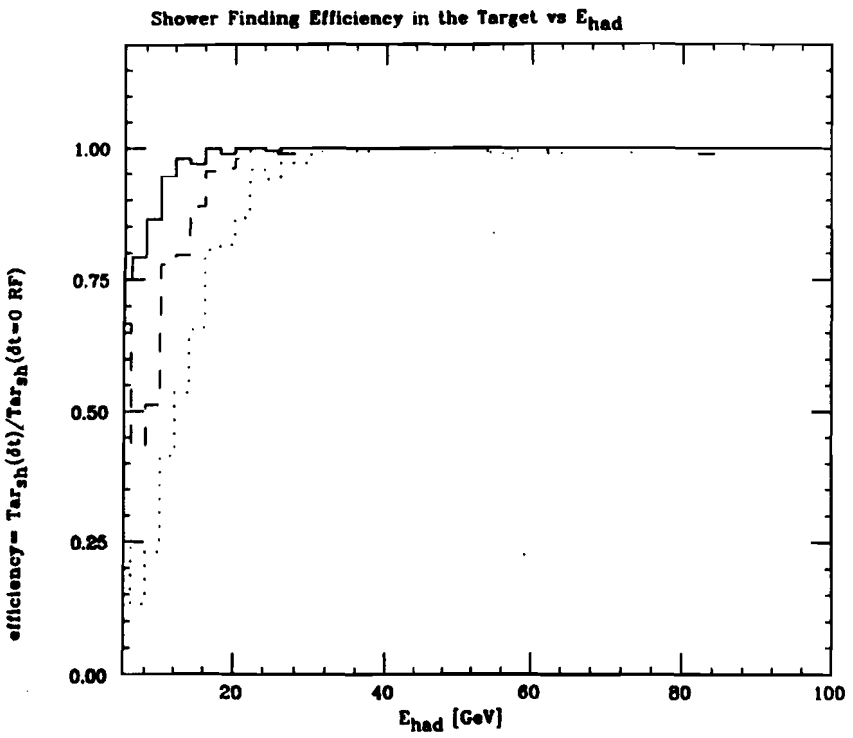

Figure 3.3: The efficiency of shower finding algorithm as as function of shower energy for shower occurring inside the fiducial volume of the Target. The solid line corresponds to the efficiency of finding showers occurring ΔT= 4 RF units after the trigger time. The dashed line corresponds to the efficiency of finding showers occurring ΔT= 8 RF units after the trigger time, and the dotted line corresponds to the efficiency of finding showers occurring ΔT= 9 RF units after the trigger time.

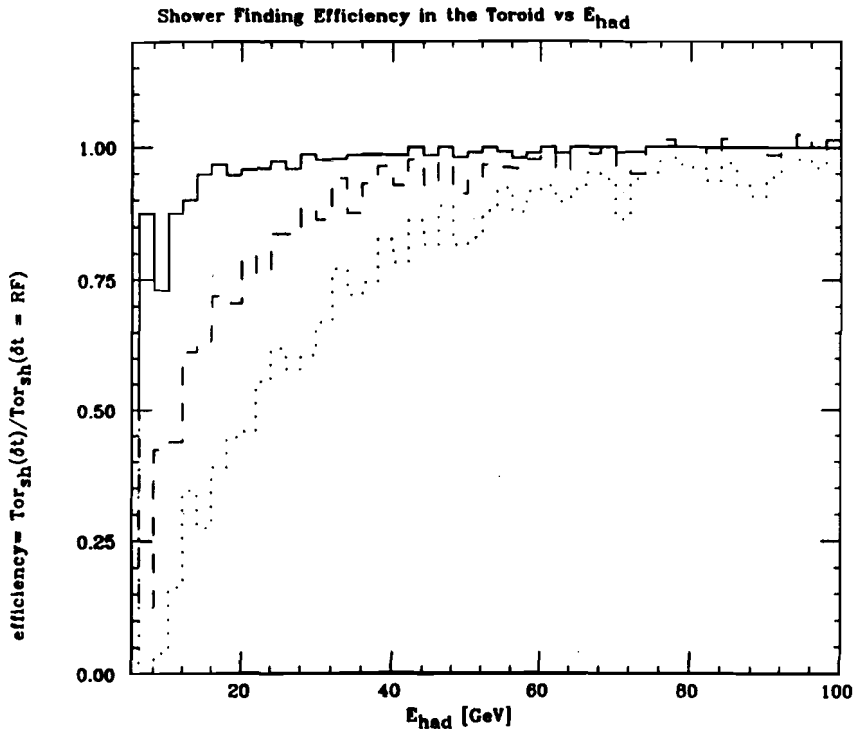

Figure 3.4: The efficiency of shower finding algorithm as as function of shower energy for shower occurring inside the fiducial volume of the Toroid. The solid line corresponds to the efficiency of finding showers occurring ΔT= 4 RF units after the trigger time. The dashed line corresponds to the efficiency of finding showers occurring ΔT= 8 RF units after the trigger time, and the dotted line corresponds to the efficiency of finding showers occurring ΔT= 9 RF units after the trigger time.

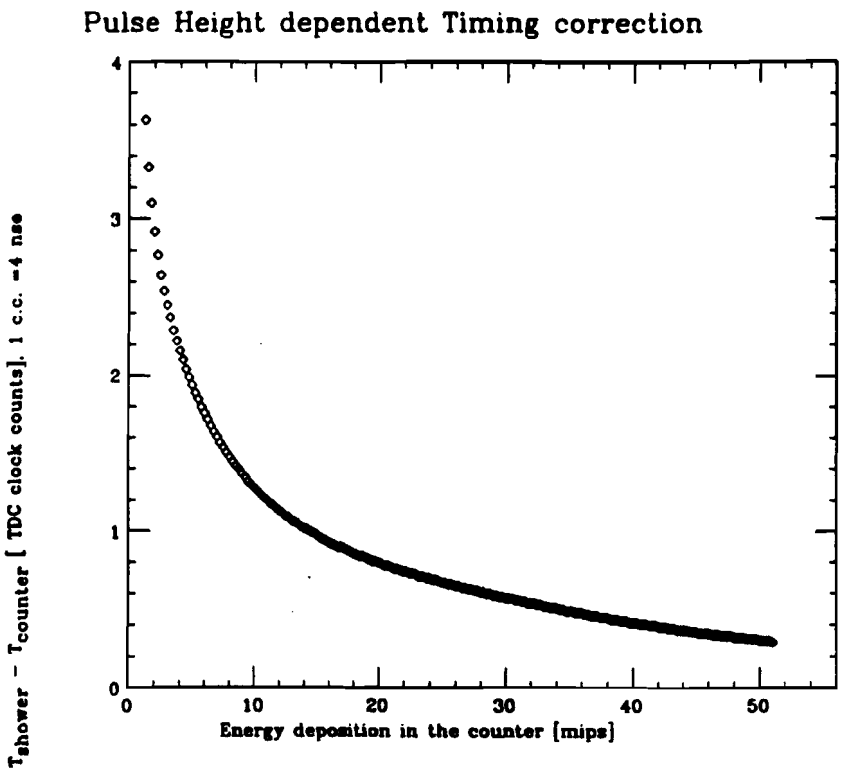

Figure 3.5: The pulse height dependent timing correction as a function of energy deposited in individual counter.

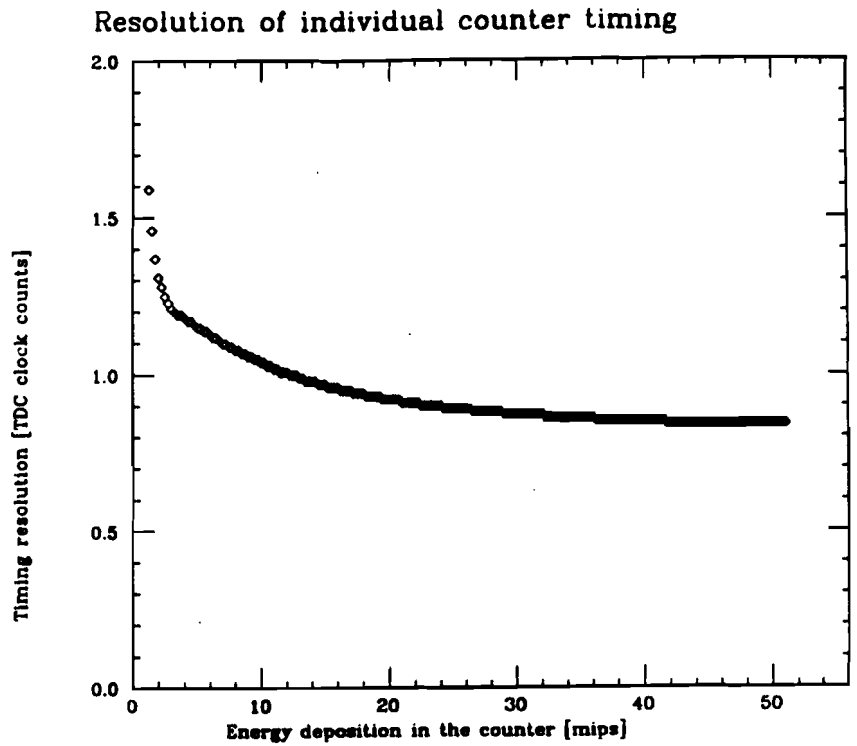

Figure 3.6: The resolution of individual counter timing as a function of energy deposited in the counter.

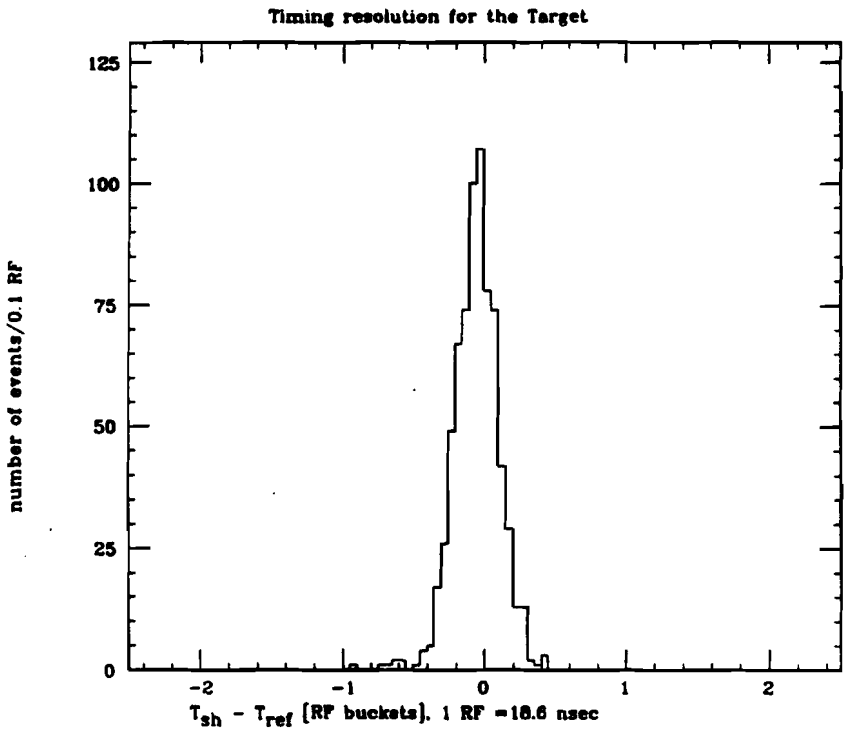

Figure 3.7: Timing resolution of showers occurring inside the fiducial volume of the Target.

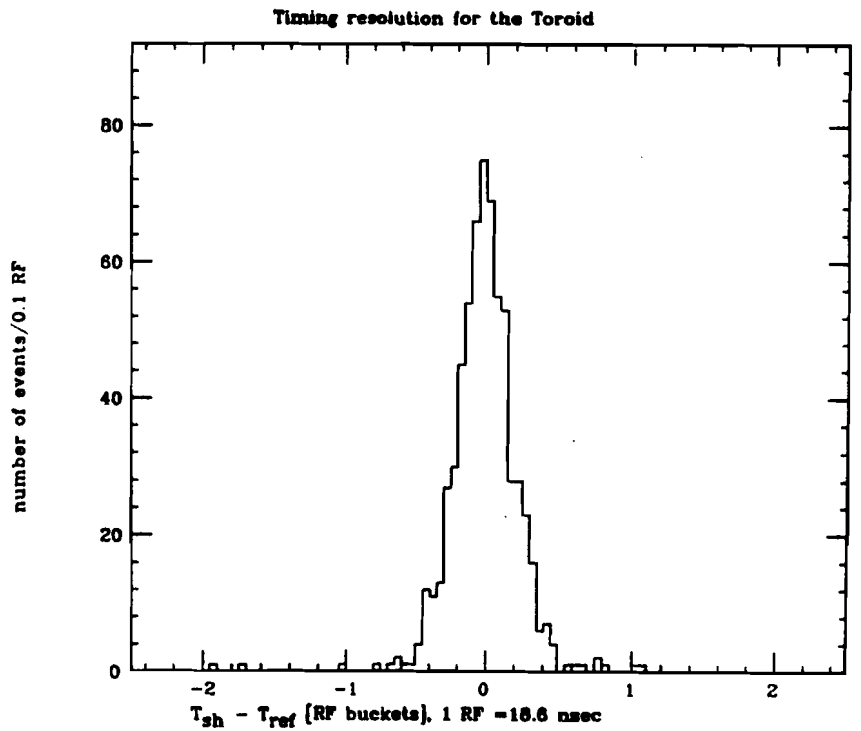

Figure 3.8: Timing resolution of showers occurring inside the fiducial volume of the Toroid.

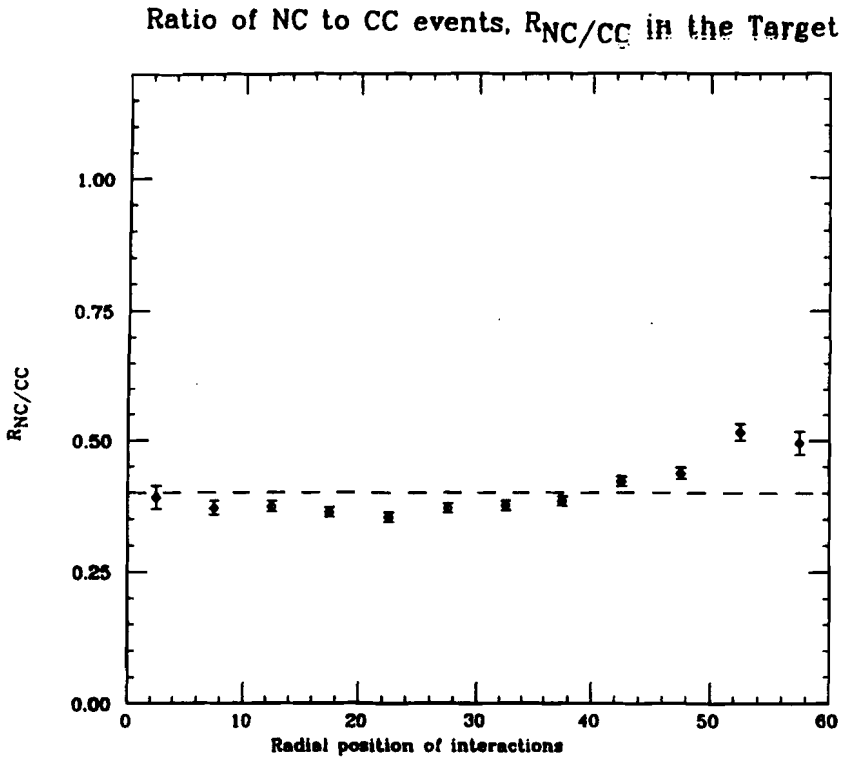

Figure 3.9: The ratio of the NC-type to the CC-type interactions $R_{NC/CC}$, for events occurring in the Target, as a function of the radial position of interaction. The dashed line corresponds to the average value of the ratio $< R_{NC/CC} >^{Target}$ within the fiducial volume of the Target.

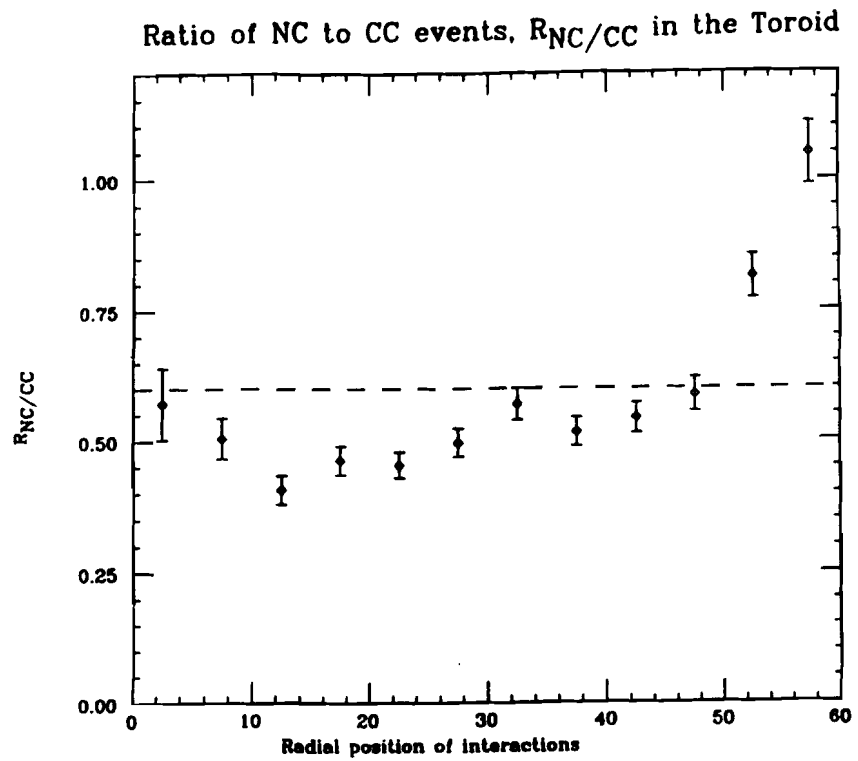

Figure 3.10: The ratio of the NC-type to the CC-type interactions $R_{NC/CC}$, for events occurring in the Toroid, as a function of the radial position of interaction. The dashed line corresponds to the average value of the ratio $< R_{NC/CC} >^{Toroid}$ within the fiducial volume of the Toroid.

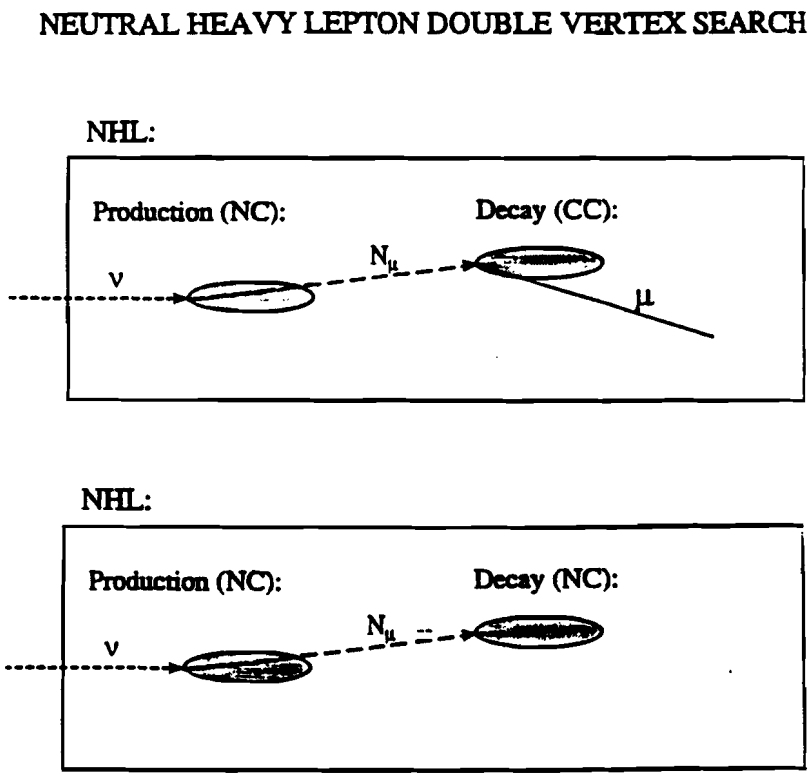

Figure 4.1: Double Vertex signature of Neutral Heavy Lepton production in ν-N interaction. The upper diagram corresponds to the a decaying into muonic channel $NHL \rightarrow \mu + X$. The lower diagram corresponds to a NHL decaying to muonless channel $NHL \rightarrow \nu + X$.

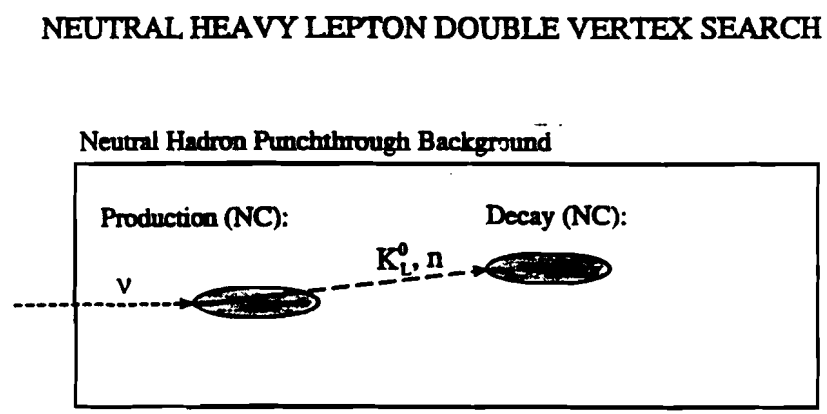

Figure 4.2: Neutral hadron punch-through background of the Double Vertex signature of NHL decaying to muonless channel $NHL \rightarrow \nu + X$.

NEUTRAL HEAVY LEPTON DOUBLE VERTEX SEARCH

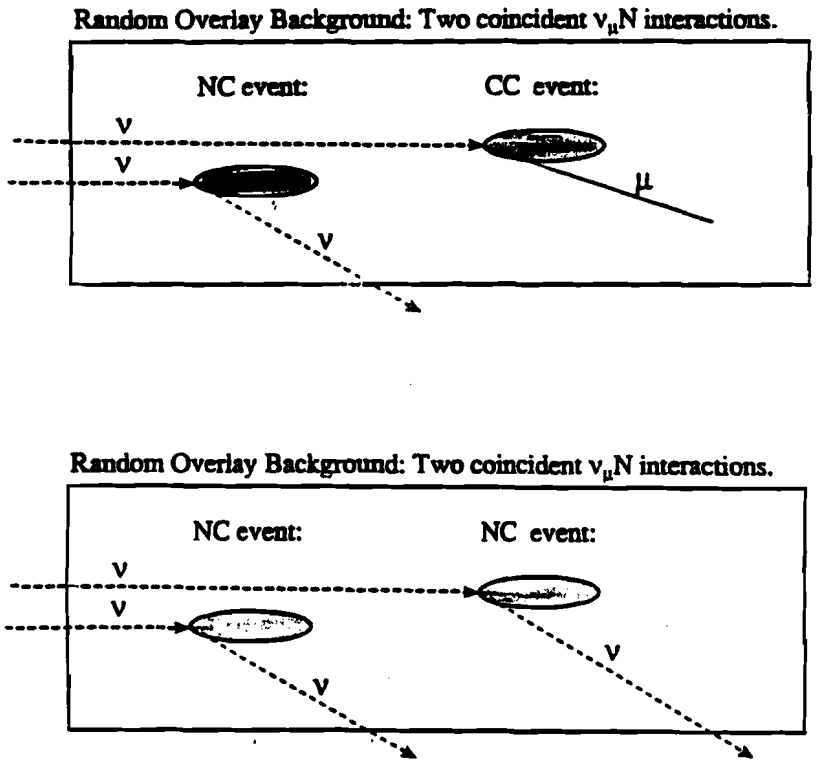

Figure 4.3: Random overlay background of the Double Vertex signature of NHL production.

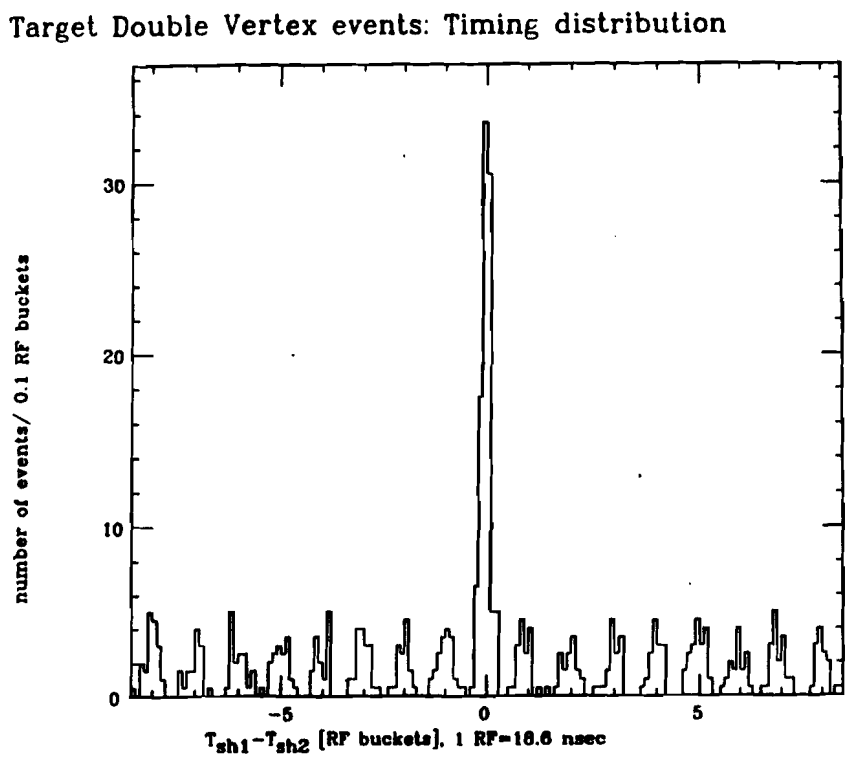

Figure 4.4a: Distribution of the timing difference between the upstream and the downstream showers in the sample of neutrino-induced Double Vertex events. The downstream shower occurred inside the fiducial volume of the Target. Non-zero buckets contain random overlay events. Bucket 0 contains random overlay events, neutral hadron punch-through events and possible NHL candidates. Target Double Vertex events with separation L_{steel} greater than 5 counters are included in this sample.

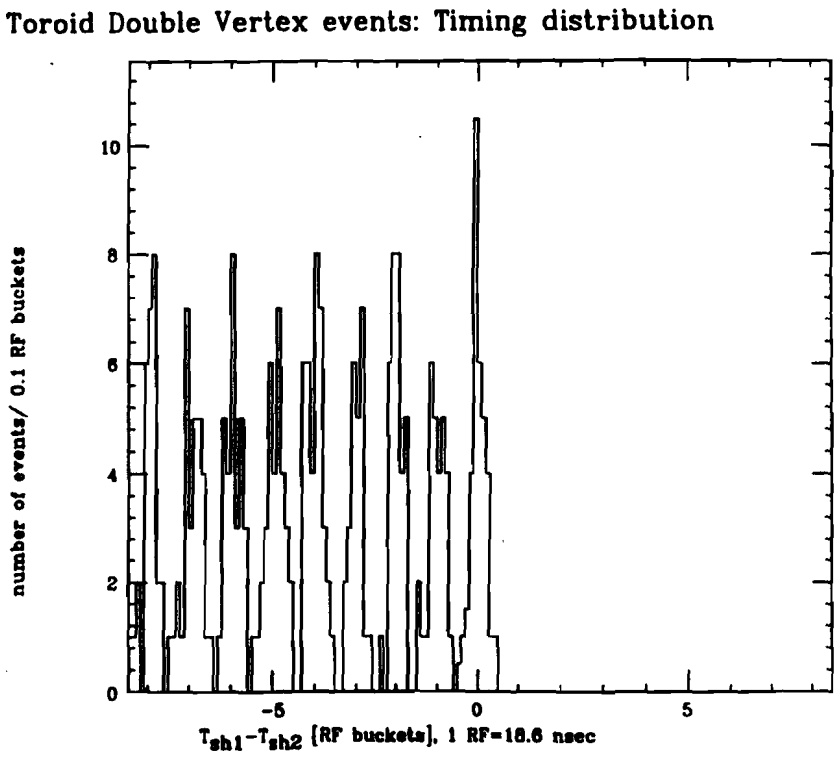

Figure 4.4b: Distribution of the timing difference between the upstream and the downstream showers in the sample of neutrino-induced Double Vertex events. The downstream shower occurred inside the fiducial volume of the Toroid. Only Toroid Double Vertex events with the downstream shower occurring *after* the triggering interaction in the Target took place are included in the sample.

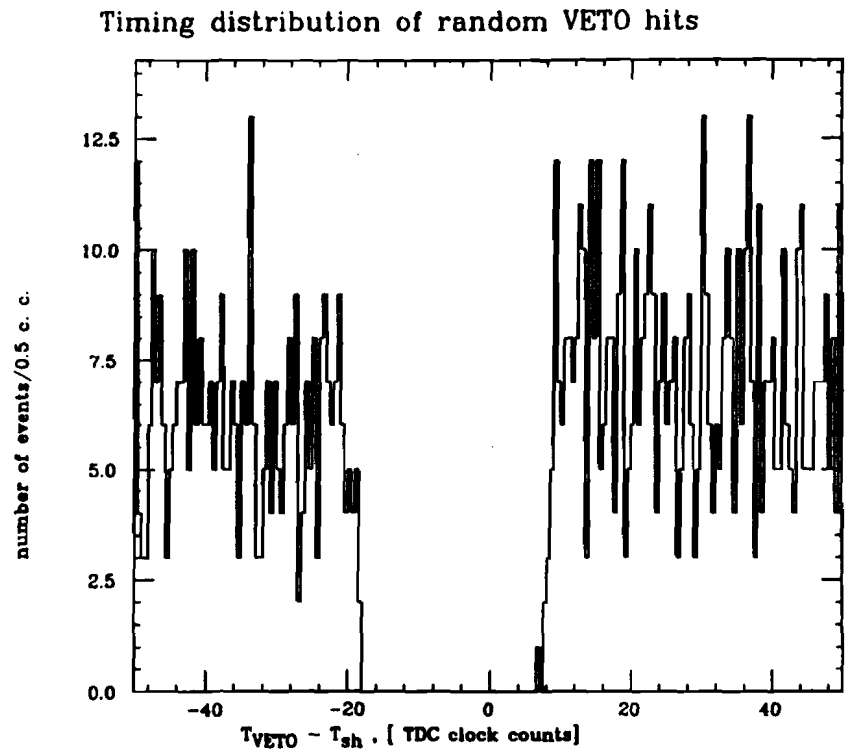

Figure 5.1: Distribution of the difference between interaction time and timing of random VETO hits for sample of Trigger 2 events.

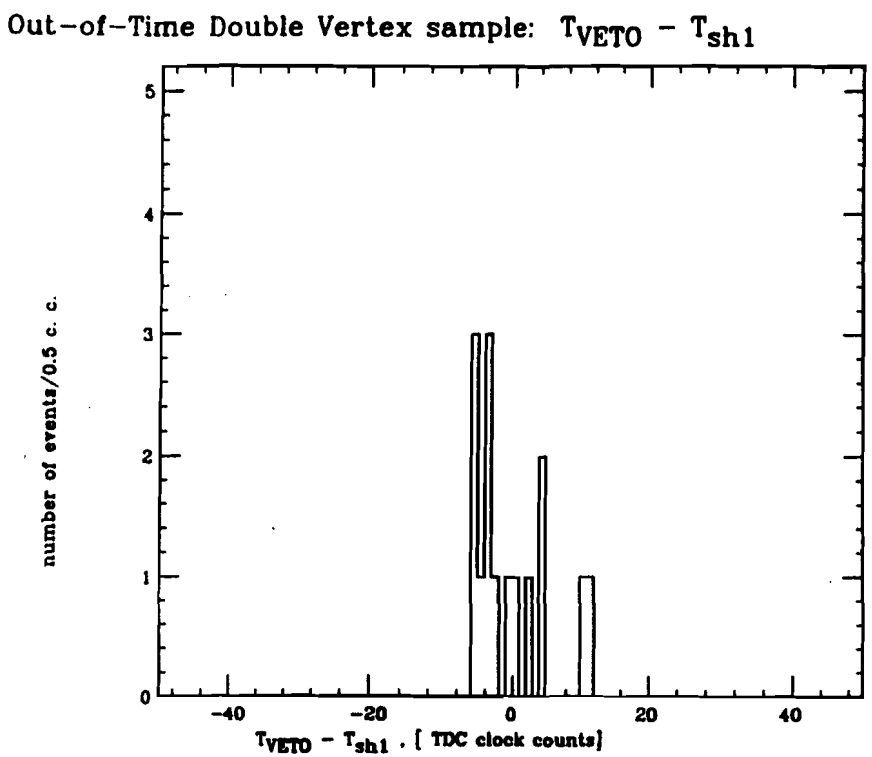

Figure 5.2: Out-of-Time Double Vertex Events with upstream interaction occurring at the edge of fiducial volume of the Target (with $PLACE_1$ =81 or 82): Distribution of the relative timing between upstream shower and the VETO hit.

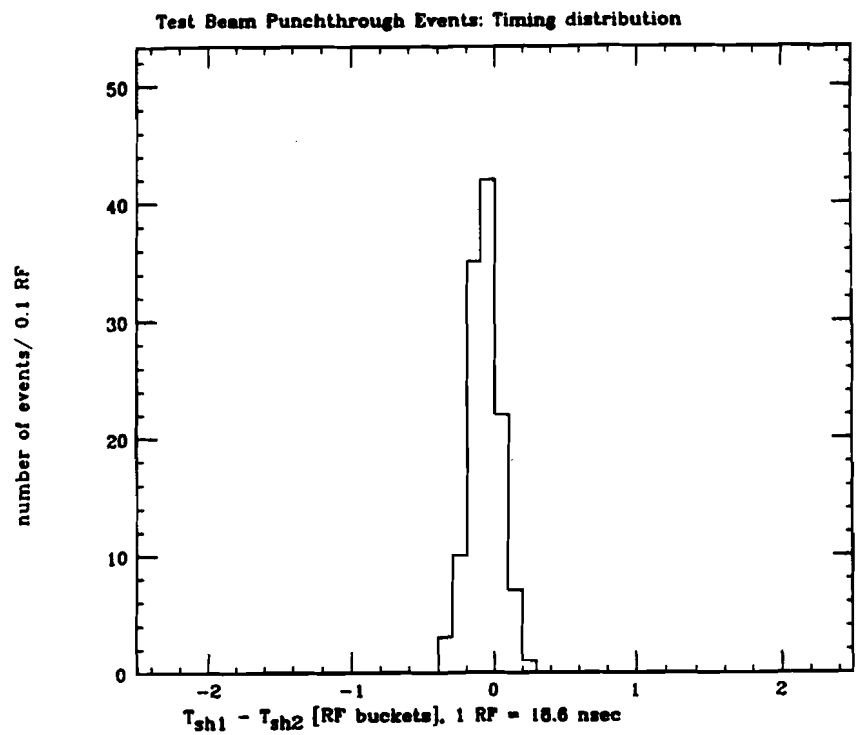

Figure 5.3: Test-Beam punchthrough events: Distribution of the relative timing between the primary and secondary shower. The r.m.s. resolution of the time difference was equal to 2.4 nsec.

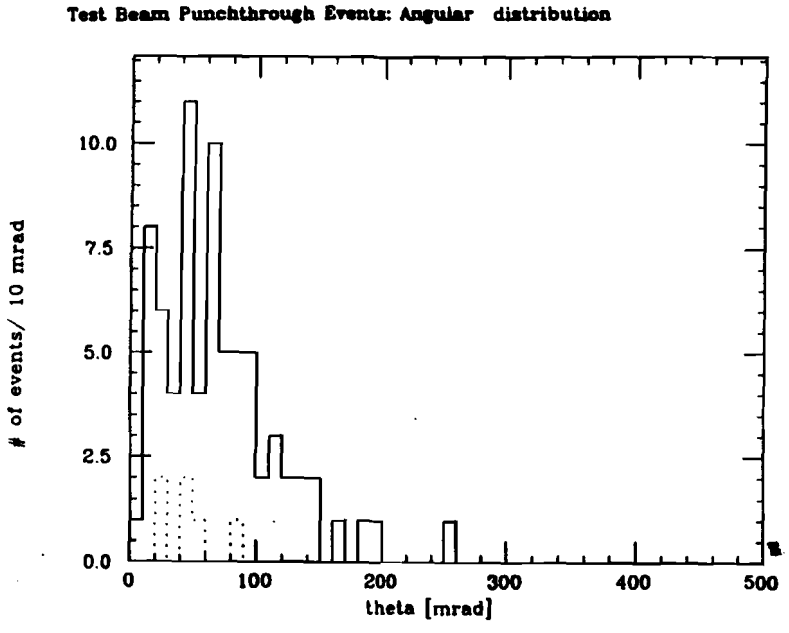

Figure 5.4: Test-Beam punchthrough events: Distribution of the angle between the hadron beam direction and the direction of the neutral hadron punchthrough. Solid line corresponds to Small Separation events and dashed line to Intermediate Separation events.

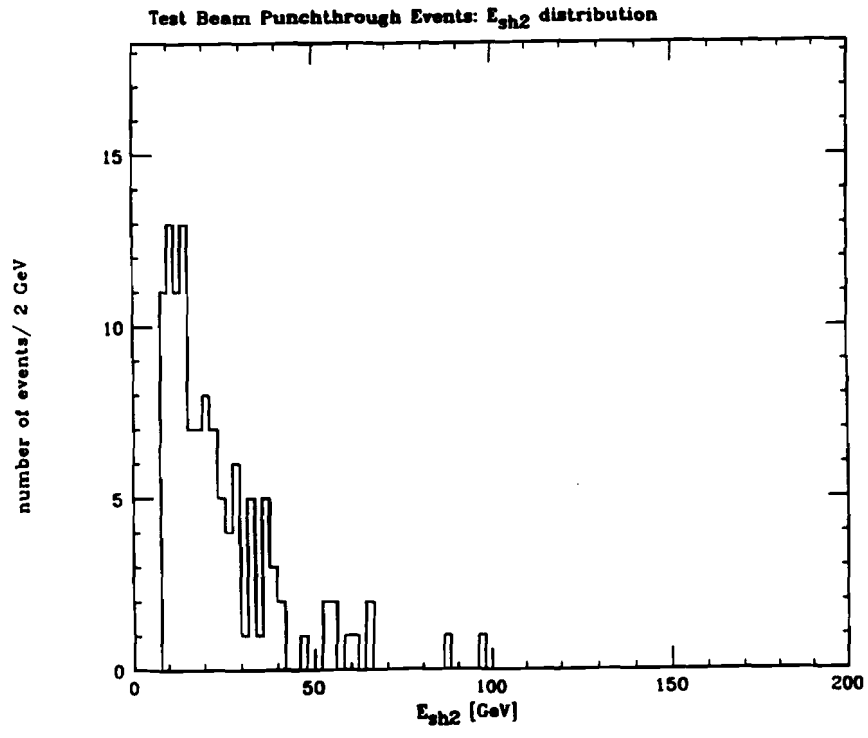

Figure 5.5: Test-Beam punchthrough events: Distribution of the energy of secondary shower.

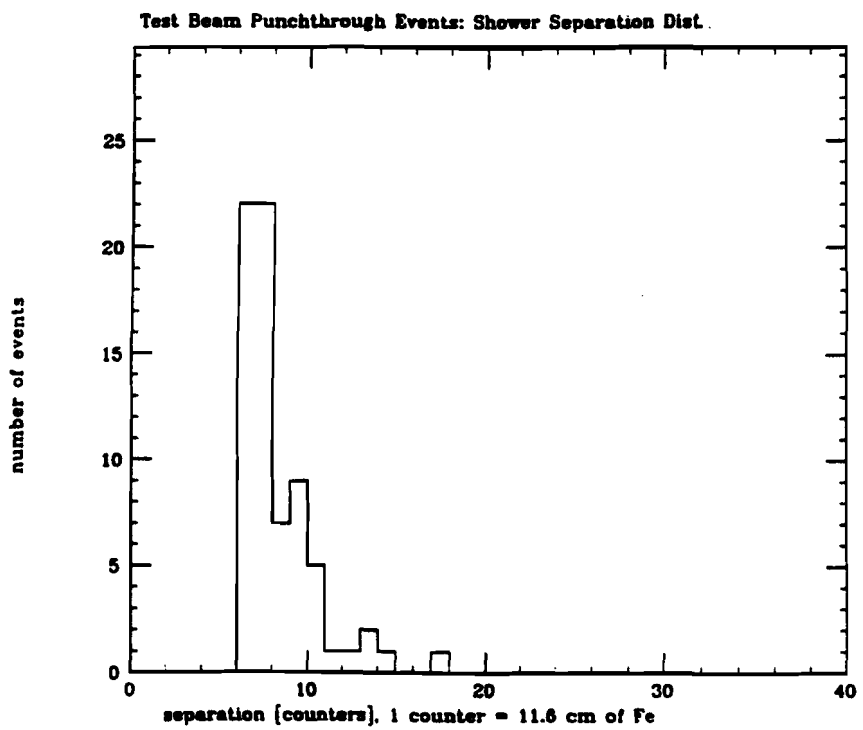

Figure 5.6: Test-Beam punchthrough events: Distribution of the separation between the end of primary shower and the beginning of the punchthrough shower.

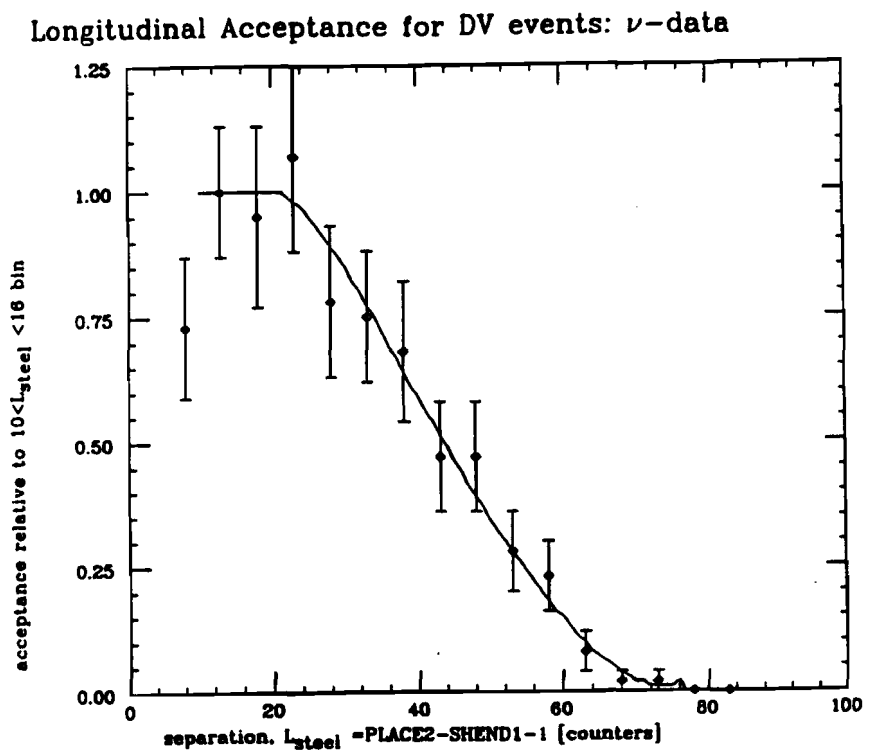

Figure 5.7: Longitudinal acceptance of the CCFR detector for Double Vertex events as a function of the separation between the end of upstream shower and the beginning of the downstream shower. The acceptance function was calculated using sample of Out-of-Time Double Vertex events and normalized for $10 \leq L_{steel} \leq 15$.

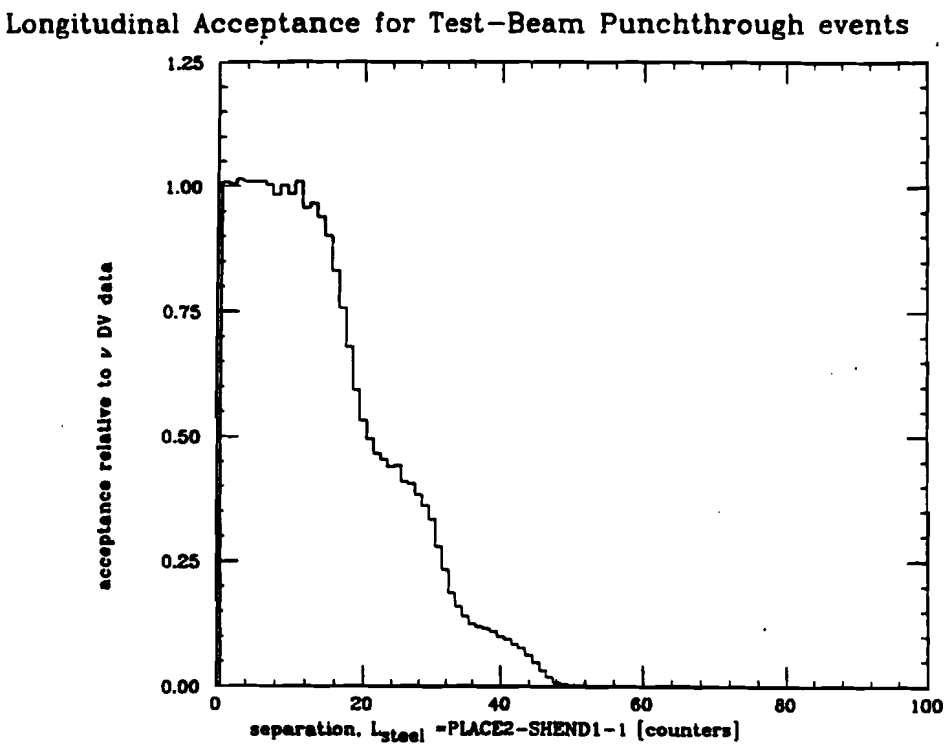

Figure 5.8: Longitudinal acceptance of the Test-Beam detector configuration relative to the acceptance of the neutrino induced Double Vertex events. The step-like function corresponds to the 2-Cart, 3-Cart and 4-Cart configurations of the Test-Beam setup.

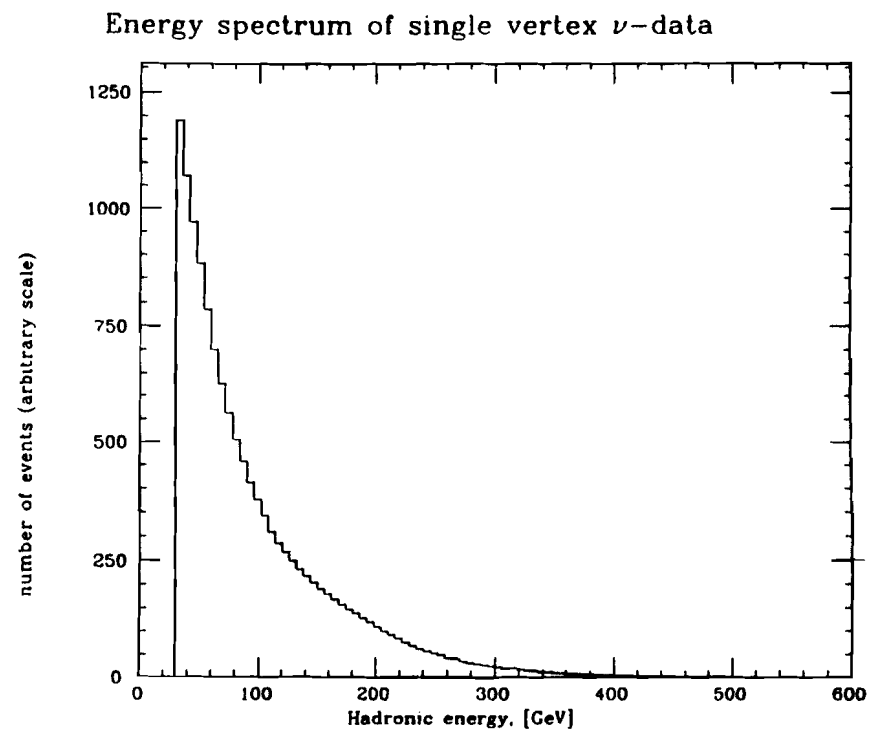

Figure 5.9a: Energy spectrum of single vertex neutrino induced interactions.

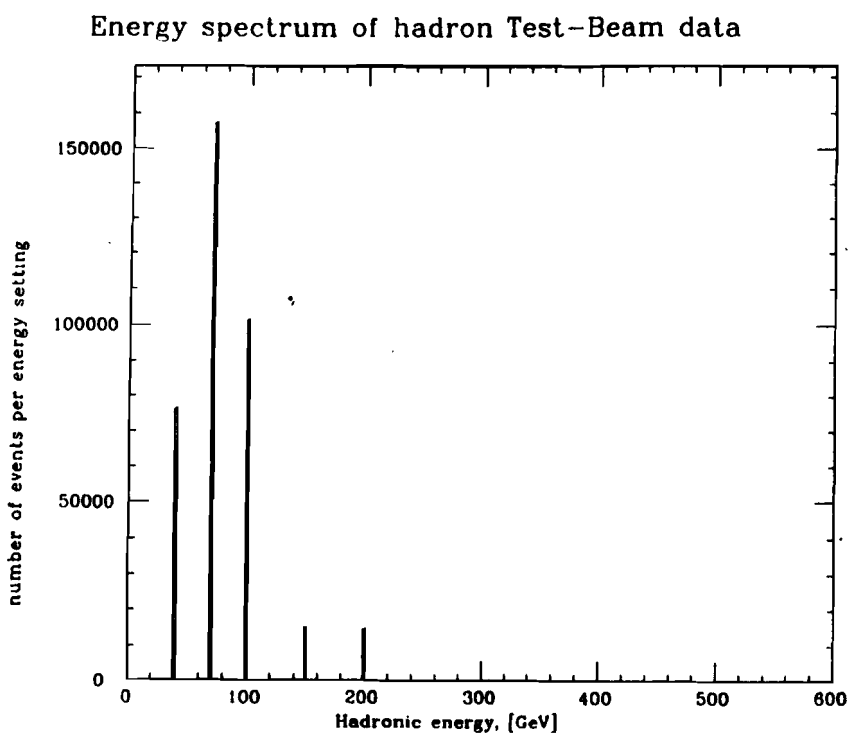

Figure 5.9b: Energy spectrum of hadron Test-Beam data.

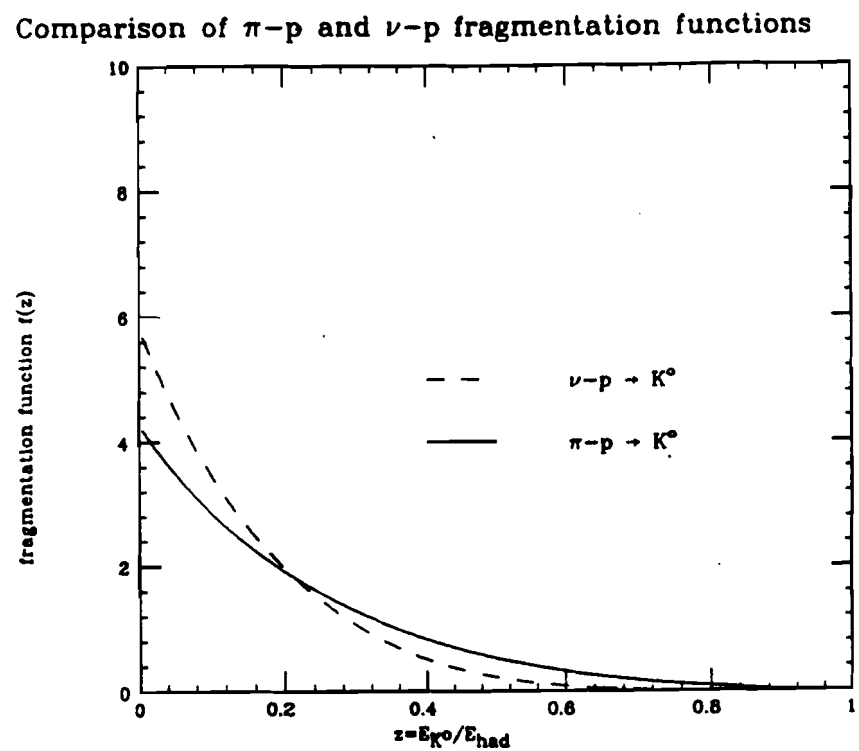

Figure 5.10: Comparison of pion induced and neutrino induced fragmentation functions of K^0 production.

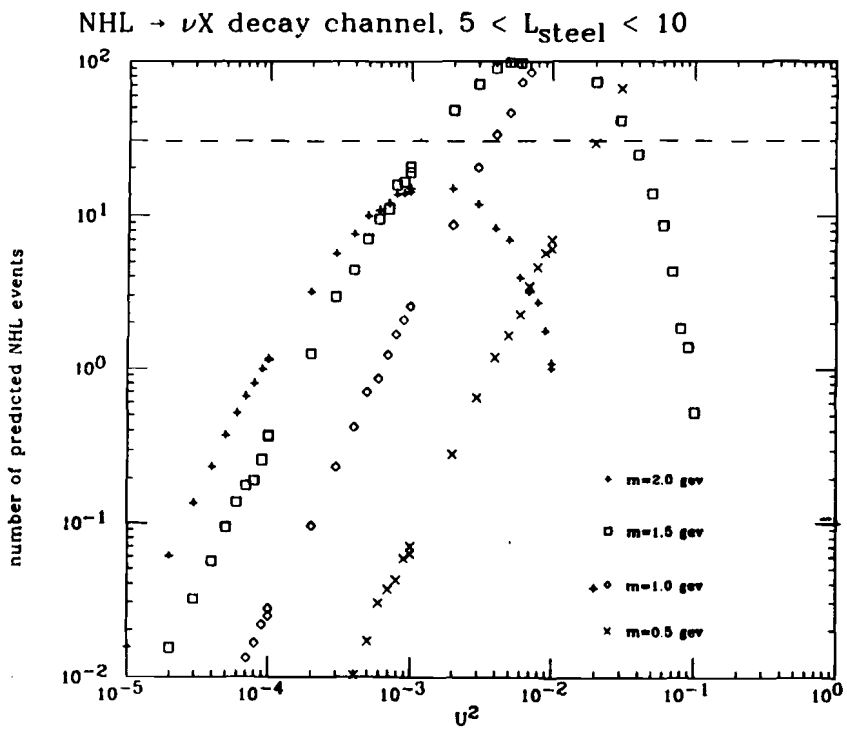

Figure 6.1: $NHL \rightarrow \nu + X$, **Small Separation region: Monte Carlo generated number of NHL as a function of coupling suppression factor U^2, relative to the Fermi coupling G_F for different values of mass of NHL m_{NHL}. The dashed line corresponds to the limit, at 90% CL of number of observed NHLs in this channel.**

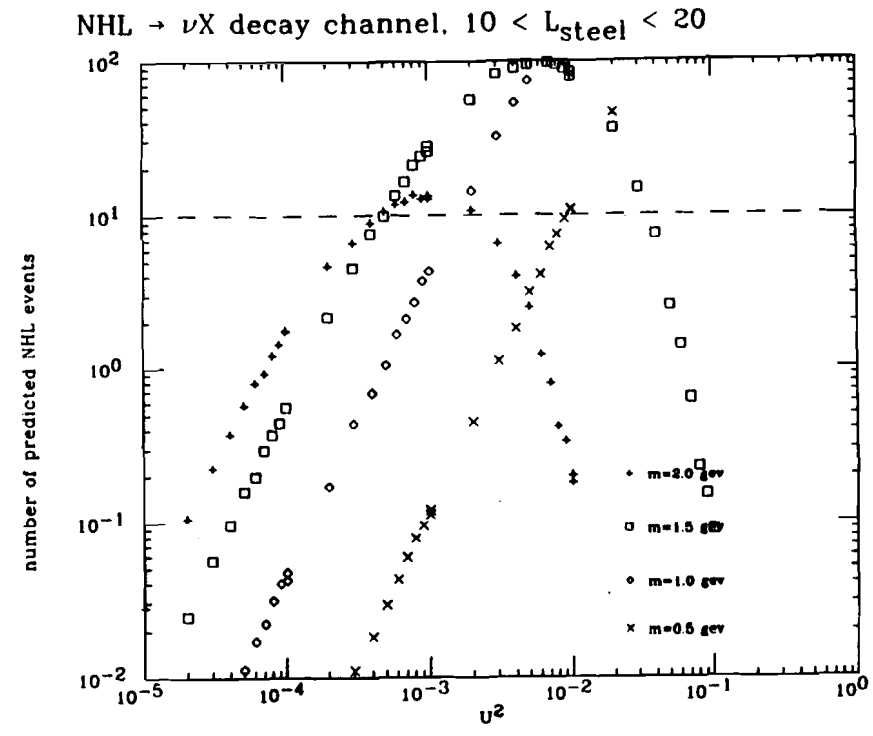

Figure 6.2: $NHL \rightarrow \nu + X$, **Intermediate Separation region: Monte Carlo generated number of NHL as a function of coupling suppression factor U^2, relative to the Fermi coupling G_F for different values of mass of NHL m_{NHL}. The dashed line corresponds to the limit, at 90% CL of number of observed NHLs in this channel.**

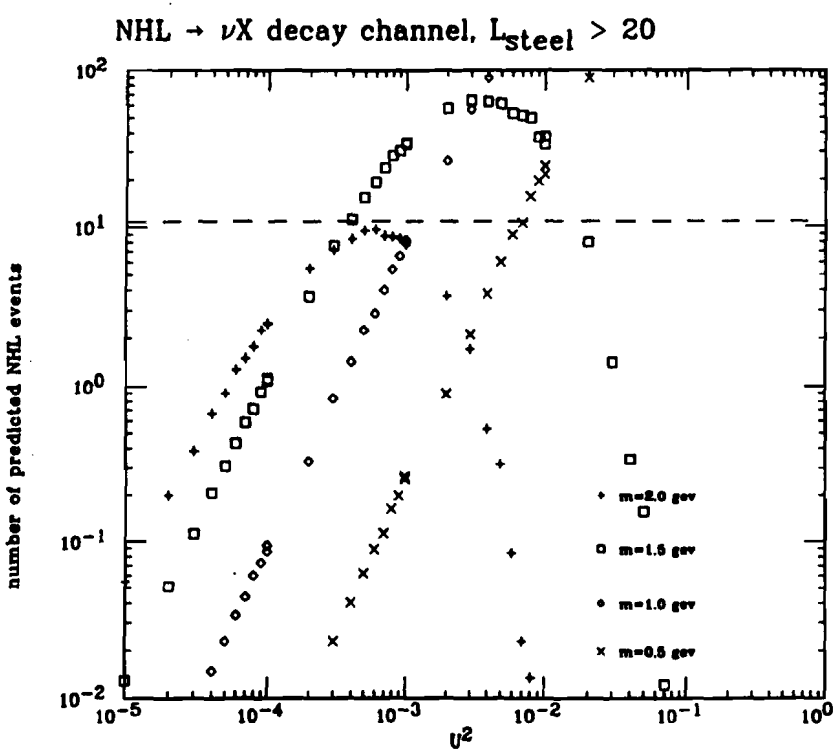

Figure 6.3: $NHL \rightarrow \nu + X$, **Large Separation region: Monte Carlo generated number of NHL as a function of coupling suppression factor U^2, relative to the Fermi coupling G_F for different values of mass of NHL m_{NHL}. The dashed line corresponds to the limit, at 90% CL of number of observed NHLs in this channel.**

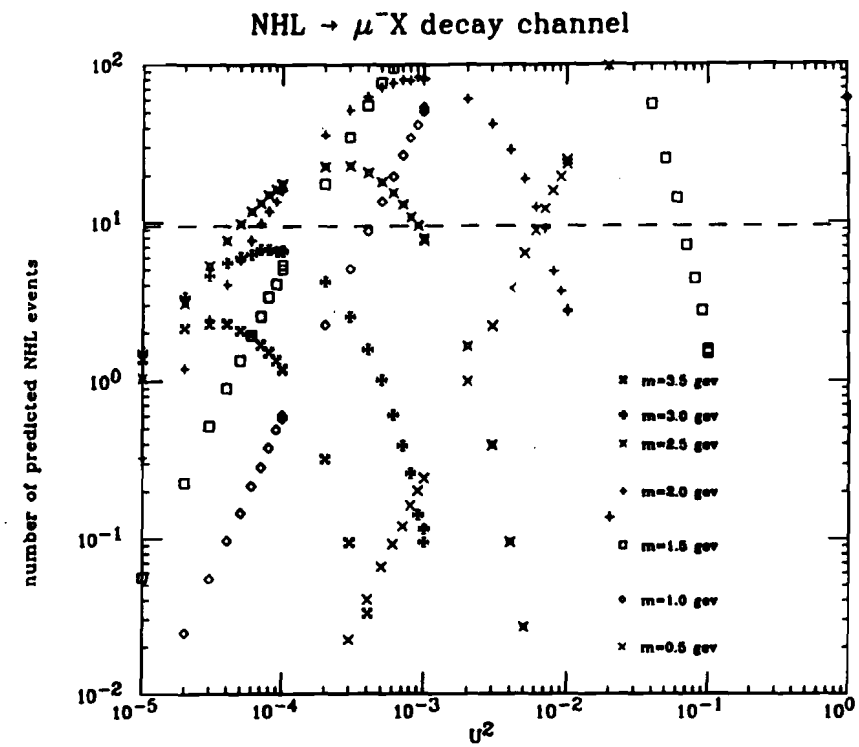

Figure 6.4: $NHL \rightarrow \mu + X$, **Small, Intermediate and Large Separation regions combined: Monte Carlo generated number of NHL as a function of coupling suppression factor U^2, relative to the Fermi coupling G_F for different values of mass of NHL m_{NHL}. The dashed line corresponds to the limit at 90% CL of number of observed NHLs in this channel.**

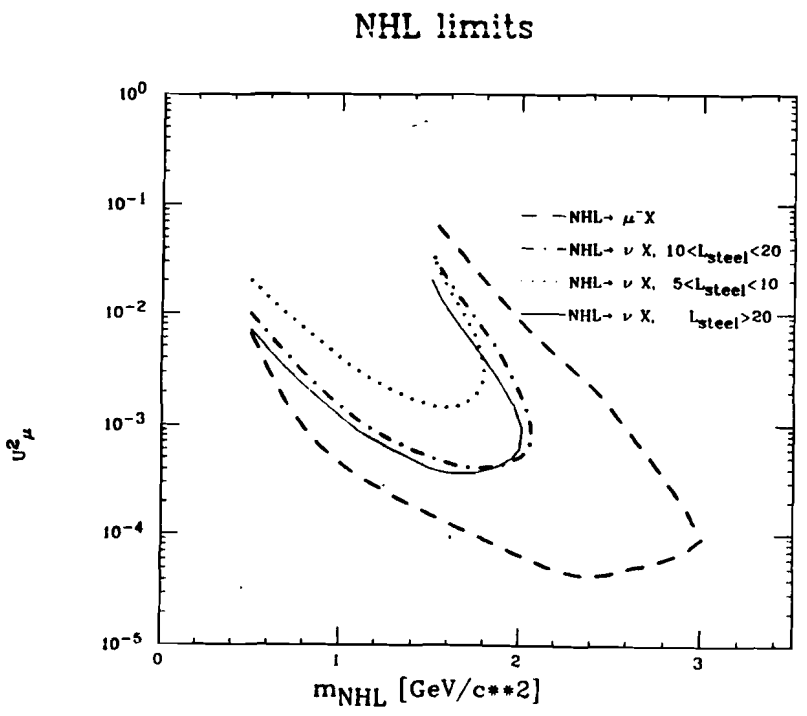

Figure 6.5: NHL limits for charged current and neutral current decay channels and different regions of the separation between the end of the upstream and the beginning of the downstream showers. The limits are presented as a function of NHL mass m_{NHL} and the coupling suppression factor U^2.

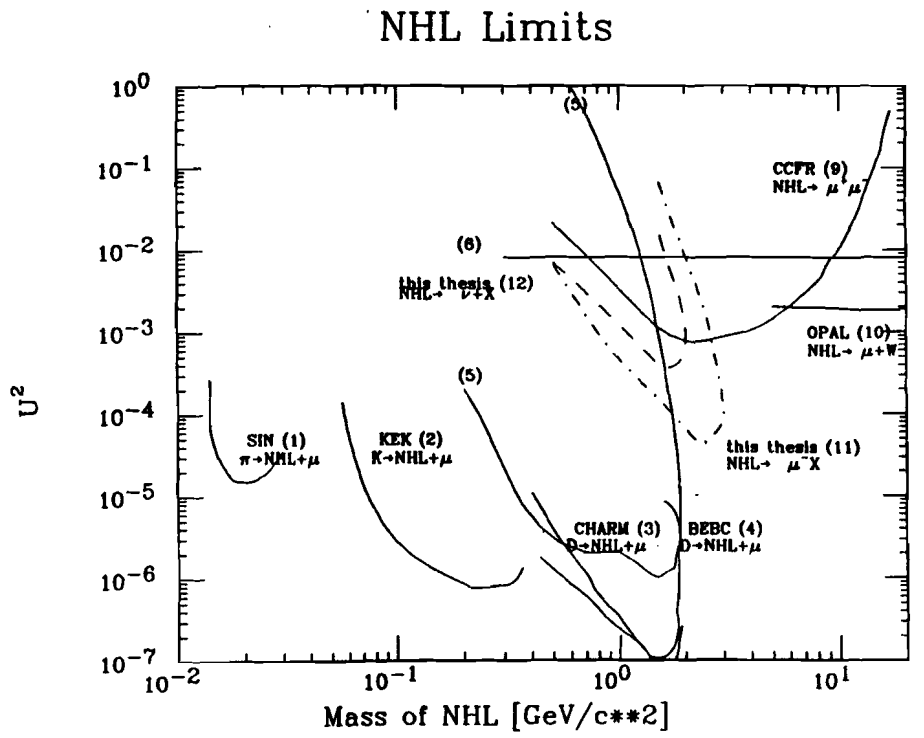

Figure 6.6: Comparison of results for NHL limits for charged current and neutral current decay channels from this thesis with NHL limits from other experiments. Dashed line (11) corresponds to $NHL \rightarrow \mu + X$ channel and dot-dashed line (12) to $NHL \rightarrow \nu + X$ channel The references to other experiments are same as for Figure 1.4

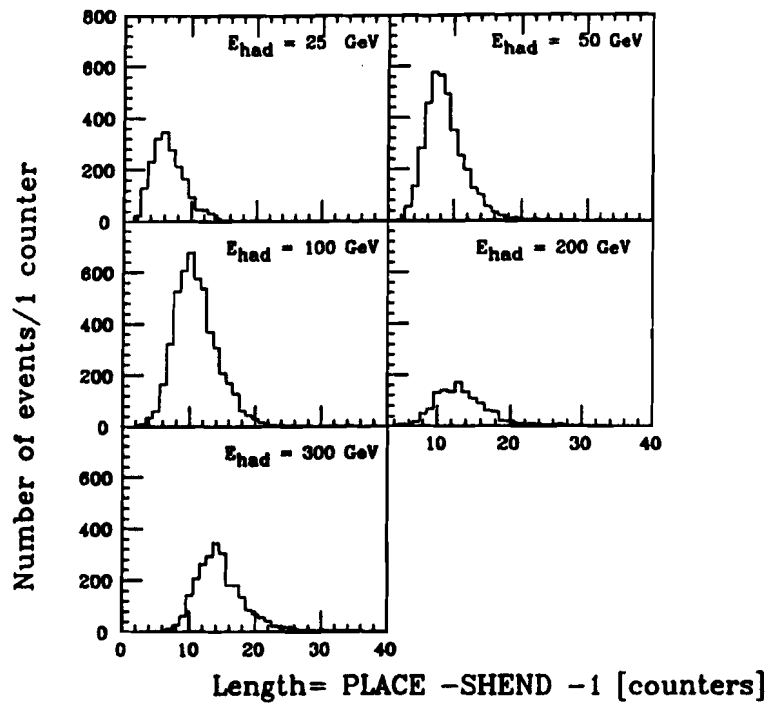

Figure B.1: Distributions of a length of hadronic showers for different settings of hadron energy beam. Hadronic shower length was defined as: $PLACE-SHEND-1$.

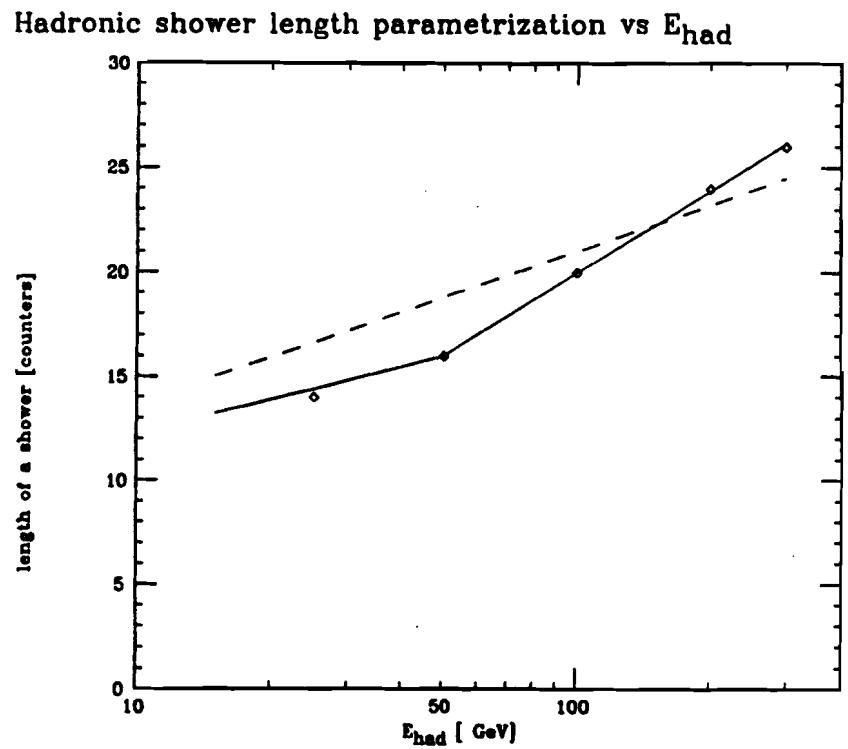

Figure B.2: Parametrization of the length of hadronic showers as a function of hadronic energy E_{had}.: data points and solid line correspond to the 99% length containment para metrization; dashed line corresponds to 99% energy containment parametrization.

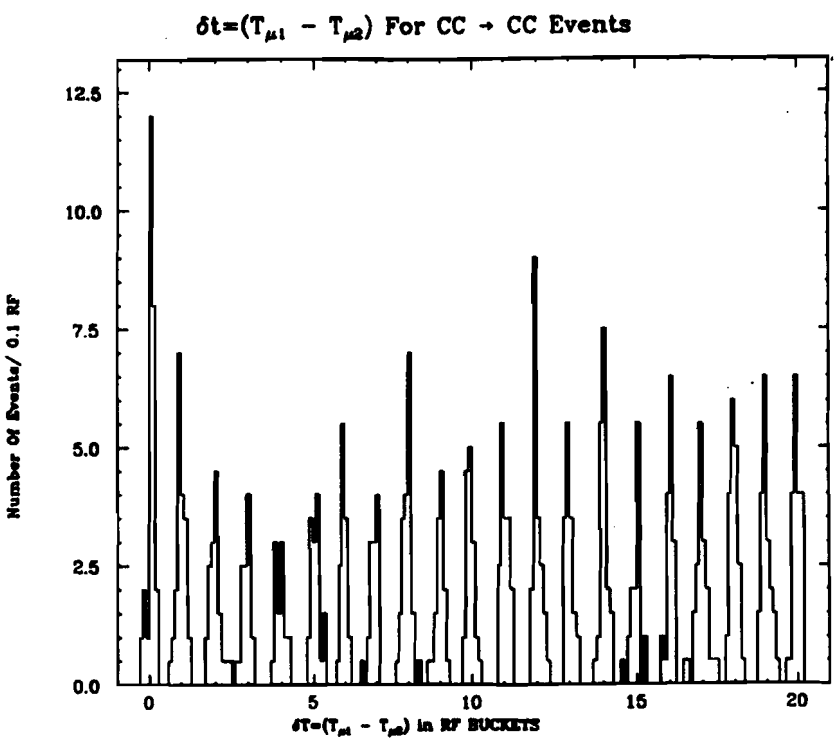

Figure C.1: Distribution of the relative timing between random overlays of two uncorrelated charged current interactions.

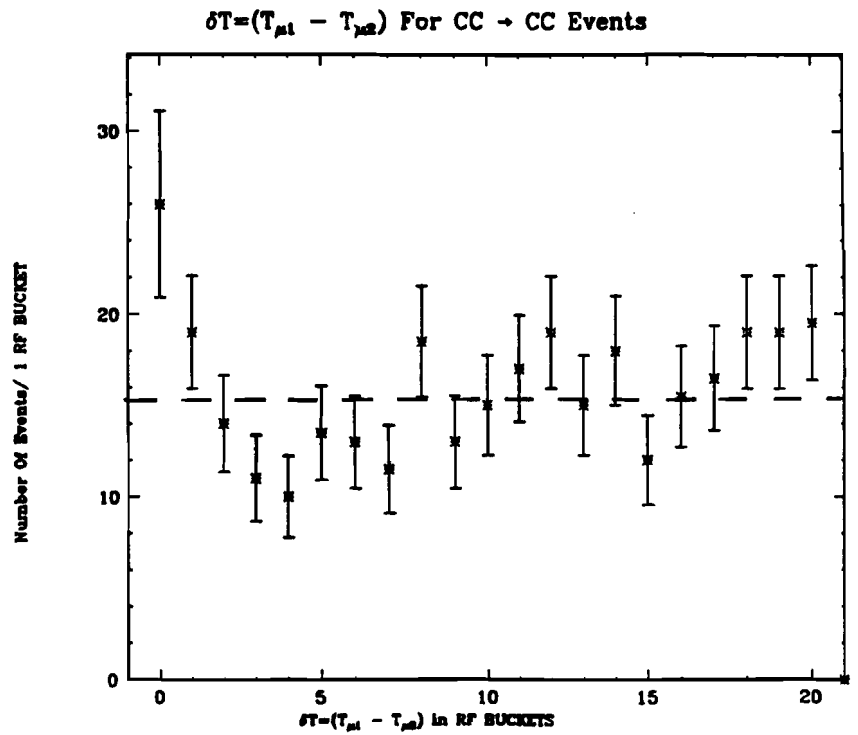

Figure C.2: Number of random $CC \rightarrow CC$ overlays as a function of the timing difference between the two muons. The dashed line corresponds to the average of random Out-of-Time overlays per 1 RF bucket.